Creation of ^{39}K Bose-Einstein condensates with tunable interaction

Nils Winter

PhD Thesis

Institute of Physics and Astronomy
Aarhus University

November 2013

Acknowledgments

I want to use this opportunity to thank some people for their support during writing this thesis. First off all I want to thank Jan Arlt for his support and guidance during my PhD. Then I want to thank Lars Wacker with whom I spent most of the time in the lab for the great work and friendship. I want to thank Nils Byg Jørgensen for being the next Nils at the experiment. I also need to thank Georg Kleine-Büning and Johannes Will for building this awesome experiment. Furthermore I want to thank Jacob Sherson for his advice and scientific discussions.

Then I want to thank my fellow co-workers whom I will not list by name because I would probably forget someone. I want to thank Grete Flarup for helping me through the administrative jungle.

A special thanks goes to Carlsberg for buying us a laser (I waited three years to write this sentence).

Last but not least want to thank all my dear friends in Aarhus whether they were permanently here or just visiting temporarily for making my stay so pleasant. I want to thank Aarhus for being so hilly to keep me well in shape.

Summary

The capability of producing ultracold atomic gases has had considerable impact on the field of quantum physics. Due to their purity and tolerance against external perturbation these ensembles are an ideal instrument for precision experiments in atomic and molecular physics. The ability to create Bose-Einstein condensates and thus accumulate ultracold atoms in a single quantum state enables the construction of model systems which can be precisely controlled. That allows a deeper understanding of complicated quantum systems. Ultracold atoms in optical lattices are an excellent example, since they provide regular lattices that are used as a quantum simulator of solid state systems. In particular the Mott-insulator phase and Cooper paring of fermions could be observed in these ultracold systems. Furthermore the scattering properties of some atomic gases can be tuned to a great extend. This allows the investigation of ultracold chemistry or ideal cases such as non-interacting Bose-gases as well as unitary gases.

Within the framework of this thesis two research direction were explored. First the creation of wave-packets in an optical lattice was demonstrated, which allows for pump probe-spectroscopy using ultracold atoms. Secondly an experimental apparatus for the creation and investigation of ultracold potassium-rubidium mixtures with tunable interactions was constructed and first ^{39}K and ^{41}K Bose-Einstein condensates were created.

This experimental apparatus features a dual-species magneto-optical trap for laser cooling as well as magnetic and optical traps for evaporative cooling until quantum degeneracy is reached. The optical potential is formed by a focused laser beam and allows to trap the atoms while their scattering length is tuned by an external magnetic field. The apparatus is able to create single-species Bose-Einstein condensates consisting of 6×10^5 ^{87}Rb atoms, 2×10^5 ^{39}K atoms and 1×10^4 ^{41}K atoms.

The creation of dual-species condensates will be the next experimental milestone. This will allow for the investigation of the interaction within ultracold potassium-rubidium mixtures leading to the creation of hetero-nuclear molecules or polarons.

Résumé (Summary in Danish)

Den eksperimentelle kapacitet til at kunne producere ultrakolde atomare gasser har haft stor betydning for kvantefysikken. Deres renhed og tolerance overfor eksterne perturbationer har gjort ultrakolde gasser til et ideelt værktøj til præcisionsmålinger inden for atom- og molekylfysik. Muligheden for at producere Bose-Einstein-kondensater, og dermed ophobe ultrakolde atomer i en enkelt kvantetilstand, tillader konstruktionen af nærmest ideelle systemer der kan kontrolleres med høj præcision. Dette muliggør en dybere forståelse af komplicerede kvantemekaniske systemer. Ultrakolde atomer i optiske gitre er et fremragende eksempel, da de regelmæssige gitre, der opstår, kan bruges som en kvantesimulator for systemer fra faststoffysikken. Især kan Mott-isolator-fasen og Cooper-par-dannelse af fermioner observeres i disse ultrakolde systemer. Ydermere kan nogle atomare gassers spredningsegenskaber i høj grad styres. Dette tillader undersøgelser af ultrakold kemi eller af ideelle systemer, så som ikke-interagerende Bose-gasser og unitære gasser.

Inden for rammerne af denne afhandling er to mulige forskningsretninger blevet undersøgt. Først er dannelsen af bølgepakker i optiske gitre blevet vist, hvilket tillader pumpe-probe-spektroskopi igennem brugen af ultrakolde atomer i et optisk gitter. Derefter er en eksperimentel opstilling blevet konstrueret, der har til formål at undersøge ultrakolde kalium-rubidium blandinger, hvor interaktionen kan styres, og at producere ^{39}K og ^{41}K Bose-Einstein-kondensater.

Den eksperimentelle opstilling har en magneto-optisk fælde der kan bruges til laserkøling af både kalium og rubidium, samt magnetiske og optiske fælder, der igennem fordampningskøling muliggør kvantemekanisk udartning. Det optiske potentiale skabes af en fokuseret laser og giver mulighed for at fange atomer, mens deres spredningslængde kan ændres igennem et eksternt magnetisk felt. Opstillingen kan producere Bose-Einstein-kondensater med enten 6×10^5 ^{87}Rb atomer, 2×10^5 ^{39}K atomer eller 1×10^4 ^{41}K atomer.

Den næste eksperimentelle milepæl er produktionen af Bose-Einstein-kondensater, indeholdende to forskellige grundstoffer på samme tid. Dette giver mulighed for at undersøge interaktionen i blandinger af ultrakolde kalium-rubidium blandinger, hvilket kan bruges til dannelsen af heteronukleare molekyler eller polaroner.

Contents

1 Introduction

> *It's a popular fact that ninety percent of the brain is not used and, like most popular facts, it is wrong. [...] It is used. One of its functions is to make the miraculous seem ordinary, to turn the unusual into the usual. Otherwise, human beings, faced with the daily wondrousness of everything, would go around wearing a stupid grin, saying "Wow," a lot. Part of the brain exists to stop this from happening.*
>
> — Terry Pratchett, *Small Gods*

Quantum mechanics has become one of the most powerful concepts in physics. Although it was very controversial in the beginning of the 20th century it is widely accepted nowadays. It makes fruitful contributions to most branches of physics, such that even fields like astronomy that are not intuitively related to small objects profit from it. The precise knowledge of atomic spectra helps to measure the speed at which the galaxies move apart and huge, massive objects like neutron stars are heavily dominated by quantum mechanical effects. In solid state physics is possible to observe macroscopic manifestations of quantum effects like superconductivity. High energy physics is maybe the most extreme application, relying on a fully quantized description of the composition of matter.

It is therefore crucial to verify theoretical models describing existing quantum mechanical systems or to test the foundations of quantum theory by constructing and investigating new systems. It is often difficult to construct a particular model system since the experimental parameters are hard to control (e.g., impurities in

crystal structures). It is therefore desirable to have a universal quantum simulator or quantum computer. Ultra-cold atomic gases are a promising candidate for such a yet-to-construct apparatus. Atomic gases can be trapped by optical and magnetic fields in a ultra-high vacuum systems and can thus be well decoupled from the environment.

To study quantum effects a regime where the non-classical properties of matter dominate has to be reached. This is the case when the inter-particles spacing is on the order of the thermal de-Broglie wavelength. The temperature that is required to observe quantum phenomena depends on the density and can therefore even reach a few million Kelvin in a neutron star. In contrast to that, the atomic gases that are used in the apparatus I describe in the following chapters have a low density, ranging from $1{\times}10^{10}$ to $1 \times 10^{14}\,\mathrm{atoms/cm^3}$. To observe quantum phenomena in such systems a very low temperature of a few hundred nanokelvin is required.

If the temperature of such bosonic clouds is decreased further and further a quantum mechanical description is therefore required to describe the system appropriately. The consequence of such an analysis is, that above a certain phase space density all exited states are occupied and the atoms start to accumulate in the ground state of the system. This phase transition was first predicted by Einstein [1] in 1925, following the work of Bose [2]. The new quantum phase is therefore called Bose-Einstein condensate (BEC). It took another 70 years until the first BECs in weakly interacting gases were observed in the group of Wieman and Cornell [3] shortly followed by the group of Ketterle [4], for which they were awarded with the Nobel Price in 2001.

The new phase has peculiar properties. Although is it a very dilute gas, a BEC is shows superfluid behaviour which can easily be observed through the formation of vortices [5] which represent the quantization of the angular momentum in the ensemble. This demonstrates one of the astonishing properties if a BEC. Beside the superfluidity, the main characteristic of a BEC is that it is phase coherent which was demonstrated soon after it was had been created [6]. This coherence makes a BEC an interesting candidate for interferometric applications [7] and storage [8].

The BECs obtained from ultra-cold gases are in many aspects ideal quantum systems. Since they are well-isolated there is almost no interaction with the environment and the lifetime of a BEC is mainly limited by interactions within the condensate. Due to the way a BEC is created it can be guaranteed that there are no impurities by other elements and it can be prepared in a single spin state.

Over the past decade a number of powerful manipulation techniques for the investigation of these quantum gases were developed. Optical lattices can be used

to form an ideal (without defects) periodic potential for the atoms. If a BEC is loaded into such an lattice it can be used as an quantum simulator for solid state systems [9]. Ultra-cold atoms can also be used to study ultra cold chemistry by associating molecules [10]. Thus ultra cold gases and BECs provide versatile quantum objects with a multitude of scientific applications.

In the experimental apparatus that I describe in the following chapters Bose-Einstein condensates of ^{87}Rb, ^{39}K and ^{41}K were created. This is achieved by first accumulating cold atoms in a combined optical and magnetic potential (a so-called magneto-optical trap). The atoms are then loaded into a purely magnetic trap that provides tight confinement and are further cooled by evaporating the hottest atoms of the ensemble. Subsequently the atoms are loaded into a purely optical trap such that the magnetic field is available as a free parameter to manipulate the quantum system. In this trap they are further cooled until condensation by continuing with the evaporative cooling. Until now only single-species condensates have been obtained but in the future dual species potassium-rubidium condensates will be created to study the behavior of such hetero-nuclear mixtures.

The combination of potassium and rubidium is very favorable for several reasons. Rubidium has a sufficiently high background scattering length such that is rethermalises quickly which eases the cooling and thus the creation of BECs. Potassium on the other hand has three stable isotopes where ^{39}K and ^{41}K are bosonic and ^{40}K fermionic. This may allow for experiments with a fermionic species in the future.

In particular ^{39}K was chosen because of the possibility to tune the scattering properties over a wide range from attractive over non-interacting to repulsive. This makes potassium a very versatile system. Additionally the inter-species scattering can be tuned such that the properties of the hetero-nuclear mixtures can be controlled. Hence potassium an rubidium provide an ideal combination for a vast spectrum of investigations.

The thesis is structured as follows:

- In chapter 2 the theoretical foundation of Bose-Einstein condensates and different experimental techniques is presented.

- The results of the first year of my PhD are presented in chapter 3 where a method for creating wave packets in an optical lattice is explained.

- Chapter 4 is a description of the experimental apparatus used to create potassium and rubidium BECs.

- The sympathetic cooling of ^{39}K and ^{41}K in magnetic traps and the production of a ^{87}Rb BEC is presented in chapter 5.
- In chapter 6 I report on the steps that had to be taken to create a ^{39}K BEC.
- With the final chapter 7 I conclude the thesis and give an outlook to the work that is planned in the future and possible other avenues that can be taken.

2 Theoretical background and experimental techniques

This chapter focuses on the theoretical background of Bose-Einstein condensates and the experimental techniques needed for the work performed for this PhD thesis. First, the most important properties of (non)-interacting Bosonic atomic gases are described in section 2.1. The two available trapping techniques for neutral atoms, magnetic traps and optical traps are introduced in section 2.2 and section 2.3. Then the methods for preparing the internal state of an atom are presented in section 2.5. In section 2.4 laser cooling is explained which is a crucial prerequisite in order to obtain large enough samples of cold atoms that can be loaded into the previously discussed traps. Concluding this chapter, I will discuss basics of scattering theory and Feshbach resonances in section 2.6.

Within this thesis the atoms are prepared and investigated within the $5^2S_{1/2}$ ground state and the excited $5^2P_{3/2}$ state and their hyperfine manifolds (see Figure A.1 for a level diagram). The excited levels are labeled as F' while the ground state is labeled as F. To simplify the description, bra-ket notation is used and if not further specified $|a, b\rangle \equiv |F, m_F\rangle$, where m_F denotes the magnetic sub-state.

2.1. Bosonic atomic gases near zero temperature

Provided the inter-particle spacing of a Bosonic gas consisting of particles of mass m is much larger than the thermal de Broglie wavelength $\lambda_T = \sqrt{2\pi\hbar^2/mk_\mathrm{B}T}$, the Bosonic nature of the particles is insignificant. This happens at high temperatures in which case the gas can be described by the well-known Maxwell-Boltzmann

statistics

$$N_i(\epsilon_i) = \mathrm{e}^{-\frac{\epsilon_i}{k_\mathrm{B}T}}, \tag{2.1}$$

where T is the temperature, ϵ_i is the energy of the i-th state and k_B the Boltzmann constant.

2.1.1. Ideal Bose gases

Near zero temperature the indistinguishable nature of Bosons starts playing a role. For non-interacting Bosons in thermal equilibrium, the mean occupation is given by the Bose-distribution function [11]

$$N(\epsilon_i) = \frac{1}{\mathrm{e}^{(\epsilon_i-\mu)/k_\mathrm{B}T} - 1}, \tag{2.2}$$

where μ is the chemical potential. The chemical potential has to be smaller then ϵ_0 since $N(\epsilon_i)$ would become negative for the lowest energy state otherwise. At high temperatures the Bose-distribution goes over into the Boltzmann distribution.

For $\mu \to \epsilon_0$ the occupation of the ground states increases which describes the process of Bose-Einstein condensation. The density of a Bose gas can be calculated classically, with the momentum $\mathbf{p}$ and position $\mathbf{r}$ the number of states in the volume element $\mathrm{d}\mathbf{p}\mathrm{d}\mathbf{r}$ is $\mathrm{d}\mathbf{p}\mathrm{d}\mathbf{r}/(2\pi\hbar)$. The number of excited states can be calculated semi-classically by integrating the Bose distribution function over the positions and momentum states [11]

$$N_\mathrm{ex} = \int\int \frac{1}{(2\pi\hbar)^3 \cdot \mathrm{e}^{(\epsilon(\mathbf{p},\mathbf{r})-\mu)/k_\mathrm{B}T} - 1} \mathrm{d}\mathbf{p}\ \mathrm{d}\mathbf{r}. \tag{2.3}$$

In a box potential the integration over the position simply yields the volume $\int \mathrm{d}r = V$ and $\epsilon(\mathbf{p}, \mathbf{r})$ is given classically by $p^2/2m$. By substituting $x = p^2/2mk_\mathrm{B}T$ (2.3) gives

$$N_\mathrm{ex} = V\frac{2}{\sqrt{\pi}\lambda_T^3}\int_0^\infty \frac{x^{1/2}}{\mathrm{e}^x/z - 1}\mathrm{d}x, \tag{2.4}$$

where $z = \mathrm{e}^{\mu/k_\mathrm{B}T}$ is the fugacity. The value of the integral is known as the polylogarithm [12]

$$\mathrm{Li}_s(z) \equiv \sum_{n=1}^{\infty}\frac{z^n}{n^s} = \frac{1}{\Gamma(s)}\int_0^\infty \frac{x^{s-1}}{\mathrm{e}^x/z - 1}\mathrm{d}x \tag{2.5}$$

with Γ being the gamma function. Replacing this identity in (2.4) and using $\Gamma(3/2) = \sqrt{\pi}/2$ one finds a simple expression for the density of exited atoms

$$n_{\mathrm{ex}} = \frac{N_{\mathrm{ex}}}{V} = \frac{1}{\lambda_T^3}\,\mathrm{Li}_{3/2}(z). \tag{2.6}$$

This numbers becomes maximal in the case $\mu = 0$ where $z = 1$. By introducing the Riemann zeta function $\zeta(s) \equiv \mathrm{Li}_s(1)$ the critical density of the excited atoms is given by

$$n_{\mathrm{c}} = \frac{N_{\mathrm{c}}}{V} = \frac{1}{\lambda_T^3}\,\mathrm{Li}_{3/2}(1) = \frac{\zeta(3/2)}{\lambda_T^3}. \tag{2.7}$$

If this critical density is reached all exited states are occupied and thus a macroscopic occupation of the ground state will occur. More commonly this is expressed in terms of the phase space density

$$d = n_{\mathrm{c}}\lambda_T^3 \approx 2.612 \tag{2.8}$$

which relates the number density to the thermal de-Broglie wavelength. The phase space density it a good quantity to determine when condensation will occur and it therefore provides the target to optimize the process leading to the production of a Bose-Einstein-condensate.

While a box potential provides good insight into the matter it is an academic example since it is difficult to produce a box potential in reality [13]. In most cases a harmonic potential

$$V(\mathbf{r}) = \frac{1}{2}m(\omega_x^2 x^2 + \omega_y^2 y^2 + \omega_z^2 z^2) \tag{2.9}$$

is used, which is characterized by its trap frequencies $\omega_{x,y,z}$. The term for the energy $\epsilon(\mathbf{p}, \mathbf{r})$ of the atoms then also depends on the potential energy

$$\epsilon(\mathbf{p}, \mathbf{r}) = \frac{p^2}{2m} + V(\mathbf{r}). \tag{2.10}$$

Equation (2.3) still holds an by integrating over space and momentum a similar equation like (2.7) can be obtained for the critical phase space density [11]

$$d = n_c\lambda_T^3 = N_{\mathrm{c}}\left(\frac{k_{\mathrm{B}}T_c}{m\overline{\omega}^2}\right)^{-3/2}\lambda_T^3 = \zeta(3) \approx 1.202 \tag{2.11}$$

where $\overline{\omega} = (\omega_x\omega_y\omega_z)^{1/3}$ is the geometric mean of the trap frequencies. This value is slightly lower than for the box potential but on the same order of magnitude.

2.1.2. The Gross–Pitaevskii equation

The previous section described the an ideal non-interacting Bose-gas. This approximation is good to get an insight to fundamental thermodynamic properties of bosonic gases. Experimentally accessible are only interacting Bose-gases. Although the interaction can be tune to zero in some cases, it is needed to reach thermal equilibrium. It is therefore desirable to describe the Bose-Einstein condensation more thorough by taking interaction into account.

Unlike as in the non-interacting case, it is not possible to simply factorize the many particle wave function $\Psi_N(\mathbf{r}_1, \mathbf{r}_2, \ldots, \mathbf{r}_N)$ into the single particle wave function since the mutual interaction of all particles has to be taken into account. Thus, by introducing the potential $V_{\text{int}}(\mathbf{r} - \mathbf{r}')$ describing the interaction between two particles at the coordinates $\mathbf{r}$ and $\mathbf{r}'$ the time evolution of the field operator $\hat{\Psi}(\mathbf{r}, t)$ in an external potential is given by [14]

$$\begin{aligned} \mathrm{i}\hbar\frac{\partial}{\partial t}\hat{\Psi}(\mathbf{r},t) &= [\hat{\Psi}(\mathbf{r},t), \hat{H}] \\ &= \left[-\frac{\hbar^2\nabla^2}{2m} + V_{\text{ext}}(\mathbf{r},t) + \int \hat{\Psi}^\dagger(\mathbf{r}',t)V(\mathbf{r}'-\mathbf{r})\hat{\Psi}(\mathbf{r}',t)\mathrm{d}\mathbf{r}'\right]\hat{\Psi}(\mathbf{r},t). \end{aligned} \tag{2.12}$$

where $\hat{\Psi}(\mathbf{r}, t)$ and $\hat{\Psi}^\dagger(\mathbf{r}, t)$ are the bosonic field operators that annihilate and create a particle at position $\mathbf{r}$, respectively. For cold and dilute gases only two body s-wave scattering is relevant. Collisions of three and more particles are improbable and the interaction can therefore be described by a simple two-body contact potential

$$V_{\text{int}} = g\delta(\mathbf{r}' - \mathbf{r}) \tag{2.13}$$

where $\mathbf{r}'$ and $\mathbf{r}$ are the coordinates of the two particles. The interaction constant g depends on the s-wave scattering length a

$$g = \frac{4\pi\hbar^2 a}{m}. \tag{2.14}$$

An additional approximation can be used for dilute gases. In case of a macroscopic occupation of the ground state a the field operator of the ground state can be replaced in the mean field description by its expectation expectation value $\langle\Psi(\mathbf{r}, t)\rangle$ plus a small perturbation $\delta\hat{\Psi}(\mathbf{r}, t)$:

$$\Psi(\mathbf{r},t) = \left\langle\hat{\Psi}(\mathbf{r},t)\right\rangle + \delta\hat{\Psi}(\mathbf{r},t). \tag{2.15}$$

This was first developed by Bogoliubov in 1947 [15]. In first order these fluctuations can be neglected and inserting this ansatz into (2.12) leads to the well-known Gross-Pitaevskii equation

$$\mathrm{i}\hbar\frac{\partial}{\partial t}\Psi_0(\mathbf{r},t) = \left(-\frac{\hbar^2}{2m}\nabla^2 + V_{\mathrm{ext}}(\mathbf{r},t) + g|\Psi_0(\mathbf{r},t)|^2\right)\Psi_0(\mathbf{r},t). \tag{2.16}$$

The time evolution of the ground-state wave function is simply proportional to $\mathrm{e}^{-\mathrm{i}\mu t/\hbar}$ [11] an thus the time dependence can be separated out as

$$\Psi(\mathbf{r},t) = \Psi(\mathbf{r})\mathrm{e}^{-\mathrm{i}\mu t/\hbar} \tag{2.17}$$

which leads to the time-independent Gross-Pitaevskii equation

$$\left(-\frac{\hbar^2}{2m}\nabla^2 + V_{\mathrm{ext}}(\mathbf{r},t) + g|\Psi_0(\mathbf{r})|^2\right)\Psi_0(\mathbf{r}) = \mu\Psi_0(\mathbf{r}). \tag{2.18}$$

The first and second term are the contributions of the kinetic energy and the external potential. The third non-linear term quantifies the interaction energy of the mean-field potential which is given by the density distribution $n(\mathbf{r}) = |\Psi_0(\mathbf{r})|^2$. When the atoms are cold enough and the iteration is strong, the kinetic energy term can be neglected in the so-called Thomas-Fermi approximation [16]. r is the size of the BEC and $\overline{r}_{\mathrm{ho}} = (r_{\mathrm{ho},x}r_{\mathrm{ho},y}r_{\mathrm{ho},z})^{1/3}$ the geometric mean of the harmonic oscillators lengths $a_i = \sqrt{\hbar/m\omega_i}$.

This criterion is experimentally usually met and in that case the density profile simplifies to

$$n(\mathbf{r}) = \frac{\mu - V(\mathbf{r})}{g} \tag{2.19}$$

which resembles the shape of the confining potential. In case of a harmonic confinement the BEC has a parabolic density profile. If the condensate is not pure but has a thermal fraction this is visible as a bi-modal distribution.

2.2. Magnetic trapping

Magnetic traps are probably the most widespread method to trap and store cold atomic gases. Since it is impossible to create a local maximum of a magnetic field only states whose energy increases with the magnetic field can be trapped.

For rubidium and potassium these are the states $|1,-1\rangle$, $|2,1\rangle$ and $|2,2\rangle$ from which the latter is normally used. In the simplest case two opposing wire loops

with opposite currents are sufficient to form a magnetic trap. Such a configuration is called quadrupole (QP) trap. If the two coils are placed in an anti-Helmholtz configuration (the relation of the distance a between the coils and their radius r is $a = \sqrt{3}r$), the magnetic field in the center of the trap depends linearly of the position. The characteristic value of such a trap is the magnetic field gradient $B'_z = -2B'_{x,y}$ with z being the symmetry axis of the two coils. A convenient unit used to specify the gradient is G/cm with 1 G (Gauss) $\coloneqq$ 0.1 mT. The physical mechanism of such a quadrupole trap, and magnetic traps in general, is the Zeeman effect. The linear Zeeman effect breaks the degeneracy of the magnetic m_F-substates and it shifts their energy in dependence of an external magnetic field an atom is exposed to by

$$\Delta E = m_F g_F \mu_B |\mathbf{B}|, \tag{2.20}$$

where g_F is the Landé g-factor and μ_B the Bohr magneton. The g-factor depends on the internal fine-structure state of the atom, and turns out to be the same for potassium and rubidium. The energy shift is

$$\Delta E/(h\ m_F) \approx \mathrm{sgn}(g_f) \cdot 700\,\mathrm{kHz/G} \tag{2.21}$$

for the $^2S_{1/2}$ ground state, and

$$\Delta E/(h\ m_F) \approx \mathrm{sgn}(g_f) \cdot 930\,\mathrm{kHz/G} \tag{2.22}$$

for the excited $^2P_{3/2}$ state, where g_f is positive for the $F = 2$ state and negative in the $F = 1$ state.

The potential $U(\mathbf{r})$ acting on the atoms in a quadrupole trap is

$$U(\mathbf{r}) = \mu B'_z \cdot \sqrt{x^2 + y^2 + 4z^2} \tag{2.23}$$

with $\mu = m_F g_F \mu_B$ and it depends on the distance $\mathbf{r}$ from the field minimum [17]. In order to hold rubidium atoms against gravity, a field gradient of 15.3 G/cm is needed for $|2, 2\rangle$ and twice the gradient for the other two states. Potassium requires a gradient of just 7.2 G/cm since it has approximately half the mass.

In such a quadrupole trap the Boltzmann distribution (equation (2.1)) for a thermal gas leads to a Laplace distribution for the density

$$n(\mathbf{r}) = n_0 \mathrm{e}^{-U(\mathbf{r})/k_\mathrm{B}T} = n_0 \mathrm{e}^{-\mu B'_z \sqrt{x^2+y^2+4z^2}/k_\mathrm{B}T} \tag{2.24}$$

and thus the characteristic size of the cloud in the (x,y)-plane is given by

$$r_{x,y} = \frac{k_\mathrm{B}T}{\mu B'_z}. \tag{2.25}$$

The size of the thermal cloud in the z-direction is smaller by a factor of two due to the gradient along the symmetry axis quadrupole trap being twice as large.

A problem for magnetic trapping arises, since the field minimum of a quadrupole trap is always zero. The spin of an atom precesses with the Larmor frequency $\mu B/\hbar$ around its quantization axis. This limits the speed at which the direction of the magnetic field can change, such that the atom can adiabatically follow. At low fields, an atom could move sufficiently fast such that the rate of magnetic field change surpasses this limit. In that case the spin of the atom may flip such that the atom is transferred into an untrapped state and thus lost from the trap. This phenomenon is referred to as a Majorana spin-flip [18]. Since it is more probable to find cold atoms in the trap center, predominately the coldest atoms are lost by this mechanism, thereby leading to an effective heating of the cloud. It is therefore impossible to create a BEC in such a trap.

There are a number of approaches to remedy this problem. One option is to apply an additional optical field at the center of the quadrupole trap. If this field is blue detuned to an optical transition it creates a repulsive potential which "plugs" the hole [17, 19]. The most common alternative is to construct a magnetic potential without field zero. Many possibilities exist but most frequently Ioffe-Pritchard (IP) type traps are used. They provide a offset field B_0 and are harmonic in axial direction $B_z = B_0 + B''z^2/2$. In transverse direction the field is linear $B_x = B'x$. The field of a IP type trap is given as follows [16]:

$$\mathbf{B} = B_0 \begin{pmatrix} 0 \\ 0 \\ 1 \end{pmatrix} + B' \begin{pmatrix} x \\ -y \\ 0 \end{pmatrix} + \frac{B''}{2} \begin{pmatrix} xz \\ yz \\ z^2 - \frac{1}{2}(x^2+y^2) \end{pmatrix}. \tag{2.26}$$

A IP trap operates in two different regimes. At high temperatures where $k_\mathrm{B}T > \mu B_0$, the linear term dominates in radial direction $U_\rho = \mu B'\rho$ which gives a strong confinement as typical for linear traps. At low temperatures where $k_\mathrm{B}T < \mu B_0$, the trapping potential can be well approximated by the potential of a 3D anisotropic harmonic oscillator. Thus for small clouds (and condensates) the potential is given by

$$U(\rho, z) \simeq \frac{\mu}{2}(B''_\rho \rho^2 + B'' z^2) \tag{2.27}$$

where

$$B''_\rho = \frac{B'^2}{B_0} + \frac{B''}{2}. \tag{2.28}$$

such a trap can be fully characterized by its trap frequencies, with a characteristic size of a thermal cloud of

$$r_{x,y,z} = \sqrt{\frac{k_\mathrm{B}T}{m \cdot \omega^2_{x,y,z}}}. \tag{2.29}$$

The trap frequencies strongly depend on the offset field B_0 (2.28) with $\omega_\rho \propto 1/B_0$. That means the offset field has to be low enough to provide sufficient confinement but high enough to avoid losses due to spin flips. Usually an offset field of around 1 G is a good compromise between trap frequencies and stability.

One possible realization is the so-called QUIC (QUadrupole Ioffe Coil) trap. It is constructed by adding an additional coil perpendicular between the anti-Helmholtz coils of a normal quadrupole trap, this coil is called Ioffe coil. The lifetime of the atoms in such a trap is mainly limited by collisions with the background gas and technical noise (e.g., noise in the current flowing through the coils). The quadrupole-Ioffe trap which was built in the course of this thesis and which is described in subsection 4.5.2 allows to store cold atoms for over 200 s.

2.2.1. Evaporative cooling

The atoms are cooled in such traps using evaporative cooling. The hottest particles are removed such that the rest of the ensembles rethermalises at a lower temperature. For a efficient evaporation high trap frequencies are necessary such that the rethermalisation rate is much higher than the loss rate. The hottest atom are usually removed by using the following methods

- Transferring the hottest atoms into a state which is not trapped. This is usually done in magnetic traps using electromagnetic radiation (in the radio frequency of microwave regime). One often describes that as a “knife” which cuts the atoms out of the trap. Due to their higher thermal energy the hottest atoms are in the outer regions of the trap. They can be selectively addressed by the electromagnetic field due to the magnetic field dependence of the transitions. For potassium and rubidium two possible transition can be driven by the field:

  - The atoms can be transferred to an untrapped m_F-state in the same hyperfine manifold using a radio frequency radiation to couple adjacent m_F levels. For example from $|2, 2\rangle$ to $|2, -2\rangle$.
  - The atoms can be transferred into a different hyperfine manifold using a microwave field. For example from $|2, 2\rangle$ to $|1, 1\rangle$. This method has the advantage that rubidium can be cooled independently from potassium since their hyperfine splitting is different.

- Lowering the depth of potential such that the hottest atoms are not trapped any more. This method is often used in optical dipole traps (see section 2.3). It has the disadvantage that the trap frequencies simultaneously decrease such that the evaporation gets less efficient.

In this experiment both methods are used. First the rubidium atom are evaporated using microwave radiation at 6.8 GHz. The potassium is then cooled sympathetically by collisions with the rubidium. At a later stage the atom are transferred to an optical dipole trap where they are evaporated by lowering the potential depth.

2.3. Optical trapping

While being easy to implement, the trapping in magnetic potentials described in section 2.2 has two major drawbacks. The first one is that not all magnetic m_F-substates are trappable which restricts possible applications on these trappable states. In particular for clock applications [20] it can be desirable to be able to vary the m_F state to avoid the effect of external magnetic fields. Secondly and more importantly the magnetic field is not available as a free parameter. The manipulation of the external magnetic field can for example be used to steer spinor dynamics [21] which can be used to create twin Fock states [22] for interferometry. Furthermore the magnetic field can be used to address magnetic Feshbach resonances (see section 2.6) which are used in this thesis to control the scattering properties of potassium. Therefore it is desirable to have an all-optical trapping potential to confine the atoms.

2.3.1. Optical dipole trap

A far off-resonant optical dipole trap (FORT) is such an all-optical trapping potential. To form it one or more light beams are focused onto the atoms. Physically,

the potential arises from the dynamic polarizability α of the atoms [23] where α quantifies the dependence of the amplitude $\mathbf{p}$ of the induced atomic dipole moment by an external field $\mathbf{E}$

$$\mathbf{p} = \alpha \mathbf{E}. \tag{2.30}$$

The resulting dipole trap potential is given by

$$U_{\mathrm{dip}}(\mathbf{r}) = -\frac{1}{2}\langle \mathbf{pE} \rangle = -\frac{1}{2\epsilon_0 c}\Re(\alpha) I(\mathbf{r}), \tag{2.31}$$

which depends on the real component of α. The intensity I is given by $I = \frac{1}{2}\epsilon_0 c \mathbf{E}^2$. The angular brackets denote the time average. The potential is attractive if the polarizability is positive. That is the case for red-detuned light. It is negative and repulsive for blue-detuned light. For a wavelength of $\lambda = 1064\,\mathrm{nm}$ the polarizability[1] is $1.13 \times 10^{-38}\,\mathrm{Cm}^2/\mathrm{V}$ for rubidium and $0.99 \times 10^{-38}\,\mathrm{Cm}^2/\mathrm{V}$ for potassium [25]. For many applications it is more practical to use red-detuned light such that a simple Gaussian beams can be used to trap the atoms. For a Gaussian beam with a waist w_0 and power P, the intensity is given by

$$I(r, z) = \frac{2P}{\pi w_0^2}\left(\frac{w_0}{w(z)}\right)^2 \mathrm{e}^{-\frac{2r^2}{w(z)^2}}. \tag{2.32}$$

It depends on the waist

$$w(z) = w_0\sqrt{1 + \frac{z}{z_{\mathrm{R}}}} \tag{2.33}$$

where

$$z_{\mathrm{R}} = \frac{\pi w_0^2}{\lambda}. \tag{2.34}$$

is the Rayleigh length which is the distance after which the intensity falls to half its value at the focus position. It is therefore in most cases not practical to form optical dipole trap from a single beam, because the confinement along the axial direction of the beam would be too weak to hold the atoms. A single-beam dipole trap for rubidium at 1064 nm and a waist of 180 µm would have a trap frequency of 92 Hz radially and 0.1 Hz axially. To increase the trapping in the axial direction, a crossed dipole trap is usually used. It is constructed by crossing two beams, ideally at an angle of 90°.

[1] If the polarizability α is given in units of a_0^3, it can be converted into SI-Units by $\alpha[\mathrm{Cm}^2/\mathrm{V}] = 4\pi\epsilon_0\alpha[a_0^3]$ [24].

2.3.2. Optical lattices

Optical lattices are a special case of an optical dipole trap. Most simply they are formed by retro-reflecting a dipole trap beam and thus forming a standing wave. This results in the creation of a periodic potential along the dipole axis of the form

$$U_{\mathrm{lat}}(x) = -U_{0,\mathrm{lat}} \cdot \cos^2(kx), \tag{2.35}$$

where k is the wavenumber $k = 2\pi/\lambda$ depending on the wavelength λ of the applied light and $U_{0,\mathrm{lat}} = 4 \cdot U_{\mathrm{dip}}(0)$.

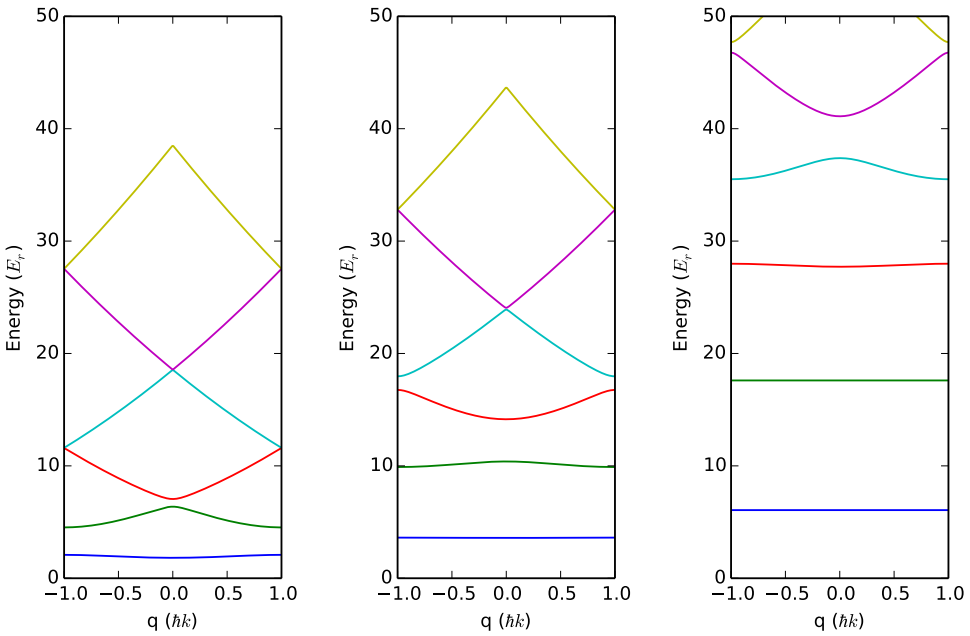

(a) $s = 5$ (b) $s = 15$ (c) $s = 40$

Figure 2.1.: Band structure of an optical lattice for different values s of the lattice depth in the first Brillouin zone.

The lattice depth $s = U_{0,\mathrm{lat}}/E_r$ is usually given in units of the photon recoil energy $E_r = \hbar^2 k^2/(2m)$. The periodicity of the potential causes the eigenstates of the system to organize into bands. This can be seen by solving the time-independent Schrödinger-equation

$$-\frac{\hbar^2}{2m}\frac{\mathrm{d}^2}{\mathrm{d}^2 x}\Psi(x) + U_{\mathrm{lat}}(x)\Psi(x) = E\Psi(x) \tag{2.36}$$

for this potential. For an infinite potential the solution is given by Bloch waves

$$\Psi_{n,q}(x) = \mathrm{e}^{\mathrm{i}qx/\hbar} \cdot u_{n,q}(x) \tag{2.37}$$

according to Bloch's theorem [26]. The function $u_{n,q}(x) = u_{n,q}(x+a)$ has the same periodicity as the optical lattice where $a = \pi/k = \lambda/2$. Here q is identified as the quasi-momentum and n the band index. Thus the periodic functions $u_{n,q}(z)$ and $U_{\mathrm{lat}}(x)$ can be written as Fourier series

$$u_{n,q}(x) = \sum_{l=-\infty}^{\infty} c_{l,n,q} \mathrm{e}^{\mathrm{i}2lkx} \tag{2.38}$$

$$U_{\mathrm{lat}}(x) = \sum_{r=-\infty}^{\infty} U_r \mathrm{e}^{\mathrm{i}2rkx}. \tag{2.39}$$

with the same periodicity. The ansatz for the wave function is now

$$\Psi_{n,q}(x) = \mathrm{e}^{\mathrm{i}qx/\hbar} \cdot \sum_{l=-\infty}^{\infty} c_{l,n,q} \mathrm{e}^{-\mathrm{i}2lkx}. \tag{2.40}$$

After inserting this ansatz into the Schrödinger equation (2.36) and dividing by E_r we obtain the eigenvalue equations

$$\sum_{l=-\infty}^{\infty} \left[\left(2l + \frac{q}{\hbar}\right)^2 + s\cos^2(kx) \right] c_{l,n,q} = \sum_{l=-\infty}^{\infty} \epsilon_{n,q}\ c_{l,n,q} \tag{2.41}$$

for $c_{l,n,q}$ and $\epsilon_{n,q}$. By using the identity

$$s\cos^2(kx) = s\left[\frac{1}{2} + \frac{1}{4}\left(\mathrm{e}^{-\mathrm{i}2kx} + \mathrm{e}^{\mathrm{i}2kx}\right)\right] \tag{2.42}$$

and comparing the terms of the Fourier sum for the potential (2.39) one can see that all therms expect $V_{-1} = V_1 = s/4$ and $V_0 = s/2$ vanish such that (2.41) can be rewritten in a matrix as form [27]

$$\sum_{l=-\infty}^{\infty} H_{l,l'} c_{l,n,q} = \epsilon_{n,q} c_{l,n,q} \quad \text{with} \quad H_{l,l'} = \begin{cases} (2l + \frac{q}{\hbar k})^2 + s/2 & \text{if } l = l' \\ s/4 & \text{if } |l - l'| = 1 \\ 0 & \text{else} \end{cases}. \tag{2.43}$$

By solving this equation the energy eigenvalues $\epsilon_{n,q}$ which form the different energy bands can be determined. A plot of the first six lattice bands in the first

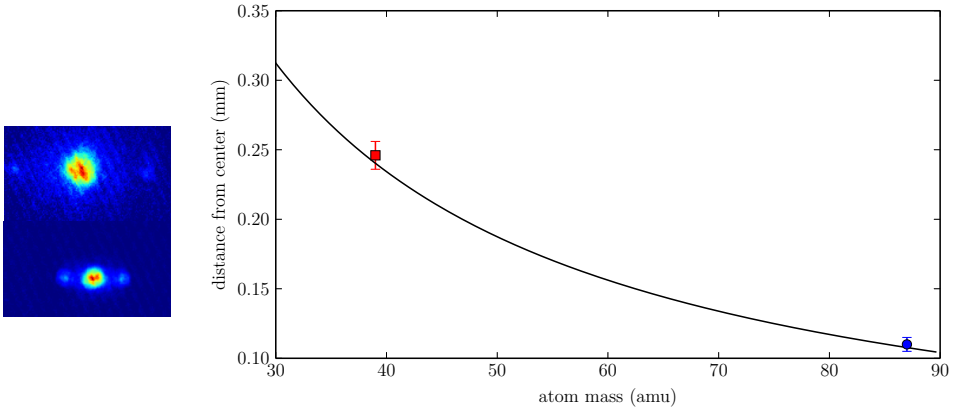

Figure 2.2.: Top left: Potassium 25 ms after the release from an optical lattice. Bottom left: Rubidium after the same time of flight. Two diffraction peaks are visible left and right of the central BEC. The distance of these peaks (^{87}Rb square, ^{39}K circle) is plotted on the graph to the right as a function of the atomic mass. It fits very well with the theory curve that assumed that the atoms got a momentum of $\pm\hbar k$ when being abruptly released from the lattice.

Brillouin (in the range of $q = \pm\hbar k$) is shown for different lattice depths in Figure 2.1 where (2.43) was solved for $l = -10, -9, \ldots, 10$.

A clear indication of an optical lattice is the formation of interference peaks when a BEC is loaded adiabatically into an optical lattice and then released abruptly. That effectively measures the momentum distribution of the BEC in the lattice. This can be seen Figure 2.2 where a picture of potassium and rubidium BECs is taken $t = 25$ ms after they were released from an optical lattice. Three blobs are visible on each picture from which the outer where scattered by the lattice and given an momentum kick of $\pm\hbar k$. Since the mass for rubidium and potassium is different the distance $s_{\mathrm{K,Rb}}(t) = t \cdot \hbar k / m_{\mathrm{K,Rb}}$ of these atoms from the center scales with $1/m_{\mathrm{K,Rb}}$. The graph in the right part compares the measured position with the expected one.

2.4. Laser cooling

Laser cooling utilizes the recoil of scattered photons to cool down individual quantum systems. It is the foundation of the whole experimental field of ultra-cold atoms. Thus the Nobel Prize in physics was awarded to Steven Chu, Claude Cohen-Tannoudji and William D. Phillips for the development of the experimental methods in 1997. It is based on the feature that the photon created during a spontaneous decay is emitted into a random direction. Therefore an atom constantly absorbing photons from a specific direction experiences a net force pushing it into the opposite direction. Typically a red-detuned laser light is used. A photon absorption is thus more probable if the atoms are traveling against the propagation direction of the light as the Doppler shift reduces the detuning.

When six light beams from all spatial directions are used the atoms are decelerated in all three dimensions. Since the temperature of an ideal gas is proportional to the mean squared velocity ($T \propto \overline{v^2}$) a deceleration causes the atoms to cool down. The light field acts like a molasses that slows down the particles entering it. Therefore this configuration is called optical molasses and it provides very efficient cooling. This cooling is velocity dependent and acts only on a small part of the velocity distribution. The Zeeman slower was one of the first setups to increase the effective velocity range by utilizing the Zeeman effect. The effective detuning of the laser light is continuously adjusted while the atom is slowed down by shifting the energy levels with external magnetic field. Initially it was believed that the temperature T limit would be the so-called Doppler limit

$$k_{\mathrm{B}}T = \frac{\hbar\Gamma}{2} \tag{2.44}$$

with Γ being the natural linewidth of the transition used for cooling at an optimal detuning $\delta = -\Gamma/2$ of the light frequency. For ^{87}Rb and all stable potassium isotopes that limit would be 146 µK. In reality, the limit can be much lower due to two features that have been neglected in the Doppler-cooling theory

- Atoms have a rich substructure and can generally not be approximated by a two level system. In the case of alkali atoms the absolute ground state splits into a $2F + 1$ magnetic substates. The energy of the two states shift in dependence of the interaction with the cooling light field.

- The counter-propagating light beams of the optical molasses interfere an thereby form an standing wave. If the light beams have orthogonal polariza-

tions the polarization of the standing wave periodically changes from right circular over linear to left circular.

One possible cooling scenario enabled by these effects can be illustrated for an atom with a ground state doublet with $m = \pm 1/2$. The energy of an atom being in $m = -1/2$ is shifted upwards when it approaches an area in which the red-detuned light is σ^+ polarized. This is due to fact that the interaction probability with the σ^+ polarized light increases. The kinetic energy of the atom is thus converted into potential energy. If the atoms now absorb such a σ^+ polarized photon it is effectively transferred into the $m = +1/2$ state for which the energy is lower than for the $m = -1/2$ at the same point. The atoms has therefore lost kinetic energy. The same process is now repeated for the $m = +1/2$ and afterwards the $m = -1/2$ over and over again. The atom is thus slowly loosing kinetic energy until in the ideal case it is limited by the photon recoil energy

$$k_B T = \frac{(\hbar k)^2}{2m}, \tag{2.45}$$

where k is the wavenumber of the light and m is the mass of the atom. This mechanism is called Sisyphus cooling in resemblance with the poor Sisyphus who has been punished by the greek god Thanatos. His penalty was to keep rolling a huge boulder up a steep hill just to have to see it rolling down after he reached the top.

2.4.1. Magneto optical trap

The optical molasses can only cool atoms but does not trap them, since the force acting on the atoms is only velocity dependent. To trap the atoms, a magnetic quadrupole field is added. In combination with the light field a so-called magneto optical trap (MOT) is created.

Figure 2.3 shows the situation in a MOT assuming an atom with an $F = 0$ ground state and $F = 1$ excited state for simplicity. The upper part of the figure shows two light beams directed onto an atomic cloud. Note that they have the same circular polarization (as defined in the reference frame of each beam).

The lower part of the figure shows the levels structure of the atoms where different cases depending on the direction of the B-field are shown. Since the Zeeman shift of the $|m_F\rangle$ substates depends only on the absolute value of the B-field the level shift is the same for $B > 0$ and $B < 0$. If the atom moves away from the trap center the $|m_F = -1\rangle$ state is pushed closer to resonance. If the atom moves to the

left only the light beam (red in the picture) coming from the left can be absorbed since it is σ_- polarized. The atom is therefore pushed back to the center again. If the atom moves to the right the polarization of the light beams changes with respect to the atom since the sign of the magnetic field changes. Thus only the green (now σ_- polarized) light which comes from the right can be absorbed. The atom is pushed to the center again. By adding four more beams the atoms can be trapped in all three spatial dimensions.

Since the optimal detuning needed for a MOT to trap the maximum amount of atoms is not the same as needed for an optimal cooling in an optical molasses, both techniques are normally combined. After having trapped a sufficient number of atoms in the MOT, the MOT is turned of and a short optical molasses phase is applied to cool the atoms further to the minimal temperature.

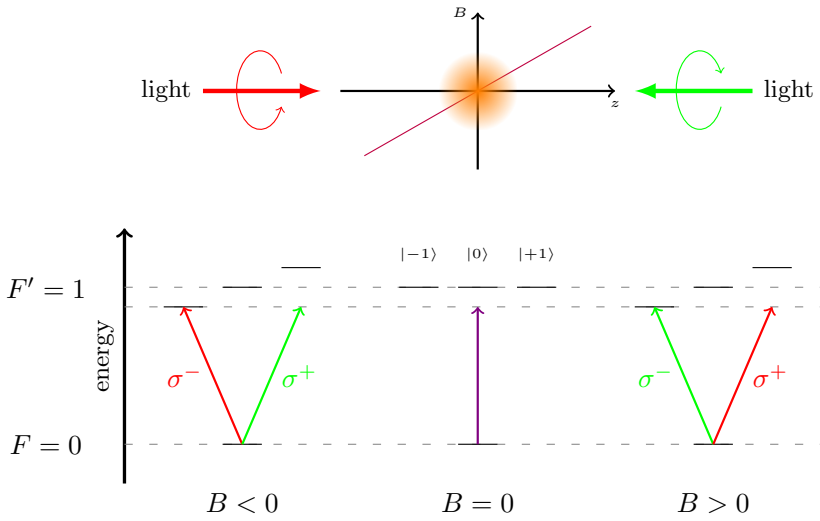

Figure 2.3.: Transitions in a magneto optical trap in 1D in a hypothetical two level atom with two states $F' = 1$ and $F = 0$. In the top: The red light beam is coming from the left while the green one is coming from the right, both having the same circular polarization. The orange cloud depicts the trapped atoms. This sketch also does not account for any Doppler shifts.

In most experimental cases additional repumping light is needed since most atoms have one or more adjacent lines to which they can be excited, leading to loss from the cycling transition. This is the case for rubidium and potassium as can be seen from Figure A.1. Normally the closed $|F = 2, m_F = 2\rangle$ to $|F' = 3, m_F = 3\rangle$ transition is used for cooling. Due to the red detuning there is a finite probability

of exciting the atoms into the $F' = 2$ manifold, which allows the atom to de-exite into $F = 1$. A repump laser is used to pump the atoms into $F' = 2$ from where they may decay back to $F = 2$. Due to the small hyperfine splitting of the excited state of potassium, the amount of repumping power needed for a MOT is significantly larger than for rubidium. In particular for ^{41}K, the same amount of optical power is needed for cooling an repumping such that it would be fair to denote both as cooling light.

A very recent exception is dysprosium for which no repumping light is needed [28]. The dysprosium atoms decay into a meta-stable state with a very high magnetic moment. This allows them to stay in the trap until they decay back into the ground state and thus back to the cooling cycle.

2.5. State preparation with electromagnetic fields

The only facility to manipulate ultra-cold atom is provided by electromagnetic radiation. Figure A.1 shows the level structure of the potassium and rubidium D2 line as an example. A common model to describe the atom-light interaction is the dressed state picture [29] (James-Cummings-Model) which is also used in subsection 2.5.2 to describe the rapid adiabatic passages. In the dressed state model the bare states are written in a product base of the atomic state and a photon fock state. Such that the interaction term of the systems Hamiltonian can only drive transitions of the form [29]

$$|e\rangle|n-1\rangle \longleftrightarrow |g\rangle|n\rangle \tag{2.46}$$

where $|g\rangle$ and $|e\rangle$ are the ground and exited state of the atom an $|n\rangle$ is the photon fock state. If the interaction is mediated by the term Ω, the Hamiltonian of the system can be written for $n = 1$ in matrix formalism by setting the energy reference to the middle of the levels as

$$H = \begin{pmatrix} E_e - \hbar\omega & \hbar\Omega/2 \\ \hbar\Omega/2 & E_g + \hbar\omega \end{pmatrix} \tag{2.47}$$

where $E_{g,e}$ are the energies of the atomic states and ω the frequency of the electromagnetic field. The eigenvectors of the hamiltonian form a new base called the dressed states which have a different energy then the bare states.

When the electromagnetic interaction is used to transfer the atoms between different state either short pulses (subsection 2.5.1) or fast frequency sweeps (subsection 2.5.2) can be used.

2.5.1. Rabi oscillations

When a two level system is perturbed by an external electromagnetic field, the probability of detecting eigenstate $|g\rangle$ or $|e\rangle$ begins to oscillate. This phenomenon is known as Rabi-oscillations and the oscillation frequency is referred to as the Rabi frequency. In the case of an resonant electromagnetic interaction the Rabi frequency is $\Omega_R = |\mu_{eq} E_0/\hbar|$ [30]. E_0 is the electric field amplitude in direction of the polarization x and $\mu_{qe} = -e\langle g|x|e\rangle$ the dipole matrix element. In the case of a off-resonant excitation the Rabi-Frequency is shifted by $\Omega = \sqrt{\Omega_R^2 + \Delta^2}$, depending on the detuning Δ. The probability p_e of finding an atom in state $|2\rangle$ after perturbing the system for the time t is then given by

$$p_e = \frac{\Omega_R^2}{\Omega^2} \sin^2(\Omega t/2). \tag{2.48}$$

When $\pi/2$-pulse with $\Omega t = \pi/2$ is applied, the system is brought into a superposition of the two states. The population probabilities are most sensitive to external perturbations at this point since the absolute value of the slope is maximized. This can be used to construct an atom interferometer. It is a very versatile tool and can be used as an inertial sensor [31, 32], for time measurements [33] or to measure fundamental constants [34, 35].

When the time is chosen such that $\Omega t = \pi$ the population is flipped. This is called π-pulse and can be used to transfer the atoms with a high efficiency to another state. It can be seen that 100% efficiency can only be reached on resonance. In experiments, dephasing causes a damping which limits the maximum transfer. It was previously demonstrated on this experimental apparatus how the dephasing can be minimized [36]). It should also be noted that a π-pulse is intrinsically robust against small unwanted perturbations (e.g., changes to external magnetic fields) due to the zero-crossing of the slope at this position.

2.5.2. Rapid adiabatic passages

An alternative method for transferring atoms to another state are the so-called rapid adiabatic passages [37]. If the frequency of an electromagnetic field coupling two levels is swept across the resonance, the atoms can be transferred between these

two states with high efficiency. In contrast to π-pulses described previously, these sweeps are very robust against small changes of the magnetic field ($< 100\,\mathrm{mG}$). The frequency sweep rate $\mathrm{d}\omega/\mathrm{d}t$ has to be rapid with respect to relaxation processes and slow enough such that the system can follow adiabatically and stays in the eigenstate of the interaction Hamiltonian. This can be expressed in the relation

$$\frac{\Omega}{T_{\mathrm{relax}}} \ll \frac{\mathrm{d}\omega}{\mathrm{d}t} \ll \Omega^2, \tag{2.49}$$

where T_{relax} the relaxation time and Ω is the resonant Rabi frequency of the transition. The relaxation time after which the process becomes incoherent and thus dephases is influenced by the noise and inhomogenities of the fields. The values of both parameters are difficult to determine a priori and thus require an experimental optimization.

To be able to reliably address the target states, a high magnetic field is applied to generate a large the Zeeman splitting. At this magnetic fields, the Zeeman effect becomes non-linear. For the ground states of potassium and rubidium the Breit-Rabi formula can be used to calculate the energies of the $|F, m_F\rangle$ states. It extends the linear term introduced earlier by a quadratic term [38]

$$E_{|F=I\pm1/2,m_F\rangle} = \frac{E_{\mathrm{HF}}}{2} + g_I \mu_B m_F B \pm \frac{E_{\mathrm{HF}}}{2}\sqrt{1 + \frac{4m_F x}{2I+1} + x^2}, \tag{2.50}$$

with

$$x = \frac{(g_j - g_I)\mu_B B}{E_{\mathrm{HF}}}. \tag{2.51}$$

where g_J is the fine structure g-factor, g_I is the nuclear g-factor, μ_B is the Bohr magneton and the hyperfine splitting energy is E_{HF}. The values of these constants an are given in Table 2.1. The nuclear angular momentum of ^{87}Rb and ^{39}K is in both cases $I = 3/2$.

	E_{HF}	g_I	g_J
^{87}Rb (from [38])	$h \cdot 6.834682\,\mathrm{GHz}$	-0.000995	2.002331
^{39}K (from [39])	$h \cdot 461.7\,\mathrm{MHz}$	-0.000142	2.002294

Table 2.1.: Relevant properties of potassium and rubidium to calculate the energy shift due to the quadratic Zeeman effect.

A more detailed understanding can be obtained by calculating the eigenstates of the coupled system. An example should be given for ^{39}K and $F = 1$. The Hamiltonian of this coupled system can be written as

$$\mathbf{H}_{\text{coupled}} = \begin{pmatrix} E_1 - \hbar\omega & \hbar\Omega_{1,0}/2 & 0 \\ \hbar\Omega_{1,0}^*/2 & E_0 & \hbar\Omega_{0,-1}/2 \\ 0 & \hbar\Omega_{0,-1}^*/2 & E_{-1} + \hbar\omega \end{pmatrix}, \tag{2.52}$$

where $\Omega_{i,j}$ are the Rabi frequencies of the oscillation between the coupled states and the energies $E_i = E_{|1,i\rangle}$ are calculated from (2.50).

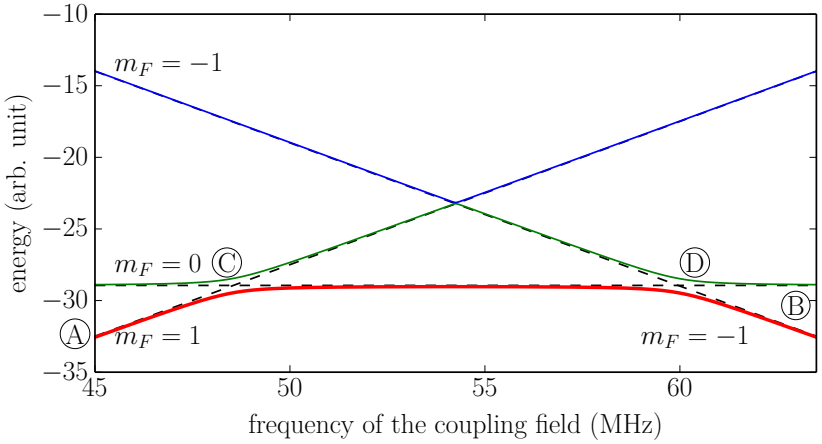

Figure 2.4.: Energies of dressed states of the $F = 1$ ground state of ^{39}K at an offset field of 85 G. A realistic coupling was chosen to show the avoided crossings at Ⓒ and Ⓓ. The eigenstates of the coupled system are depicted blue, green and red and the energies the uncoupled system are dashed. Note that it is not possible to use the avoided crossing between the blue and green line since this transition is forbidden due to selection rules (Δm_F would be 2).

The solution of this three-level system is shown in Figure 2.4, where the frequency of the coupling field was varied. A rapid adiabatic sweep to transfer the atoms from $|1, 1\rangle$ to $|1, 0\rangle$ starts at point Ⓐ where the dressed and bare states are almost degenerate. The frequency of the RF field is swept over the avoided crossing at Ⓒ. When the states are degenerate again at Ⓑ, the RF field would be turned off. The atoms would be projected back on the eigenstates of the bare states such that all atoms are transferred to $|1, 0\rangle$. By the same means the atoms can be transferred from $|1, 0\rangle$ to $|1, -1\rangle$ by sweeping over the resonance at Ⓓ.

Changing the energies of the uncoupled system by varying the magnetic field B has the same effect as sweeping the frequency of the coupling field. This can be an option when a fast change of the magnetic field is easier to accomplish then a fast change of the frequency. In particular when the antenna used to emit the electromagnetic field exhibits resonances exactly within the used frequency range this can provide a practical alternative. In our experiments typical sweeps have the duration of 10 ms while ranging over a few MHz. A fairly high RF-power has to be used, usually on the order of 1 to 10 Watt, since it is difficult to construct efficient antennas for frequencies $< 1\,\mathrm{GHz}$, which have a wavelength of $> 10\,\mathrm{cm}$.

2.6. Feshbach resonances

Feshbach resonances have become a vital tool to influence the scattering length a of ultra cold atoms. At very low kinetic energies E, the wavenumber $k = \sqrt{2mE}/\hbar$ approaches zero and s-wave scattering dominates. Thus the scattering length is a good measure [40] for the total cross section σ_{tot} (for distinguishable particles) according to:

$$\sigma_{\mathrm{tot}} \overset{k\to 0}{=} 4\pi a^2. \tag{2.53}$$

Figure 2.5 shows a simple picture of such a resonance. It occurs when the total energy of two free particles approaches the energy of a bound state in an molecular potential of the two atoms. In that case even a small coupling between the two states allows temporary transitions between the them [41, 42].

These transitions increase the phase shift δ between the incoming and outgoing scattered wave [43, 44]. The scattering length $a = \delta/k$ depends on this phase shift [40] and thus the scattering length is increased near such a resonance.

If the bound state of a molecular potential in the closed channel has a different magnetic moment than the free state the energy difference between two states can changed with an external magnetic field B. That changes the coupling between the two states and thereby the phase shift accumulated by the scattering process. The scattering length then depends on the external field and has a pole at the point at which the two states are in resonance. According to [42, 45] the scattering length $a(B)$ can then be described by

$$a(B) = a_{\mathrm{bg}}\left(1 - \frac{\Delta}{B - B_0}\right). \tag{2.54}$$

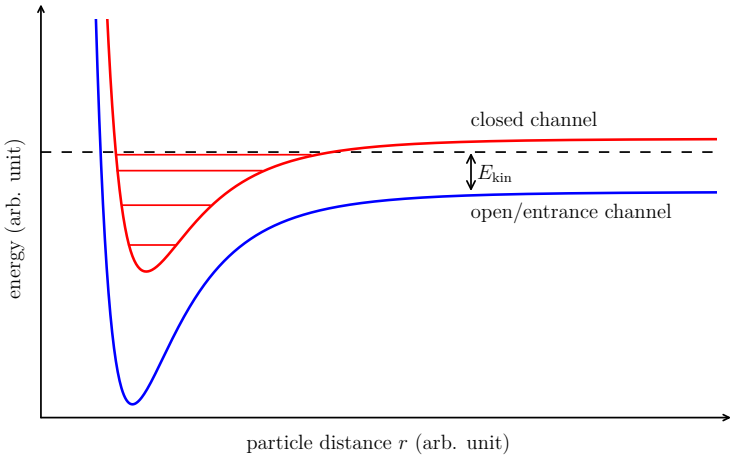

Figure 2.5.: A simple picture of a Feshbach resonance. The blue potential represents the unbound scattering potential of two particles. It is called the open channel, because the asymptotic total energy is lower then the kinetic energy E_{kin} (dashed line). The red potential whose asymptotic energy is higher then the available energy is called the closed channel. It has several bound states (horizontal red lines) from which one approaches the energy of the free particles.

A Feshbach resonance can thus be described by the background scattering length a_{bg}, its width Δ and the magnetic field B_0 at which resonance occurs. When multiple well-separated resonances ($\Delta \ll (B_i - B_{i-1})$) exist the scattering length can be calculated according to

$$a(B) = a_{\mathrm{bg}} \left(1 - \sum_i \frac{\Delta_i}{B_i - B_0}\right). \tag{2.55}$$

In this experimental apparatus we use the Feshbach resonances to tune the negative s-wave scattering length of ^{39}K to a positive value in order to be able to make a Bose-Einstein condensate. Beside being able to just tune the scattering length it is also possible to actually associate molecules using the nearby molecular potentials by sweeping the magnetic field over the resonance [46, 47]. The produced molecules are usually in a weakly bound highly excited state and have to be brought into a deeply bound state [48, 49].

3 Rubidium BECs in optical lattices

This chapter reports on the creation of matter wave packets in a combined magnetic and optical potential. It is based on the research during the first year of my PhD studies and resulted in the publication of two papers [50, 51]. By combining a vertical 1D lattice with a weak harmonic potential provided by the QUIC trap, we have developed a novel method of creating wave packets by applying a weak lattice modulation. Wave packets are non stationary superpositions of energy eigenstates that are spatially localized, and evolve in a similar manner as a classical particle. This chapter is organized as follows: In section 3.1 a brief introduction to the experimental apparatus used for these experiments is given. Some of the experimental techniques are elaborated further in chapter 4, where I describe the apparatus for the condensation of ^{39}K. The main experimental idea is given in section 3.2, where I describe the creation of wave packets. The pump probe spectroscopy with these wave packets is described in section 3.3.

3.1. Experimental setup

The experimental apparatus for the investigation of ^{87}Rb BECs in optical lattices was constructed prior to my PhD. It is described in detail within the PhD thesis by Henrik K. Andersen [27]. In the following a very brief overview shall be given. The apparatus features a 3D MOT that is loaded from the background vapor supplied by commercial dispensers. A round glass cell is used as the chamber for the MOT to provide good optical access. The light for the MOT and detection is generated on a separate optical table and transmitted to the experiment table on which the vacuum system is mounted using optical fibers. The light for cooling and detecting

the atoms is generated by three external-cavity diode lasers.

1. The master laser is frequency-stabilized to the $F = 2$ to $F' = 2/3$ transitions using Doppler-free saturated absorption spectroscopy. It provides the light for the detection resonant to the $F = 2$ to $F' = 3$ transition which can be tuned using a double-pass AOM.

2. The cooling and trapping light is provided by a second laser. A tapered amplifier (TA) is used to amplify the light up to 300 mW. The frequency of this laser is stabilized to the first laser by deriving an error signal from the measurement of their frequency difference.

3. A third laser is independently stabilized by Doppler-free saturation spectroscopy to the $F = 1$ to $F' = 1$ transition. A double-pass AOM is used to shift the laser frequency to the $F = 1$ to $F' = 2$ resonance. That light is used to repump the atoms that have dropped out of the cooling cycle.

After loading a MOT, the atoms are transported in a magnetic quadrupole trap on a translation stage to a region with better vacuum conditions. This is achieved by using a differential pumping stage to isolate the two vacuum sections. A 3D view of that vacuum setup is shown in Figure 3.1. After a first transport stage the atoms are loaded into a second magnetic trap. It transports the atoms to the final science chamber. This two-stage transfer allows the addition of an additional MOT to be able to use another species. This initial goal has been abandoned.

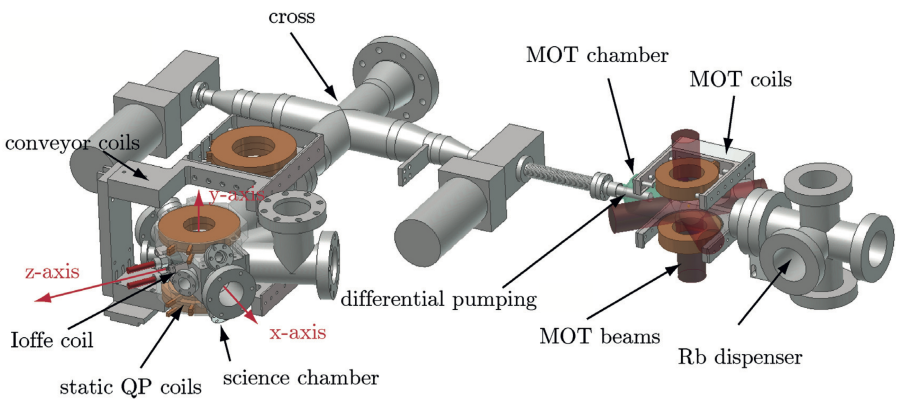

Figure 3.1.: Schematic of the vacuum system of the lattice experiment. Adapted from [52].

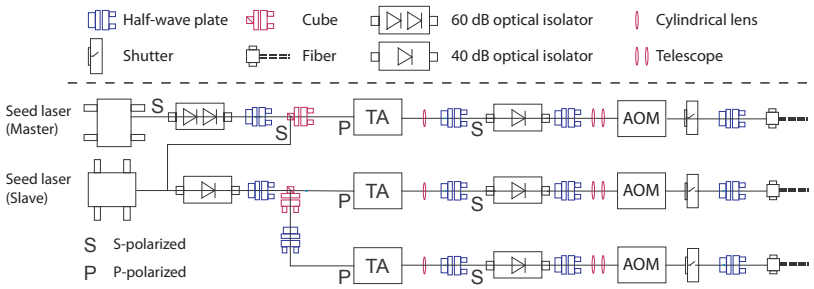

Figure 3.2.: Sketch of the lattice laser system the optical table. Adapted from [27].

In the science chamber the atoms are transferred to a QUIC type magnetic trap. In contrast to the experimental apparatus presented in chapter 4 the evaporative cooling is performed using the radio frequency transitions between the different m_F-states in order to transfer the atoms from the state $|2, 2\rangle$ to $|2, -2\rangle$.

To perform further experiments, the apparatus features a 3D optical lattice at a wavelength of 914 nm. This wavelength is not very common but has the advantage of being closer to optical transitions in rubidium than the more commonly used 1064 nm light. This makes the confinement much stronger since the potential is inverse proportional to the detuning and therefore less power can be used. Semiconductor diodes, providing 1 W of light power, are thus used to create the optical lattice.

A master/slave combination is used to seed three tapered semiconductor amplifiers (TA). The master laser operating at a wavelength of 914 nm can be locked by using a transfer cavity to the rubidium reference laser. A little portion of the light from the master laser is injected into a slave laser to stabilize its frequency to that of the master laser. The light from the slave laser is split and used to seed two amplifier chips while the master laser is used to seed the third amplifier. The light that is provided from the amplifiers is sent through an AOM before being coupled into three fibers, each for one lattice axis. The AOMs are used to stabilize the power after the fiber. It is also used to modulate the power of the lattice beam in order to create the wave packets as described later. Figure 3.2 shows the setup of the lattice on the optical table.

The light coming from the three fibers is then focused onto the atoms resulting in a beam waist of 120 µm. The beams are retro-reflected to produce a total optical lattice of a depth up to 60 E_r for each axis, where $E_r = h^2/(2m\lambda^2)$ is the photon recoil.

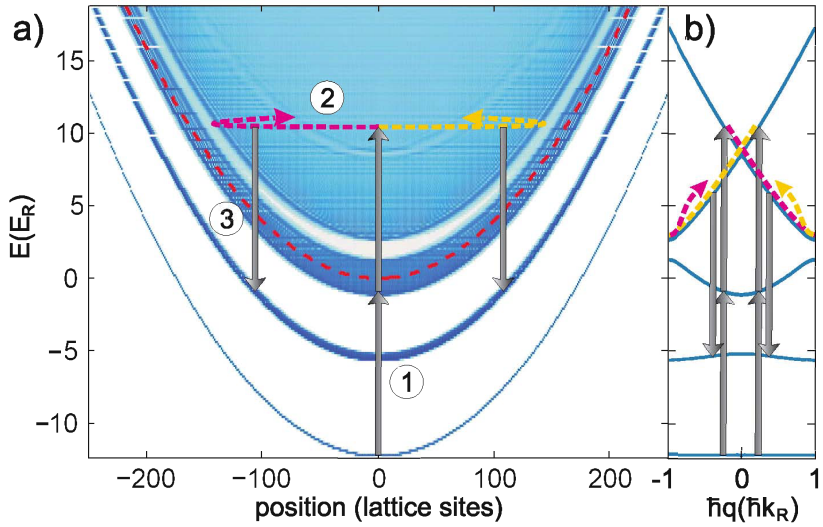

Figure 3.3.: Single particle energy spectrum of a periodic potential with a lattice depth of $16E_r$ and a harmonic potential with $\omega_{\text{trap}} = 2\pi \cdot 37.9\,\text{Hz}$. The density of states is encoded in the blue value and hence white areas indicate energy gaps. The gray upward-pointing arrows visualize a possible two-phonon excitation of a wave packet by a small amplitude modulation of the lattice. The wave packets can then evolve freely until they reach the band gaps where they get reflected or get de-exited by an additional modulation (gray downwards-pointing arrows). The right picture shows the same situation in a band picture.

3.2. Creation of wave packets

For the experimental realization, a BEC of 1×10^5 ^{87}Rb atoms is created in the QUIC trap following a similar scheme as described in subsection 5.5.1. The trap is then relaxed to 12.3 and 37.9 Hz in axial and radial direction, respectively. The atoms are then loaded into a vertical 1D-lattice (along the radial direction of the QUIC trap). The lattice is formed by retro-reflecting a Gaussian light beam at 914 nm with a waist of 120 µm. The lattice depth is adjusted to $16E_r$. The combination of a vertical 1D lattice and a weak harmonic confinement by the QUIC trap along vertical direction is given by

$$U_{\text{comb}}(y) = \frac{1}{2}m\omega_{\text{trap}}^2 - U_{\text{lat}}\cos^2(k_{\text{lat}}y)(1+\epsilon\cos(2\pi\nu_{\text{mod}}t)) \tag{3.1}$$

where m is the mass of the atom, ω_{trap} the trap frequency of the QUIC trap in vertical direction, U_{lat} the lattice depth and k the wavenumber ($k_{\mathrm{lat}} = 2\pi/\lambda$). An additional modulation of the lattice with an amplitude ϵ and frequency ν_{mod} is allowed.

Figure 3.3 visualizes [53] the energy spectrum of the single particle Schrödinger equation in the potential U_{comb}. A darker shade of blue indicates a higher density of states while white areas are forbidden areas visualizing the band gaps. With this spectrum the dynamics presented in the following can be well understood.

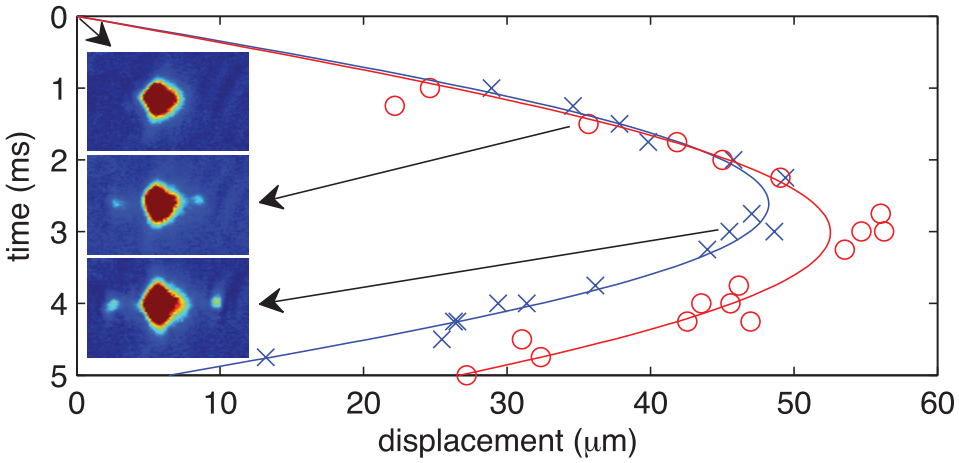

Figure 3.4.: In-situ propagation of the wave packets. The graph shows the position of the upper (×) and lower (○) wave packets. The inset images shows the picture corresponding to the data point marked with an arrow.

The lattice depth is typically modulated by a short 500 µs pulse at a frequency around 30 kHz with an amplitude of $0.3U_{\mathrm{lat}}$. This is close to the transition frequency from band 0 to band 2 at 30.5 kHz. The modulation creates quasi-free wave-packets whose motion in the combined potential can be observed in-situ. Figure 3.4 shows two wave packets traveling outwards within the potential. The wavepackets get back-reflected after 2.6 ms (3 ms for the upper peak). This is clearly not in agreement with the movement in a harmonic potential where a turning point is expected after 6.6 ms for a trap frequency of 37.9 Hz. However, can be understood from an analysis of the band structure. As depicted in Figure 3.3, the wavepacket creation corresponds to a two phonon excitation from the zeroth to an equivalent energy of the fourth band. Due to energy and momentum conservation, the atoms are transferred into states of opposite quasi-momentum $\pm\hbar q_{\mathrm{max}}$, where $4 \leq q_{\mathrm{max}}/k_{\mathrm{lat}} \leq 5$ and the reversal of direction can be understood as a high-order Bragg reflection [54].

In this picture the movement can be calculated by treating the quasi-momentum $\hbar q$ as the momentum p of a classical particle moving in a harmonic trap

$$p(t) = \hbar q_{\max} \cos(\omega_{\text{trap}} t). \tag{3.2}$$

If we now assume that the wavepackets will reach the band gap graph between the bands n and $(n-1)$ at $q_n = nk_{\text{lat}}$ such that

$$p_n = \hbar q_n = \hbar n k_{\text{lat}} = \hbar q_{\max} \cos(\omega_{\text{trap}} t_n). \tag{3.3}$$

Thus the time at which a reflection at the band gap between (n-1)th and n-th band occurs is given by

$$t_n = \cos^{-1}\left(\frac{nk_{\text{lat}}}{q_{\max}}\right) / \omega_{\text{trap}}. \tag{3.4}$$

A reflection at the band gap between second and third band therefore occurs at $t_3 = 3\,\text{ms}$ for $q \sim 4k_{\text{lat}}$. This is in good agreement with the measured turning times in Figure 3.4. This was confirmed by increasing the modulation frequency what caused the atoms to move further outside due to the higher initial momentum. The asymmetry between the upper and lower peak is caused by the gravitational potential.

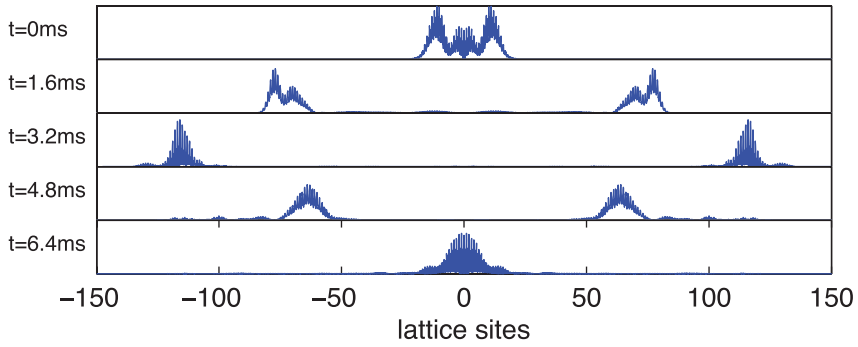

Figure 3.5.: Simulations of the wave packet dynamics.

This simple calculation have also been backed by a more thorough simulation. The outcome of it is shown in Figure 3.5. For the simulation the time-dependent single-particle Schrödinger equation has been solved in the combined potential. In this simulation a wave packet as a superposition of the eigenstates was obtained after the modulation. The simulation reveals a turning point at 3.2 ms in agreement with the simple model.

3.3. Pump-probe spectroscopy

The production of the wave packets can be interpreted as the pump pulse of a so-called pump-probe experiment. In such an experiment a first "pump"-pulse creates exited state wave packets. The wave packets evolve for a variable amount of time, until a second "probe" pulse transfers the population back into the desired target state. This methods can then provide information about the coherent dynamics in the excited state [55, 56]. Additionally the pump-probe probe mechanism can be used for interferometry [57] or for the preparation of a desired state [58]. By using a second modulation to probe the wave packets, they can be de-exited to remote lattice sites separated from the original position by over 100 sites.

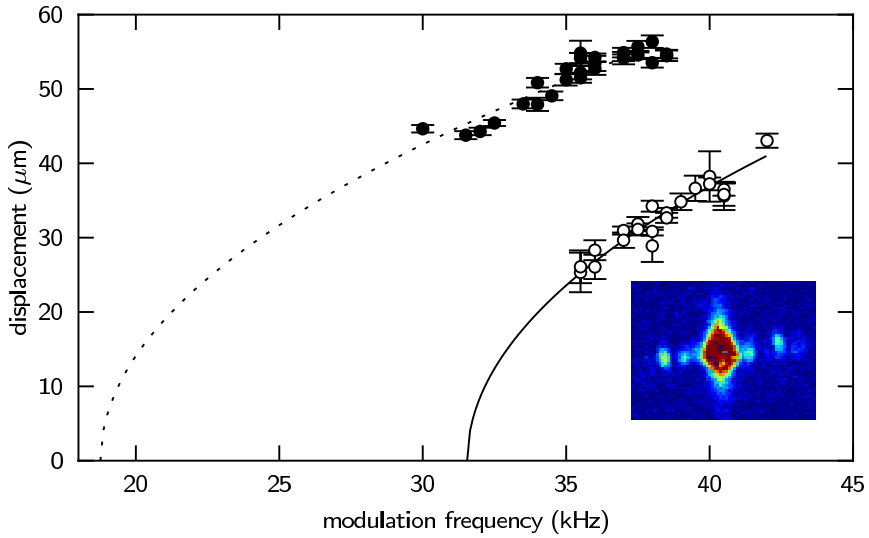

Figure 3.6.: Position of the outer (inner) peaks as a function of the frequency of the probe pulse. The dots (circles) correspond to a localization in the first (second) excited band.

By looking at Figure 3.3 again it can be seen that a second modulation pulse should be able to de-excite the wave packet back into a bound state (depicted by the downwards-pointing arrows). This should create localized states that are held by the lattice. In order to de-excite the wave-packet the energy of the modulation has to match the potential energy of the harmonic trap plus the energy difference to the band $h\nu_{0i}$

$$2h\nu_{\mathrm{mod}} = h\nu_{\mathrm{mod}} + h\nu_{0i} + \frac{1}{2}m\omega_{\mathrm{trap}}^2 x_i^2, \tag{3.5}$$

where i indexes the bands. By solving for x_i an expression for the displacement corresponding to a localization in the ith band depending on the probe frequency is obtained

$$x_i = \sqrt{2h(\nu_{\mathrm{mod}} - \nu_{0i})/m\omega_{\mathrm{trap}}^2}. \tag{3.6}$$

Figure 3.6 shows the results of such an experiment. Here the lattice is modulated for a long time (10 ms) with different frequencies. The harmonic potential is then turned off to remove the remaining fractions of the wave packets and the localized atoms are images in-situ. As it can be seen from the inset of Figure 3.6, which is taken for a modulation at a frequency of 36 kHz, two localized states are visible at certain frequencies. The fits are performed according to equation (3.6) and give $\nu_{01}^{\mathrm{fit}} = 18.5(2)$ kHz and $\nu_{02}^{\mathrm{fit}} = 33.06(17)$ kHz in good agreement to the first (18.1 − 19.3 kHz) and second (30.6 − 37.2 kHz) Bloch bands for a lattice depth of $16E_r$. This shows that the process can be very well described by the proposed band picture.

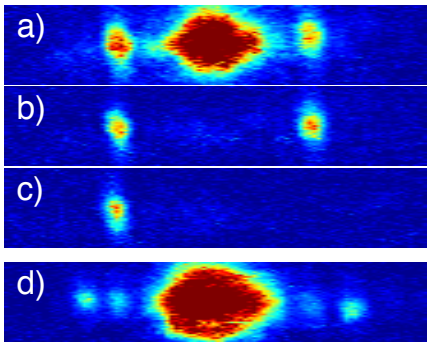

Figure 3.7.: Demonstration of the individual addressing of the localized states. (a) Population after a 10 ms modulation at 30 kHz. (b) Removal of the main peak. (c) Removal of the main and lower peak. (d) Creation of multiple localized states by two probe pulses.

Furthermore the localized states can be manipulated independently. Due to the gravitational sag $g/\omega_{\mathrm{trap}}^2 = 173$ µm each localized state is exposed to a unique magnetic field and can therefore be independently addressed by RF-fields. This was used to demonstrate the selective removal of localized states as shown in Figure 3.7. Additionally, it is also possible by produce multiple localized states by using two probe pulses at different times and frequencies (see Figure 3.7 (d)). This is a promising starting position for future experiments to investigate the coherence

properties of the localized states which could then be used for interferometric experiments.

In a follow up paper [51] we demonstrated that multiply exited wave packets could be produced, moving even further out in the potential due to higher energies. A first application was also presented by using the pump probe spectroscopy to measure the trap an anharmonicity.

4 Experimental setup

The experimental apparatus presented in this chapter has been designed to investigate fundamental properties of various alkali metal isotopes. Currently the three bosonic isotopes ^{87}Rb, ^{39}K and ^{41}K are available for studies. In addition the fermionic ^{40}K could be accessed by a future addition of an ^{40}K-enriched source. The optics for the magneto-optical trap (MOT) have been chosen carefully such that a future extension with lithium and cesium is also possible.

The apparatus is built on two optical tables which provide a grid of M6 threads to mount the optical elements and act as a passive vibration isolation from the ground. Additionally vibrations can be isolated further by floating the table on pressurized air. An overhead rack above the tables provides storage space and includes a flow-box to keep dust away from the sensitive optics. One table contains the lasers and supplementary optics to provide the light needed for cooling and imaging the atoms. The other table contains

- the vacuum system,
- MOT optics & imaging system,
- magnetic traps to transport and store the atoms,
- and the laser and beam shaping optics for the optical dipole trap.

These are the main components of the experiments which are described in this chapter in this order which also roughly resembles the sequence of an experimental run. The relevant calibration measurements are given for ^{87}Rb and the addition of potassium is described in chapter 5.

The experiment was first built at the Leibniz Universität Hannover and has been described in two PhD theses [24, 59]. There the apparatus was used to demonstrate the implementation of an atom laser [60] and investigate an effect called spin self-rephasing to drastically increase the coherence time on the rubidium clock transition [36]. As a part of the work leading to this thesis this machine was moved to the Aarhus University. That resulted in a complete disassembly of the machine in Hanover and a part by part reconstruction in Aarhus.

A complete experimental cycle takes around 30 to 90 s and can be divided into following consecutively executed steps:

- Loading of the 3D magneto-optical trap for 10 up to 25 s from the background vapor.
- Transfer of the atoms into a quadrupole magnetic trap. Hence, the ensemble has to be spin polarized by optical pumping to maximize the efficiency of the transfer.
- A mechanical transport to the region with better vacuum conditions in order to increase the lifetime of the ensemble.
- Transfer into a stationary quadrupole trap.
- Forced evaporative cooling by actively removing only the hottest atoms from the trap by microwave radiation.
- Transfer into a harmonic magnetic trap (a QUIC trap).
- Continuation of the evaporative cooling using microwave radiation.
- Transfer to an optical dipole trap.
- Transfer of the atoms into the desired inner state.
- Evaporation in the optical potential by lowering the intensity of the beam.
- Manipulate the atoms as desired.
- State-dependent imaging the remaining atoms to obtain the results.

Depending on the isotope and the aim of the experimental run only some of these steps may be carried out.

4.1. Vacuum system

The main component of the experimental apparatus is a vacuum chamber that sustains the ultra-high vacuum (down to a few 10^{-11} mbar) which is required for the work with ultra-cold quantum gases. A differential pumping stage divides the vacuum system into two regions that provide the vacuum conditions needed during the different stages of an experimental sequence. To maximize the optical access to the atomic ensemble, glass cells instead of a conventional stainless steel chamber are used both for the MOT and the final experimental region. It is therefore possible to construct small magnetic coils that allow the creation of very high magnetic fields without having to use too high currents.

The vacuum system itself is constructed out of non-magnetic stainless steel tubes that are connected using copper gaskets. The magneto-optical trap and the subsequent evaporative cooling have different requirement concerning the vacuum quality (i.e. the pressure). Since the MOT is loaded from the background gas the partial pressure of rubidium and potassium in the MOT area is a compromise between the MOT loading rate and the lifetime to maximize the number of atoms in the MOT while keeping the loading time reasonably low. This compromise is normally reached at a background pressure of a few 10^{-10} mbar. For the evaporation and future experiments a pressure of about 10^{-11} mbar is needed.

As can be seen in Figure 4.1, a differential pumping stage is used achieve this goal and to divide the vacuum system into two sections. The pumping stage is a 160 mm long tube with an inner diameter of 8 mm. Since the atoms are transported through this tube, the exact dimensions are a compromise between maintaining different vacuum conditions and minimizing the losses during the transport, caused by a too small diameter. The ultra-high vacuum condition is maintained by two ion pumps each on one side of the differential pumping stage. In addition two titanium sublimation pumps are installed to decrease the pressure further if necessary.

The MOT is created in a $140 \times 50 \times 50$ mm glass cell manufactured by *Hellma*. The big cell allows the usage of large-diameter beams to create the MOT. This increases the MOT volume and enables efficient loading from the background vapor. The atoms are supplied by dispensers from *SAES Getters*. The dispensers are metal tubes that contain an alkali metal salt and an Aluminum-Zirconium alloy as the reducing agent. When the dispenser is heated by resistive heating (to temperatures around 500 °C) the salt is reduced by the Zirconium alloy and elementary rubidium or potassium is released through a small slit in the tube. The dispensers are available for different alkali metal species and dispensers that are

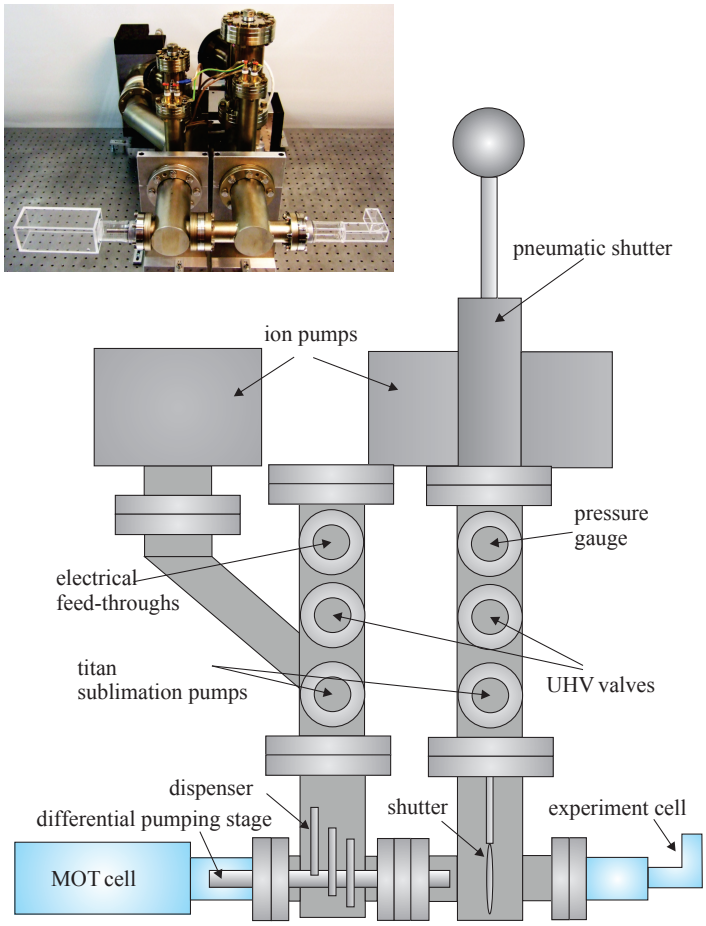

Figure 4.1.: Schematic of the vacuum system is constructed as seen from above. In the top left corner an actual picture of the vacuum system is shown. Adapted from [24].

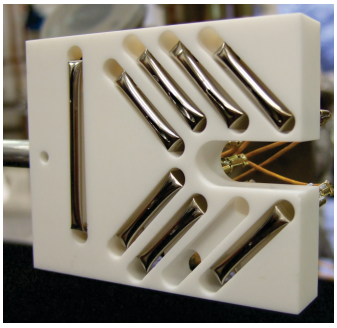

Figure 4.2.: Dispensers on the ceramic holder

enriched with a specific isotope are available as well. They are mounted facing towards the MOT-cell on a ceramic holder as can be seen in Figure 4.2. This mounting allows an efficient release of the rubidium and potassium atoms towards the MOT area. Currently eight dispensers are built into the vacuum system from which only two are known to work reliably as shown in Table 4.1. In case they run out replacement dispensers are stored inside the vacuum system to be able to replace them fast.

#	Element	Manufacturer	Remarks/Status
1	-	-	-
2	^{40}K	old selfmade	?
3	K	SAES	cable defect
4	Rb	SAES	?
5	Rb	SAES	?
6	-	-	-
7	K	SAES	?
8	^{39}K	Alvatec	old one, reused
9	K	SAES	currently used
10	Rb	SAES	currently used

Table 4.1.: Status and type of the dispensers currently build into the vacuum system. The two dispenser that are currently used are the only ones that are known to work. The status of the other ones is dubious.

In addition light-induced atom desorption (LIAD) [61] is used. Therefore four high-power UV-LED arrays from *Roithner Lasertechnik* are placed around the MOT class cell. The ultra violet light emitted by them is able to desorb atoms from the surface of the glass cell. Thus the background pressure can be temporarily increased during the time the MOT is loaded.

On the other side of the differential pumping stage a smaller L-shaped glass cell (25 mm height) is used that is also manufactured by *Hellma*. The small size allows to place the magnetic coils needed for the cooling and manipulation of the atoms very close to the atoms. This reduces the current needed to create the high fields needed for accessing the Feshbach resonances (up to 600 G). The L shape permits free optical access from all sides which is used to create a crossed dipole trap.

The lifetime of atoms stored in the experimental cell would be drastically decreased if a MOT would be operated at the same time due to the enormous amount of near-resonant photons used in the MOT. Thus a pneumatic shutter placed inside

the vacuum system can be used to block the direct line of sight the two chambers. This can be used to load a new MOT while the experiment is running and thus shortening the cycle time or to reload new atoms from the MOT into the magnetic trap.

4.2. Laser setup for trapping and cooling

To pursue optical cooling of the atoms (section 2.4) light of various well-defined frequencies is needed. The bandwidth of the radiation needed for the cooling and trapping of potassium and rubidium has to be about one MHz well below the natural linewidth of the used transitions of 6 MHz. Such high frequency relative precision of $\approx 3 \times 10^{-9}$ can only be achieved by using an actively stabilized laser. With the advent of high quality laser diodes these setups can be very compact without sacrificing maintainability and expandability. The laser setup that will be discussed in this chapter is build on a standard optical table using 2.54 cm (1 inch) diameter mirrors. The setup consists of two different independent laser systems, one for rubidium and one for potassium. Both systems generate light for the following applications:

- Light for cooling and trapping the atoms: For both potassium and rubidium the closed $F = 2$ to $F' = 3$ transition on their D2 line (767 nm and 780 nm respectively) is used.
- Light to repump atoms back into the cooling cycle. This is necessary since the cooling light has a finite probability to excite atoms into the $F' = 2$ instead of the $F' = 3$ state. From this state they may deexcite into the $F = 1$ state and are then lost for the cooling cycle.
- Light to pump the atoms into the $|2, 2\rangle$ state after the optical cooling and loading them into the magnetic trap.
- Light resonant to the $F = 2$ to $F' = 3$ transition to detect atoms in the $F = 2$ state.

Figure 4.3 and Figure 4.4 show the transitions used for cooling potassium and rubidium. The detunings are large in the case of potassium since the hyperfine splitting is so small. For ^{39}K a power ratio between cooler and repumper of $2 : 1$ is used, ^{41}K even requires a ratio of $1 : 1$, while ^{87}Rb only requires a few milliwatts of repumping power

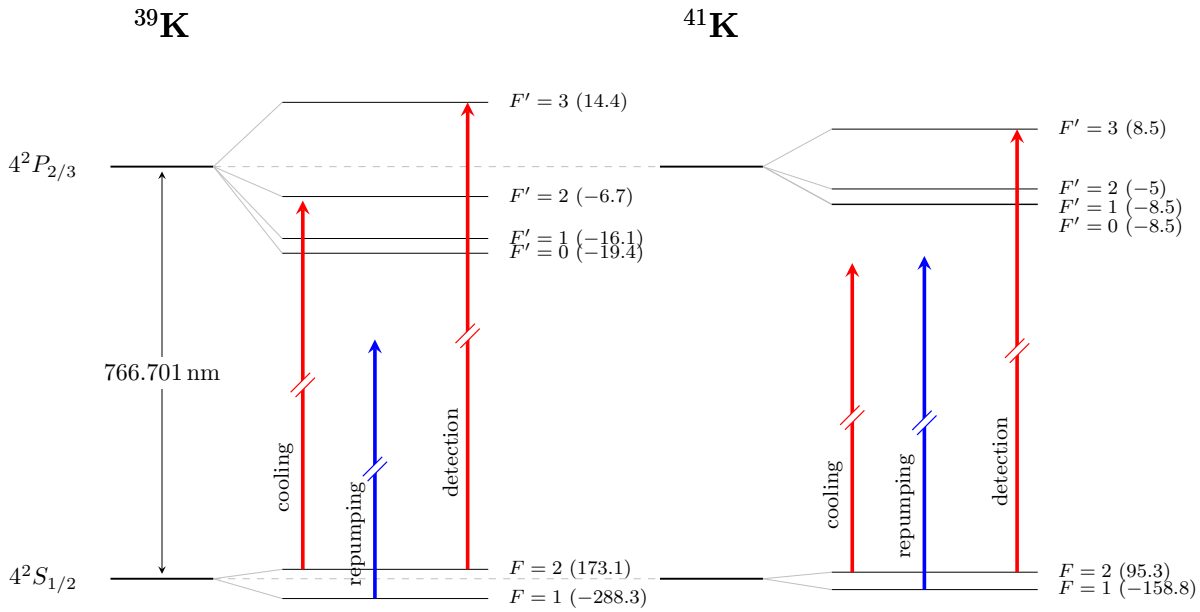

Figure 4.3.: Cooling transitions in ^{39}K and ^{41}K. The endpoint of the arrows depicts the detunings used to cooling and repump laser and is to scale with the splitting of the exited levels. See Table 5.1 for the numerical values.

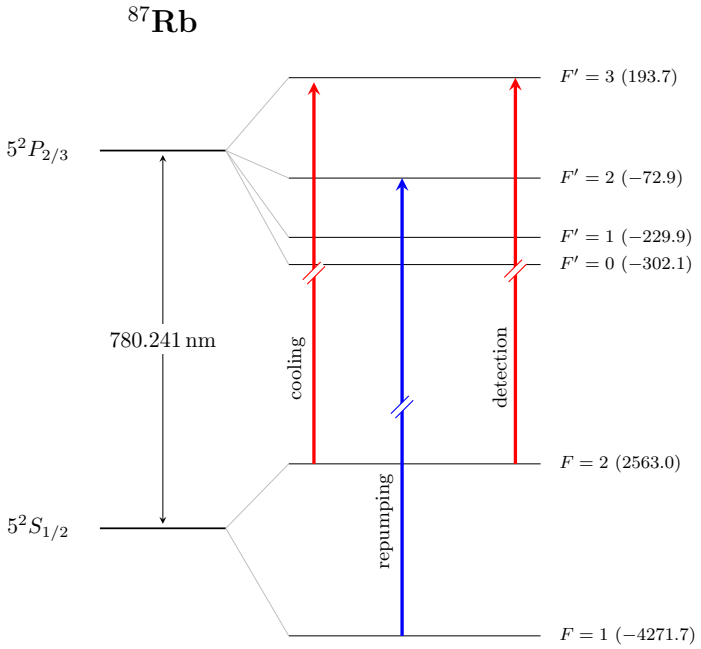

Figure 4.4.: Cooling transition in ^{87}Rb. The cooling laser is red-detuned by 4Γ.

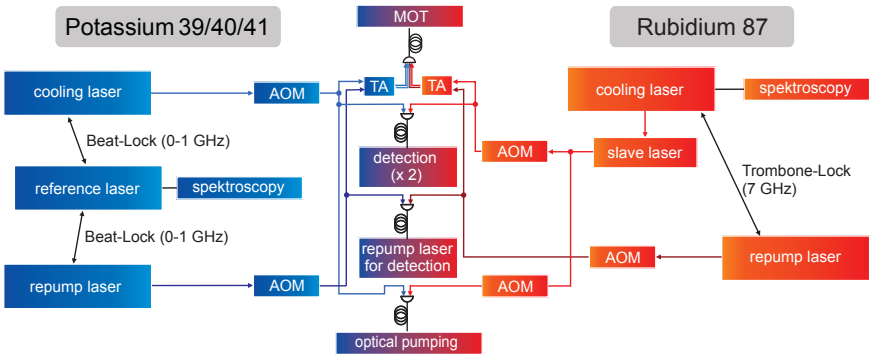

Figure 4.5.: Block diagram of the complete laser system. Adapted from [24].

4.2.1. Rubidium laser system

The rubidium laser consists of three diode lasers and one tapered semiconductor laser amplifier, as can be seen in Figure 4.6. Two of them are grating stabilized external cavity diode lasers (ECDL) (the design is described in [62]). The cooler master laser is a commercial *DL-100* laser from *Toptica* the second one is a home built model. The third laser is an injection locked laser which is stabilized in frequency by injecting light of the first laser into it.

The *DL-100* laser acts as an absolute frequency reference for the other lasers. Using saturated absorption spectroscopy [63] this laser is stabilized with an electronic servo loop to an atomic transition. To maximize the signal-to-noise ratio for the stabilization, the strong crossover line between the $F = 2$ to $F' = 2$ and the $F = 2$ to $F' = 3$ transition is chosen for that purpose. The light used for the spectroscopy is shifted upwards in frequency by 300 MHz using an acousto optical modulator (AOM) in double-pass configuration before being fed into the spectroscopy path. Thus the laser effectively lases at a frequency that is much lower than required. This complication is added such that the stabilized light can afterwards be tuned over a wider range utilizing a second AOM.

The second ECDL laser is used to provide light to repump the atoms. The frequency is stabilized to the reference laser by measuring the beat frequency between the two lasers. The frequency difference of the two lasers is due to the hyperfine splitting of the ground state around 6.8 GHz. To measure the beat frequency two light beams, one from each laser, are superimposed on a high speed photo diode. The resulting signal is split up and sent through cables of different length and then recombined. This produces interference fringes in the frequency domain. A phase shifter is used to shift the zero crossing of such a fringe to the

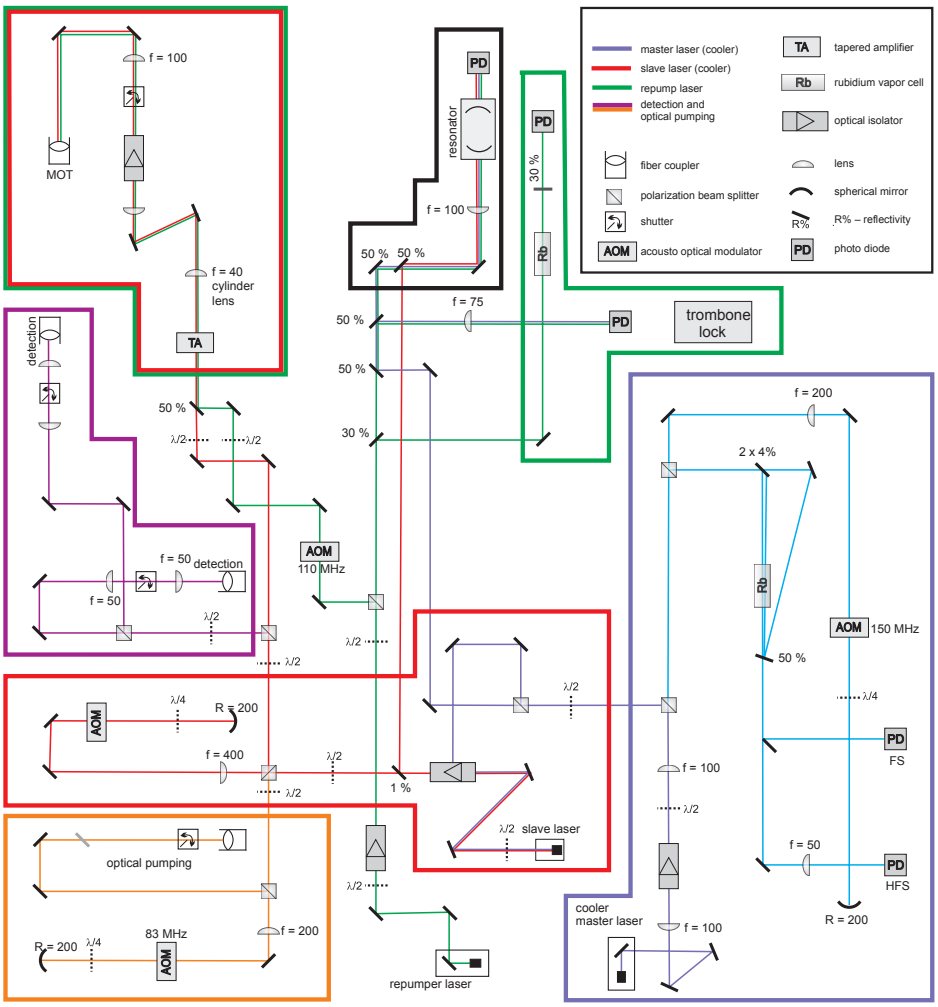

Figure 4.6.: Drawing of the rubidium laser system. Adapted from [59].

designated frequency [64]. Based on this error signal an electronic servo loop is used to stabilize the laser frequency of the repump laser with respect to the reference laser.

A small portion of the reference light is fed into a slave laser. Due to this seeding the slave laser operates at the same frequency as the master laser [65]. The advantage of using a slave laser, is that it provides considerably more output power (70 mW vs. 30 mW) than the reference laser. The light from the slave laser is then split into two paths. A small portion is fed into a double-pass AOM to shift the laser frequency up by 166 MHZ to be resonant to the $|2, 2\rangle$ to $|3', 3\rangle$ transition for optical pumping. The major portion of the beam is shifted up in frequency by 412 MHZ to provide light for laser cooling and imaging, again using a double-pass AOM. After splitting off 1 mW for imaging the rest of the light is used to seed a tapered amplifier.

The tapered amplifier is a semiconductor diode that is used to amplify light. It has a tapered region to suppress amplification of spontaneous emission in the backward direction while providing enough amplification in the forward direction [66]. The light for cooling and repumping are superimposed in front of the tapered amplifier using a 50 : 50 beam splitter. The light is then amplified up to 800 mW and coupled into a fiber to send it to the experiment table.

4.2.2. Potassium laser system

The laser system for cooling and manipulating potassium, from which a drawing is shown in Figure 4.7, is built more flexible than the system for rubidium. In order to be able to easily switch between the different isotopes, the lasers providing the light for cooling and repumping are both frequency stabilized to a master laser.

Doppler-free absorption spectroscopy is used to frequency stabilize the master laser to an atomic transition which then acts as a frequency reference for the two other lasers. Since ^{39}K has the highest natural abundance of the three stable isotopes the $F = 2$ to $F' = 2/3$ crossover transition is chosen for this purpose. A double-pass AOM is used to shift the frequency up by 320 MHz before the light is fed into the spectroscopy path.

The two lasers providing light for cooling and repumping are stabilized to this master laser by measuring the respective beat frequencies on separate photo diodes. A polarization beam splitter is therefore used after each laser to split off a small portion of the light beam to illuminate respective photo diodes. The signal coming from each photo diode is filtered amplified to improve it. Afterwards a phase

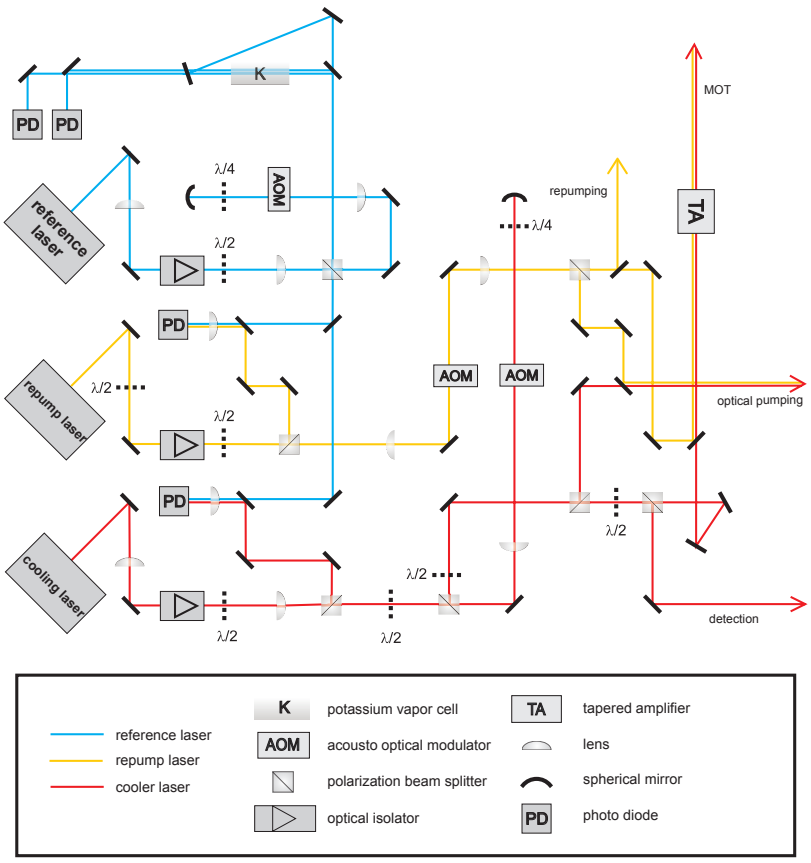

Figure 4.7.: Drawing of the potassium laser system. Adapted from [67].

.

detector compares the frequency of the beats with reference signals provided by computer-controllable synthesizers. From this an error signal is derived which is used to stabilize the cooling-/repumping-lasers with respect to the master laser using a feedback loop. Thus it is possible to change to a different isotope by simply changing the reference signal, this can even be done remotely from within the computer control program.

The light used for prepumping is send through an AOM to be able to shift fast enough such that it can be used for the MOT, molasses and optical pumping. A small part of the light is split off after the AOM to be used to repump from $F = 1$ to $F = 2$ prior to imaging. While another small portion is split of the beam to be used for optical pumping, the majority of the beam is used to seed an tapered amplifier in order to have enough light power for the MOT.

The light for cooling the atoms on the cycling transition is coupled into a double-pass AOM to be able to shift the frequency of this light as well. The cooling laser provides also light for imaging the atoms and therefore a small portion of the beam is split of right in front of the tapered amplifier. Another small part of the beam is split of for optical pumping and superimposed with the repumper light in order to pump the atoms to the $|2, 2\rangle$ state prior to the magnetic transport. The main part of the light provided by the cooling laser is used for the MOT. Thus the main beams coming from the two lasers are superimposed on a $50 : 50$ beam splitter and afterwards in a tapered amplifier to a combined power of 1 W.

In contrast to the rubidium system much more repump light is required for the cooling of potassium. ^{39}K requires a power ratio (cooler:repumper) of $2 : 1$ and ^{41}K a ratio of $1 : 1$. To measure the power ratio a cavity is used where the power of the different frequency components can be related to the heights of the interference peaks. This effort is necessary since the amplification characteristic of a tapered amplifier is highly nonlinear and the light frequencies are too close to be separated by optical elements. AOMs are used to adjust the exact power ratio by regulating the RF-power used to operate them. The ability to adjust the powers is especially important for the optical molasses.

The light beams produced for optical pumping, imaging, repumping and MOT are all superimposed with their counterpart from the rubidium laser system. To maintain a high efficiency dichroic mirrors are used for that. The combined beams are then coupled into the same fiber. Since the wavelength of the light needed for rubidium and the one needed for potassium is similar this is possible without any bigger problems. Additionally a lot of the complexity of using two species is effectively removed from the experimental apparatus and kept on the laser table. This makes the optical setup around the vacuum system very reliable as it does not have to be realigned due to the intrinsic stability provided by an optical fiber.

4.3. Magneto optical trap

The MOT is built on the second table. The light for the cooling of potassium and rubidium is guided to the experiment table using a single fiber. Thus the alignment of the MOT is decoupled from the alignment of the rest of the laser system. Achromatic optics are used for all optical elements such that no realignment is necessary for the different atomic species such that they can be used at the same time. At the beginning the fiber out-coupler collimates the beam to 2.25 mm. At this point a power of 180 mW for rubidium and 300 mW for potassium are available.

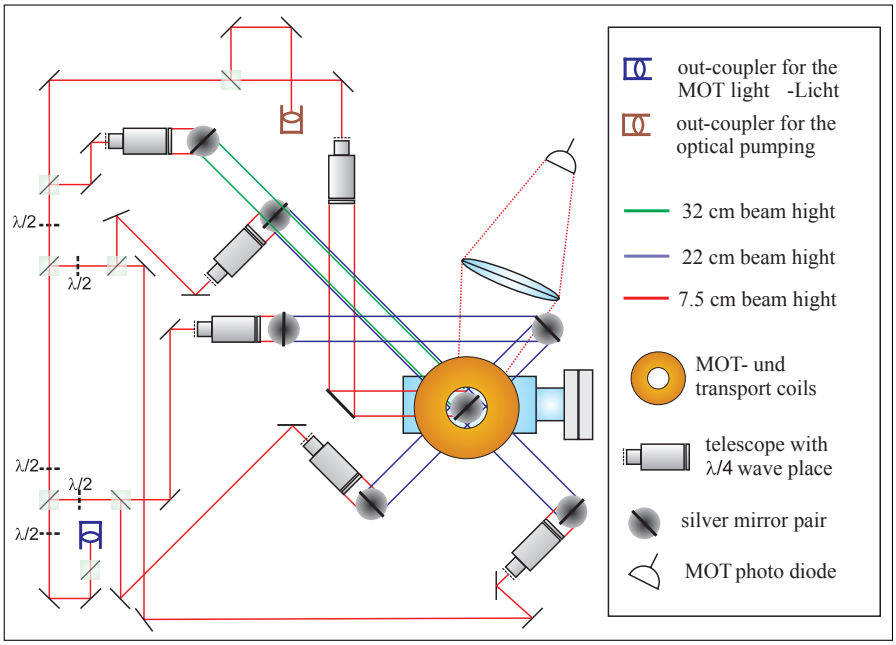

Figure 4.8.: Sketch of the optical MOT setup as seen from above. The different beam heights are color coded. From [59].

Afterwards the light is split into six beams using polarization beam splitters into. In conjunction with achromatic half-wave plates this allows to precisely adjust the power balance between the beams. This is important since the optical molasses is especially sensitive to a mismatch of the optical power.

Since it is so sensitive huge coils are attached around the whole table in order to compensate the magnetic field at the place of the MOT to improve the optical molasses. Initially these coils were also used to compensate the magnetic field in the stationary magnetic trap (see section 4.5) until is was noticed that they affected the experimental apparatus in the adjacent lab. Thus much smaller compensation coils were installed around the stationary trap and the MOT compensation coils are kept at a constant field for the whole time.

After the beams are split, telescopes are used to magnify the beams to a diameter of 50 mm. This is done (a) in order to increase the trapping volume and (b) to be less sensitive to drift in the beam pointing. Since the MOT requires circular polarized light to work, a quarter-wave plate is used just in front of the telescopes to change the polarization from linear to circular. The circular polarization is not maintained optimally by the dielectric reflective coatings such that silver coated mirrors are used after the telescopes. The mirrors have a size of 50×70 mm and a

reflectivity of 97%. Two beams provide cooling in the vertical direction while the four remaining beams provide cooling in the horizontal plane. They are brought to a high of 22 cm above the table and then directed towards the center of the magneto optical trap. This setup is shown in Figure 4.8. To monitor the MOT, two cameras are installed which show the MOT from the side an above. To quantify the number of atoms acquired in the MOT a $f = 80\,\mathrm{mm}$ lens is used to collect the fluorescent light of the MOT on a photo diode using a $2f$ imaging. The total power of the light that is emitted by the MOT is

$$P = N\hbar\omega_0\Gamma_{\mathrm{sc}} \tag{4.1}$$

where

$$\Gamma_{\mathrm{sc}} = \frac{\Gamma}{2}\frac{I/I_{\mathrm{sat}}}{1 + I/I_{\mathrm{sat}} + (2\Delta/\Gamma)^2} \tag{4.2}$$

is the photon scattering rate according to [68]. The linewidth Γ and the saturation intensity I_{sat} can be found in the literature [38]. The voltage U_{PD} measured at the photo diode also depends on the sensitivity of the photo diode and the solid angle in which the light is collected by the imaging lens. Taking this into acount the total number of atoms in the MOT is [24]

$$N \approx 1 \times 10^9 \mathrm{atoms/V} \cdot U_{\mathrm{PD}} \tag{4.3}$$

with a MOT detuning of 22 MHz and a light intensity at the place of the atoms of approx $\approx 50\,\mathrm{mW/cm^2}$.

The MOT setup has turned out to be very robust and insensitive against slight misalignment. To adjust the light beams for the MOT a geometric alignment with respect to the center of the magnetic trap is sufficient. The power of the beams can be balanced using a optical power meter by adjusting the half-wave plates.

After the MOT and optical molasses phase the atoms are equally distributed in all m_F sub states. In order to facilitate an efficient transport the atoms are pumped into the $|2, 2\rangle$ state. The trapping potential is strongest for this state that reduces the losses at the thin differential pumping stage. To transfer atoms into $|2, 2\rangle$ state an offset field of 15 G is applied to provide a defined quantization axis. Additional coils attached to the transport coils provide a field of $B/I = 1.46\,\mathrm{G/A}$. To transport the atoms σ_+ polarized light resonant to the $|2, 2\rangle$ to $|3', 2\rangle$ transition is irradiated on the atoms. Since the σ_+-light can only drive transition with $\Delta m_F = +1$ and the atoms can only spontaneous decay by $\Delta m_F = 0, \pm 1$ they finially accumulate in the $|2, 2\rangle$ state. A separate fiber is used to deliver the light for optical pumping.

Additionally repumper light is needed to prevent that atoms are lost into the $F = 1$ manifold. In the case of rubidium the repumper is irradiated through the MOT telescopes. For potassium this is not possible since it would not be possible to separately turn off the cooling light. Thus the repumping light is also coupled into the optical pumping fiber. In our experimental setup the optical pumping increases the number of atoms that are be trapped in the magnetic trap by 50%.

4.4. Detection of atomic gases

After conducting an experiment the atomic ensembles are detected by taking absorption images of the atoms. The detection is one of the most crucial parts of the experiment because all experimental results are extracted from the pictures. In most of the cases the images are taken in time-of-flight (TOF) meaning that the atoms are released from the trap and the pictures are taken after a short period of free fall. The maximum TOF is mainly limited by the field of view of the imaging optics and the walls of the vacuum chamber. In the case of our setup the maximum time-of-flight is limited to approx. 30 ms which is fully sufficient for our requirements. For some type of experiments a long time of free expansion might be helpful. Especially interferometric experiments profit from a long time-of-flight.

The setup for taking the absorption images is sketched in Figure 4.9. The atoms can be imaged on a *Pixelfly 270XD* camera from *PCO* in the direction along the weak axis of the QUIC trap (subsection 4.5.2) providing a $1:1$ magnification using a $f = 140\,\mathrm{mm}$ lens. The camera and the atoms have a distance of $4f$ and the lens is placed exactly in the center. The visible area of this axis is constrained by the inner diameter of the Ioffe coil holder which is 5.6 mm. This limits the maximum TOF to approx. 15 ms in this direction. In the other direction a $3:1$ magnification is achieved by using a telescope constructed out of a $f = 100\,\mathrm{mm}$ and a $f = 300\,\mathrm{mm}$ lens. The first lens is also used for the optical dipole trap. On this axis a *SenSys 3200ME* camera from *Roper Scientific* is used. Figure 4.10a and 4.10b show example pictures takes with this camera. To be able to take images of hotter, bigger clouds a $1:2$ demagnification telescope can be inserted in front of the camera consisting of a $f = 100\,\mathrm{mm}$ and $f = -50\,\mathrm{mm}$ which results reduces the magnification to 1.5. The concave lens with a negative focal length allows to build a very compact telescope.

Since the atoms are trapped 22 cm above the optical table very long posts would be necessary to mount the mirrors and lenses for imaging and the optical dipole trap. To minimize this noise due to vibrations an intermediate breadboard is

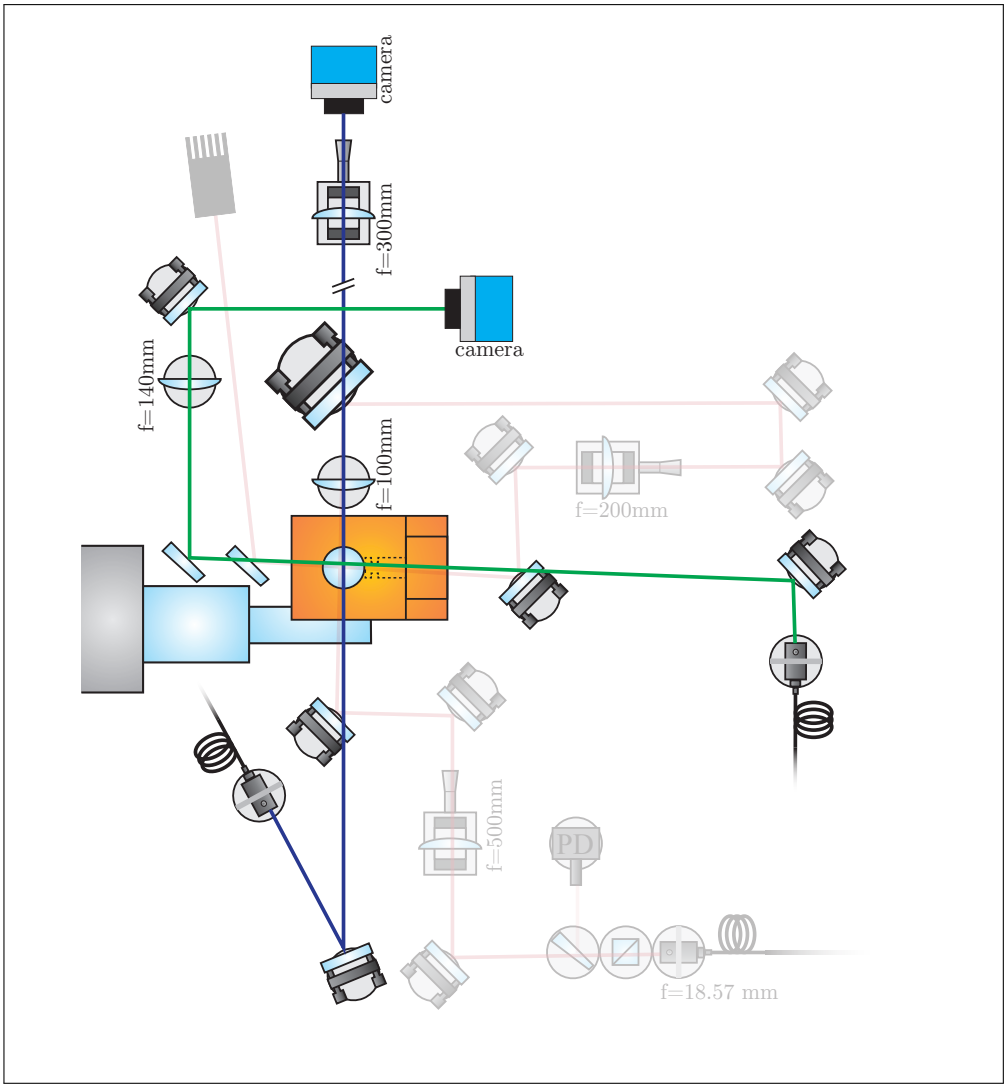

Figure 4.9.: A sketch of the imaging setup which allows to image the atoms from two different directions, depicted with a green and blue beam. The blue axis provides a 1 : 3 magnification. The green axis is a simple one-lens setup with 1 : 1 magnification. The setup used for the optical dipole trap is sketched fainted. Dichroic mirrors are used in both axes to separate imaging light from of the light at 1064 nm used for the optical dipole trap which is depicted faintly in this sketch.

used. It is mounted on top of the optical table and is made out of 5 cm thick solid aluminum. By using this breadboard the effective beam height it is only 7.5 cm. This setup has proven to be very stable and reliable such that the optical dipole trap stays aligned for months.

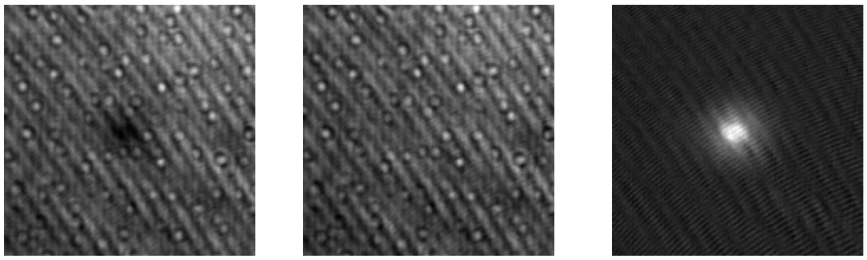

(a) Absorption image (b) Imaging beam (c) Processed picture

Figure 4.10.: The three images above show that a less noisy 2D optical density profile (c) can be derived from a very noisy absorption image (a) by using an additional background image (b). The interference fringes that are still visible on (c) are caused vibrations faster than 1 Hz since the background image has been taken 1 s after the first image.

All parameters of the atomic clouds are calculated based of the measured 2D atom density distribution $n(x, y)$ which is a projection of the real 3D density distribution onto the imaging plane and often called column density. It attenuates the incident beam according to

$$I(x, y) = I_0(x, y)\mathrm{e}^{-n(x,y)\sigma} \tag{4.4}$$

where σ is the effective scattering cross-section and I_0 the intensity of the beam. The effective cross section is given [16] by

$$\sigma = \frac{\sigma_0}{1 + 2I(x, y)/I_{\mathrm{sat}} + 4\Delta^2/\Gamma^2} \tag{4.5}$$

where $\Delta = \nu - \nu_0$ is the detuning of the imaging light from the transition that has a linewidth of $\Gamma(\approx 6\,\mathrm{MHz}$ for potassium and rubidium). Furthermore σ_0 is the resonant cross section and I_{sat} the saturation intensity that both depend on the polarization of the light. The total number of atoms N can then be calculated by summing over all pixels

$$N = A \sum_x \sum_y n(x, y) \tag{4.6}$$

where A is the area covered by one pixel in the imaging place and depends on the pixel size of the camera and the magnification of the optical setup. This factor is determined as shown in Figure 4.11 by taking a series of images of cold cloud at different time-of-flights. The position of the atoms is then related to the theoretical position $s(t) = (g/2)t^2 + s_0$ with $g = 9.81\,\mathrm{m/s^2}$ being the gravitational acceleration.

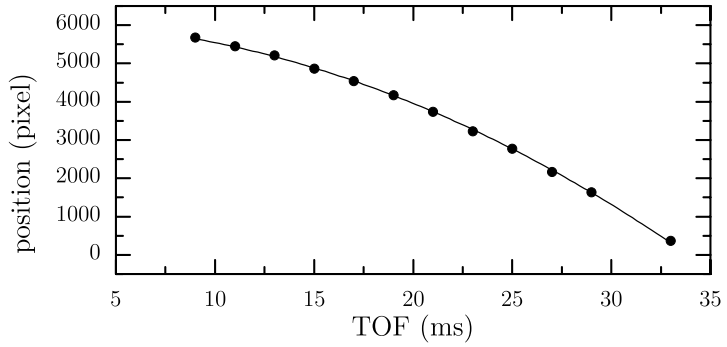

Figure 4.11.: Calibration of the demagnification telescope. A cloud of cold atom is released from the trap and the position is measured in dependence of the time. By relating it to the gravitational acceleration the a pixel-size of 8.44 µm/px is derived.

From (4.4) the term $n(x,y)\sigma$ can be identified as the absorbance (in the following by convention called optical density $D(x, y)$) which attenuates the intensity of the incident beam I_B according to

$$I_\mathrm{A}(x,y) = I_\mathrm{B}(x,y)\mathrm{e}^{-D(x,y)}. \tag{4.7}$$

Experimentally the optical density can be calculated by taking two successive images. Directly after obtaining the absorption image I_A of the atoms an image I_B of the beam is taken such that

$$D(x, y) = \ln I_\mathrm{B}(x, y) - \ln I_\mathrm{A}(x, y) \tag{4.8}$$

in dependence of the two intensities I_A and I_B. As can be seen from Figure 4.10 most off the noise visible on the first two images is removed in the final step of calculating the optical density. The images were exposed for a period of 40 µS and taken 1 s apart.

Theoretically it would be possible to just take one image and reconstruct the imaging beam at the position of the atoms from a Gaussian fit to the intensity

profile. Unfortunately as it can be seen in Figure 4.10a such an absorption image is full of interference fringes and other imperfections. Therefore it is not practical to assume a perfect Gaussian beam and deduce the incident intensity I from that assumption. By using a second picture (Figure 4.10a) that is taken shortly after the absorption image most of the noise cancels out. The remaining interference fringes are mostly caused by vibrations of the optical elements in the beam path and interferences/diffraction at them. Thus it is best to keep the time delay between the successive images as short as possible to increase the frequency range in which the noise gets canceled out. It also helps to build the imaging system such that the elements cannot vibrate. As mentioned before, this goal is reached in this setup by mounting the mirrors and lenses on as short posts as possible. The total number of atoms can then be calculated from an image like Figure 4.10c by using $n(x, y) = D(x, y)/\sigma$ and integrating (summing) over the whole imaging plane.

Trap frequencies and temperature

Beside the atom number the temperature of the ensembles is a very important quantity. It can also be derived from the absorption images since the size of the cloud after TOF depends on the temperature of the atoms. The trapping frequencies of potentials created by a magnetic or optical dipole trap can be approximated by a 3D harmonic potential

$$U(\mathbf{r}) = \frac{1}{2} m \sum_{i \in \{x,y,z\}} \omega_i^2 r_i^2 \tag{4.9}$$

depending on the mass m of the atoms and the trap frequencies ω_i of the potential. The density distribution $n(\mathbf{r})$ of thermal atoms in such a potential is described by a Gaussian distribution

$$n(\mathbf{r}) = \frac{N}{(2\pi)^{3/2}\sigma_x\sigma_y\sigma_z} \mathrm{e}^{-\left(\frac{x^2}{2\sigma_x^2}+\frac{y^2}{2\sigma_y^2}+\frac{z^2}{2\sigma_z^2}\right)}. \tag{4.10}$$

In time of flight the width σ_i of the cloud of atoms evolves like

$$\sigma_i(t) = \sqrt{\sigma_i(0) + t^2 \frac{k_\mathrm{B} T}{m}} \tag{4.11}$$

depending on their thermal energy $k_\mathrm{B}T$. Since this is mass-dependent cold ensembles of potassium atoms grow much faster than cold rubidium clouds at the same temperature. This makes it more difficult to detect the potassium atoms since the detected atoms more dilute and therefore the signal-to-noise ratio is smaller.

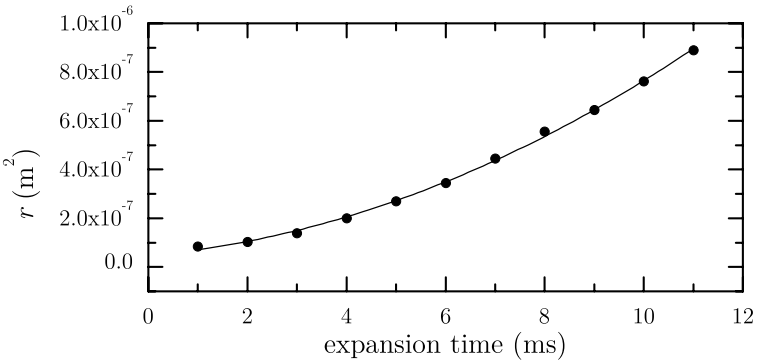

Figure 4.12.: Measurement of the temperature of a cloud of ^{87}Rb atoms after the optical molasses. The quadratic fit to the squared size gives an temperature estimate of 27 µK.

The temperature of the cloud can therefore be measured by taking a series of images with different time of flight as shown in Figure 4.12. By making a quadratic fit $f(t) = at^2 + b$ to $\sigma_i^2(t)$ the temperature can then be derived from the coefficient a as $T = am/(2k_\mathrm{B})$.

The initial width of the cloud is given by

$$\sigma_i(0) = \sqrt{\frac{k_\mathrm{B}T}{\omega_i m}} \tag{4.12}$$

and depends on the trap frequencies. It is therefore additionally important to know the trap frequencies ω_i of the potential. They can be measured by determining the center of mass oscillations $r_i(t) \propto \sin(\omega_i t + \dots) + r_i(0)$ after holding the atoms for a defined amount of time t in the trap. Such an oscillation as shown in Figure 4.13 can be excited beforehand by suitable means. One possibility is to turn the trap of for a short time to offset the atoms from the trap center.

4.5. Magnetic transport and trapping

Since the magneto optical trap is loaded from the background pressure, which prohibits further experiments in that area of the vacuum system, the atoms have to be transported out of this area directly after enough atoms were accumulated in the MOT. The transport is performed in a quadrupolar magnetic trap which is mounted on a translation stage (*404XR* from *Parker*). Thus the atoms are transported within 1.2 s over a distance of 60 cm to the volume of improved vacuum

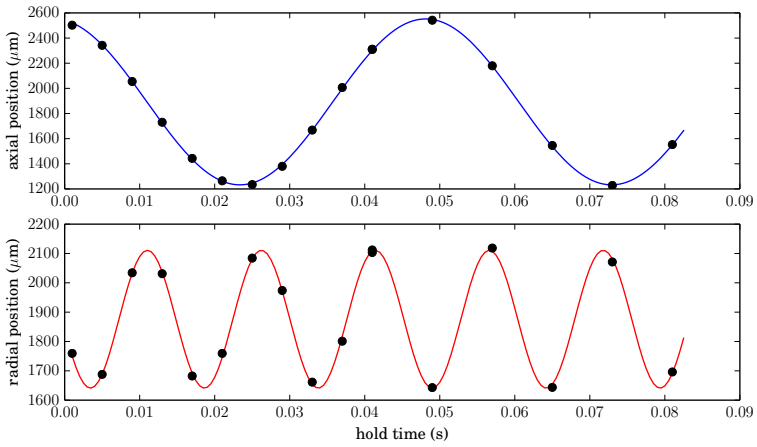

Figure 4.13.: Measurement of the trap frequencies of ^{39}K in a relaxed QUIC trap. Showing 66 Hz in radial and 20 Hz in axial direction.

conditions. The coils providing the magnetic field for the MOT are the same ones used to create the magnetic trap for the transport, Figure 4.14 shows a sketch of these coils and the ones used in the stationary trap described later. They have a distance of 100 mm and consist of 162 windings each. Their outer diameter is 110 mm and their inner diameter is 50 mm. This results in a vertical gradient of $B'/I = 4.35\,\mathrm{G/(cm \cdot A)}$.

After pumping the atoms into the correct state, the current through MOT-coils is ramped up to 200 G/cm and the translation stage moves to the science chamber. The atoms are then loaded into a stationary magnetic trap by increasing the current through its coils within 400 ms until a gradient of 220 G/cm is reached while simultaneously decreasing the current through the transport coils. After the transport 1×10^9 rubidium atoms at a temperature around 300 µK are loaded into the quadrupole trap in the science chamber.

4.5.1. The quadrupole trap

The stationary quadrupole trap in the science chamber consists of two sets of coil pairs. A sketch of it is shown in Figure 4.14. The inner pair (two layers of 20 loops each) has distance of 36.4 mm and is built to provide a very homogeneous field. The other pair has a distance of 46.8 mm and 32 loops. The coils are wound out of 1×2 mm rectangular wire and both have an outer diameter of 100 mm. For use as a magnetic trap both pairs can be connected in anti-Helmholtz configuration

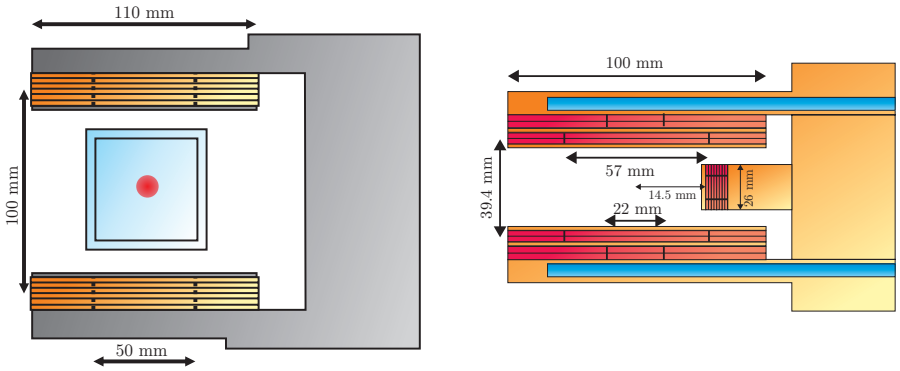

(a) Transport coils (b) QP & QUIC trap

Figure 4.14.: (a) shows the transport coils, the MOT glass cell is drawn in the center to get an impression of the length scales. (b) shows the stationary QUIC trap, the channel for water cooling are depicted in blue. Figures adapted from [59].

(see Figure 4.15) to produce a field of $B'/I = 8.83\,\mathrm{G/(cm \cdot A)}$. For a homogeneous field the inner pair can be used in Helmholtz configuration providing a field of $B/I = 9.47\,\mathrm{G/A}$. To conduct a Stern-Gerlach type experiment only one coil can be switched on to create an inhomogeneous field.

The current is supplied by a custom-built linear regulated current supply from *High Finesse*. It is able to switch the current very fast and has a high current stability of $< 10\,\mathrm{ppm}$ on short time scales. To achieve a good long term stability an additional servo loop is used, which uses a low-noise and low-drift current transducer from *DanFysik* to measure the current.

The coils are mounted on a large copper holder which has channels for a water cooling. The water used for cooling is actively stabilized to $19 \pm 0.1\,^{\circ}\mathrm{C}$ by an industrial chiller from *HIB*. This decouples the cooling of the coils from the main cooling water cycle of the building which is not temperature stabilized very precisely.

After the transport approx. 1×10^9 Rubidium atom are available in the stationary quadrupole trap. The temperature of the ensemble is increased from $20\,\mu\mathrm{K}$ after the optical molasses to $300\,\mu\mathrm{K}$ after transport due to the compression of the trap. The heating rate of cold atoms of about $35\,\mu\mathrm{K}$ is $0.6\,\mu\mathrm{K/s}$ which is sufficient to be able to efficiently evaporate the rubidium atoms until they are loaded into the QUIC trap at a temperature of $160\,\mu\mathrm{K}$.

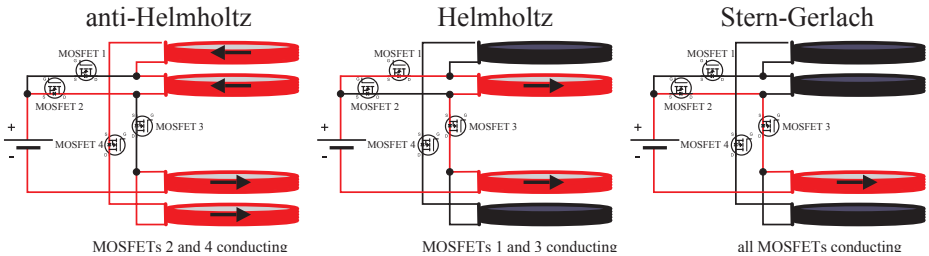

Figure 4.15.: The circuit for switching between quadrupole, homogeneous and inhomogeneous magnetic fields. Adapted from [59].

4.5.2. The QUIC trap

While the a quadrupole trap is a very reliable and simple trap it cannot solely used to produce a BEC. Due to the inherent zero crossing in the center of the trap the atoms undergo so called Majorana spin-flips when crossing the trap center [69]. That happens at low fields when the rate of change in the magnetic field vector is higher than the Lamor frequency $\mu B/\hbar$ of the atom. It becomes significant at low temperatures when the atomic density at the trap center is high. This loss channel can be avoided by constructing a magnetic field that has a non-zero field minimum. In addition the sympathetic cooling of potassium in a quadrupole is very difficult due to the degeneracy of the atomic levels at the trap center (see section 5.6 for explanation).

Thus the trapping geometry had to be changed. Different coil configurations such as the TOP trap or various Ioffe-Pritchard style traps (Cloverleaf, QUIC) are known and well tested. Since the experiment already included with a quadrupole trap the addition of a single coil was the most feasible approach. Thus a QUIC (quadrupole Ioffe-coil) [70] trap configuration was chosen. A QUIC trap is constructed by adding a single additional (Ioffe) coil in between the two coils of the quadrupole trap likes it can be seen on Figure 4.14b and Figure 4.17. The spherical quadrupole trap is converted into the Ioffe configuration by increasing the current I_{Ioffe} through the Ioffe coil. With increasing current the trap minimum is moved towards the Ioffe coil and eventually converted into a non-zero harmonic minimum. The simulation shows that behavior in Figure 4.16. The simulation was pursued by dividing the coil the windings into simple wire loops and then superimpose the fields of all wire loops. The field of each loop was obtained using the analytic solution of the Biot-Savart-law for a simple loop. This approach is quite flexible since it easily allows to construct arbitrary coil configuration (not restricted to a QUIC setup).

The design constraints for the construction of the QUIC trap were:

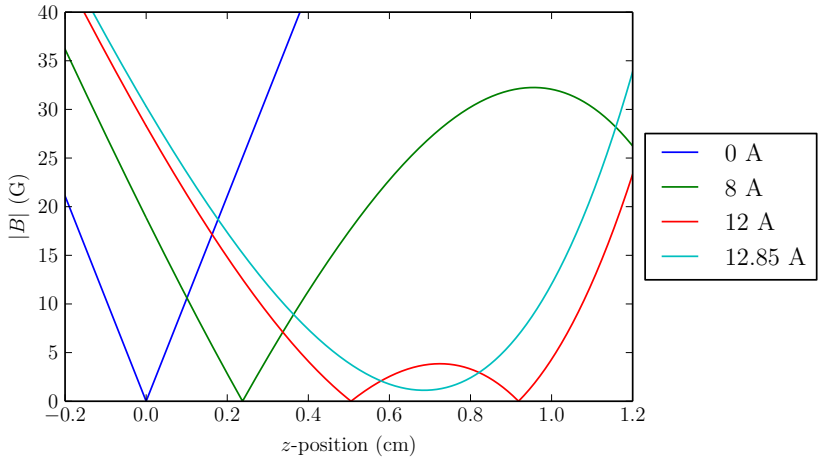

Figure 4.16.: Simulation of the magnetic field along the z-axis (through the Ioffe coil) of the QUIC trap described in subsection 4.5.2. Calculated for different currents through the Ioffe coil.

- A maximum outer diameter of 26 mm, corresponding to the distance between the existing quadrupole coils.
- Make the hole in the middle as big as possible to maximize the optical access.
- Trap frequencies sufficiently high ($\approx 2\pi \cdot 200\,\mathrm{Hz}$ in strong axis).
- Creates the trapping potential with a current I_{Ioffe} that is lower than the current I_{QP} through the QP coils. This constraint is chosen to have a safety margin in case of errors in the simulation and construction of the trap.
- Heat dissipation $\lesssim 10\,\mathrm{W}$ to avoid instabilities caused by overheating.

In order to maximize the heat transport away from the coil it was decided to replace the complete middle part of the existing quadrupole coil holder with a new assembly made of a single piece of copper. A CAD drawing of the final component is shown in Figure 4.17. As can be seen from it the Ioffe holder itself is a massive rod sticking out of the block that is replacing the middle part of the QP holder. The hole in the middle of the rod has a diameter 5.6 mm for the first 25.5 mm and is then expanding to 15 mm diameter. The hole is kept small at the beginning to maximize the heat capacity of the holder at the position of the coil while it is increased later to improve the optical access.

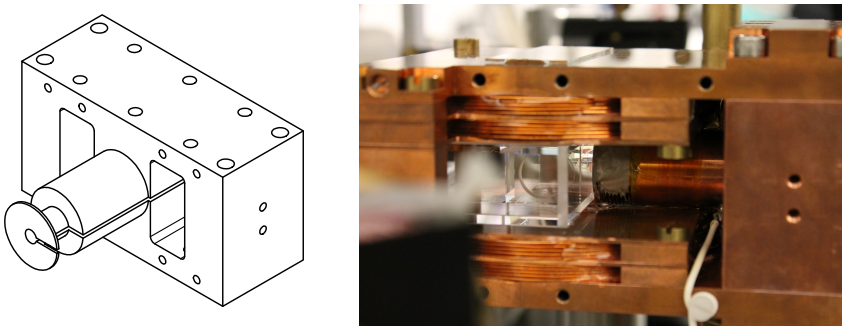

Figure 4.17.: Sketch and photo of the finished QUIC trap. As it can be seen from the sketch. The holder is sliced to prevent eddy currents. On the photo the Ioffe coil is located directly right to the glass cell.

Due to the use of a class cell it was possible to position the Ioffe coil only 15.5 mm away from the center of the quadrupole trap. Thus a fairly weak Ioffe coil is sufficient. A 11×7 mm coil with 60 windings was found to be optimal. It produces a suitable trapping potential at a current $I_{\mathrm{Ioffe}} \approx 0.5 \cdot I_{\mathrm{QP}}$ while shifting the trap center by ≈ 6.5 mm towards the Ioffe coil. To minimize the heat dissipation a wire with a square shape was used which provides a better filling ratio than conventional round wires. The heat dissipation was estimated to be ~ 10 W. Figure 4.17 shows a photo of the finished trap.

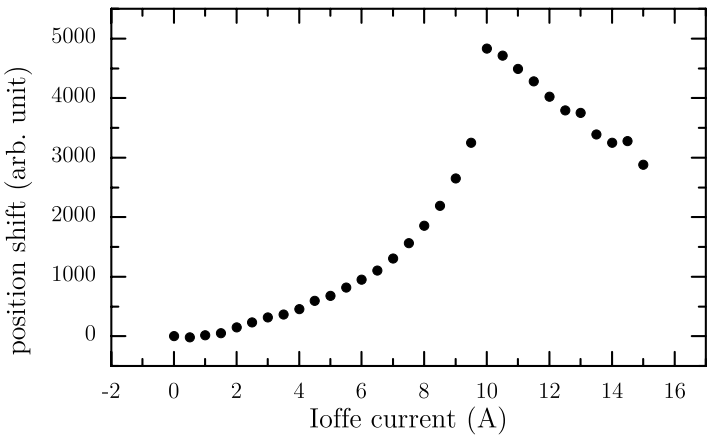

Figure 4.18.: Measured position shift of the trap center as expected. The camera was not calibrated at this point so the value of the shift cannot be compared to Figure 4.16.

The Ioffe coil is connected in series to the quadrupole coils as shown in Figure 4.19. The current through the Ioffe coil is controlled by bypassing the Ioffe coil. In the bypass a high-power MOSFET is used to change the resistance of the bypass. The MOSFET is regulated by a servo loop which uses an *IT 200-S ULTRASTAB* current transducer from *LEM* to measure the current through the Ioffe coil. Since the MOSFET has a finite on-resistance of 7 mΩ an additional MOSFET is used in series with the Ioffe coil to be able to shut it completely off when a homogeneous field is required.

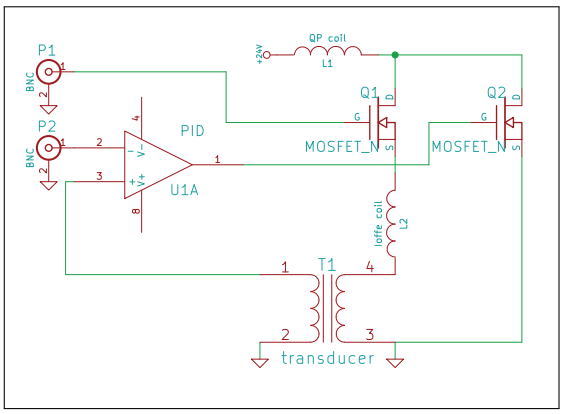

Figure 4.19.: Schematic of how the Ioffe coil is connected to the QP coils.

Figure 4.18 shows how the center of the trap shifts towards the Ioffe coil with increasing current. If the current is increased further above the point where the harmonic trap is formed the position is shifted back again. This is used for loaded the dipole trap in order to be more in the center of the quadrupole trap. The desired offset field of 1 G is reached at $I_{\mathrm{QP}} = 25\,\mathrm{A}$ and $I_{\mathrm{Ioffe}} = 12.85\,\mathrm{A}$. The resulting trapping frequencies shown in Table 4.2. The atoms in the trap have a lifetime of 210 s and a heating rate of 8 nK/s. This allows for a very efficient production of a rubidium Bose-Einstein condensate (see subsection 5.5.1) and very efficient sympathetic cooling of ^{39}K (see subsection 5.5.2). It also indicates that no significant noise is produced by the current regulation.

	f_{radial} (Hz)	f_{axial} (Hz)
^{87}Rb	195	17.4
^{39}K	250	24

Table 4.2.: Trap frequencies of our QUIC trap at a current of 25 A through the quadrupole coils and 12.85 A through the Ioffe coil.

4.6. Trapping in an optical potential

The QUIC trap works reliably to produce rubidium BECs. But in order to create ^{39}K-BECs it is necessary to use a magnetic Feshbach resonance in order to tune the scattering length to a positive value (see chapter 6). Thus the atoms cannot kept trapped in a magnetic potential. One alternative is an optical potential which is utilized here. For this purpose light at a wavelength of 1064 nm is used. This wavelength is far enough away from the atomic transition frequencies such that the absorption of the photons is strongly suppressed. Additionally it is a very common wavelength for which high power light sources and high quality optics are available. In the following I will describe the setup of the laser system needed to generate the light for the optical dipole trap and how the beams are shaped to obtain the desired beam waists.

4.6.1. Laser setup

The laser system consists of two stages. Initially a very stable seed laser generates light with a small bandwidth. This light is then amplified by a fiber amplifier to get the power needed to trap the atoms the setup is sketched in Figure 4.20.

The seed laser is a *Mephisto* laser from *Innolight (now Coherent)* which produces light of a small bandwidth ($\approx$ 1 kHz) with a power of up to 1 W. This laser also allows to tune the wavelength by up to 30 GHz which can be important to avoid association of molecules by the laser which can be a loss channel as suggested by [71] and verified by [72] for a laser operating at 1071 nm. The seed laser is placed on a separate optical breadboard and protected by an optical isolator from back-reflections from the amplifier. The light is then split up and coupled into optical fibers to provide seeding light for multiple amplifiers in different laboratories.

The amplifier is fiber amplifier from *Nufern* (*PSFA-1064-50mW-50W-0*). It provides up to 50 W optical power while maintaining the properties of the seeded

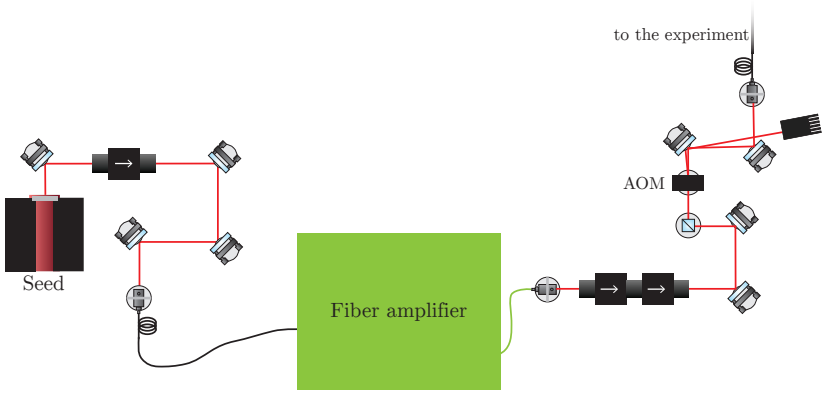

Figure 4.20.: Setup for the generation of the light for the optical dipole trap. The intensity after the fiber is stabilized by controlling the AOM.

light concerning linewidth and frequency stability. For this high power no reliable fiber coupled optical isolator was available such that a free space tandem isolator is used. It provides roughly 50 dB of isolation against back-reflection with a transmission efficiency of 85%.

The light for the dipole trap is sent through an AOM which is used for a fast control of the light power and coupled into a high power photonic crystal fiber (*LMA-PM-15*) from *NKT Photonics*. A small part of the transmitted light is split off the beam on the other end of the fiber and measured with a fast photo diode. This signal is evaluated by a servo loop and fed back to the AOM in order to stabilize the power that is transmitted through the fiber. The set point is controlled by an analog channel from the computer and used to precisely control the light power during the evaporative cooling of the atoms.

The light that illuminates the photo diode for the intensity stabilization is carefully adjusted by a neutral density filter such that the whole dynamic range of the photo diode is used. This is necessary because the power has to be adjusted by two orders of magnitude during the evaporation in the optical dipole trap. The optical power available after the fiber is limited to $16 - 20\,\mathrm{W}$ due to technical reasons. At higher powers the back reflections from the fiber tip cause the fiber amplifier to shut off for safety reasons. This could be prevented by using another isolator after the amplifier but is not necessary at the moment since the sympathetic cooling in the QUIC trap is so efficient that 7 W are enough to hold the atoms.

4.6.2. Crossed dipole trap

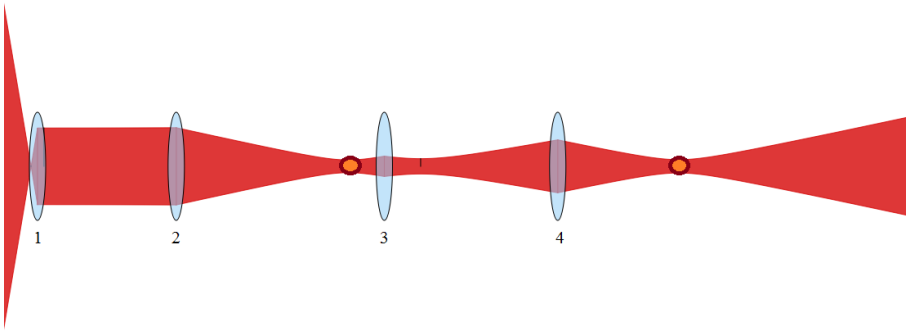

Element	**Fiber output**	L_1	L_2	L_3	L_4
Position (mm)	0	18.57	418.57	1018.57	1518.57
Focal length (mm)	–	18.57	500	100	200
Waist (µm)	6.25	1006	168	201	176
Waist Position (cm)	0	37.14	915	1123	1868

Figure 4.21.: Schematic of the beam profile of the crossed dipole trap (top) and calculated data for the beam waists for the given lenses and positions (bottom). The position where the two beams are supposed to cross is marked with orange circles.

The stabilized light is used to form a crossed optical dipole trap (ODT). In contrast to a single beam trap, a crossed dipole trap provides a strong confinement of the atoms in all directions. The waist were chosen such that a sympathetic cooling of potassium with rubidium is practical, a detailed reasoning for the choise of the waists is found in section 6.1.

Figure 4.22 shows a sketch of the setup the light coming out of the high power fiber in the bottom right corner of the sketch. It is collimated to a waist of 1 mm using a 18.57 mm lens (see Figure 4.21). A polarization beam splitter is used to filter out polarization impurities. The polarization axis of the light is parallel to the table. A small fraction of the beam is split off to measure the power after is then focused down to 168 µm at the position of the atoms using a 500 mm lens. The beam is then recycled and used for the other axis to maximize the trap depth. The $f = 100$ mm lens used for imaging is re-used for the optical dipole trap. Hence it first passes the 100 mm lens also used for imaging before it is then refocused through the tube in the Ioffe coil to 176 µm using a 200 mm lens. Due to optical imperfections the final waist is with approx. 189 µm a bit bigger than anticipated,

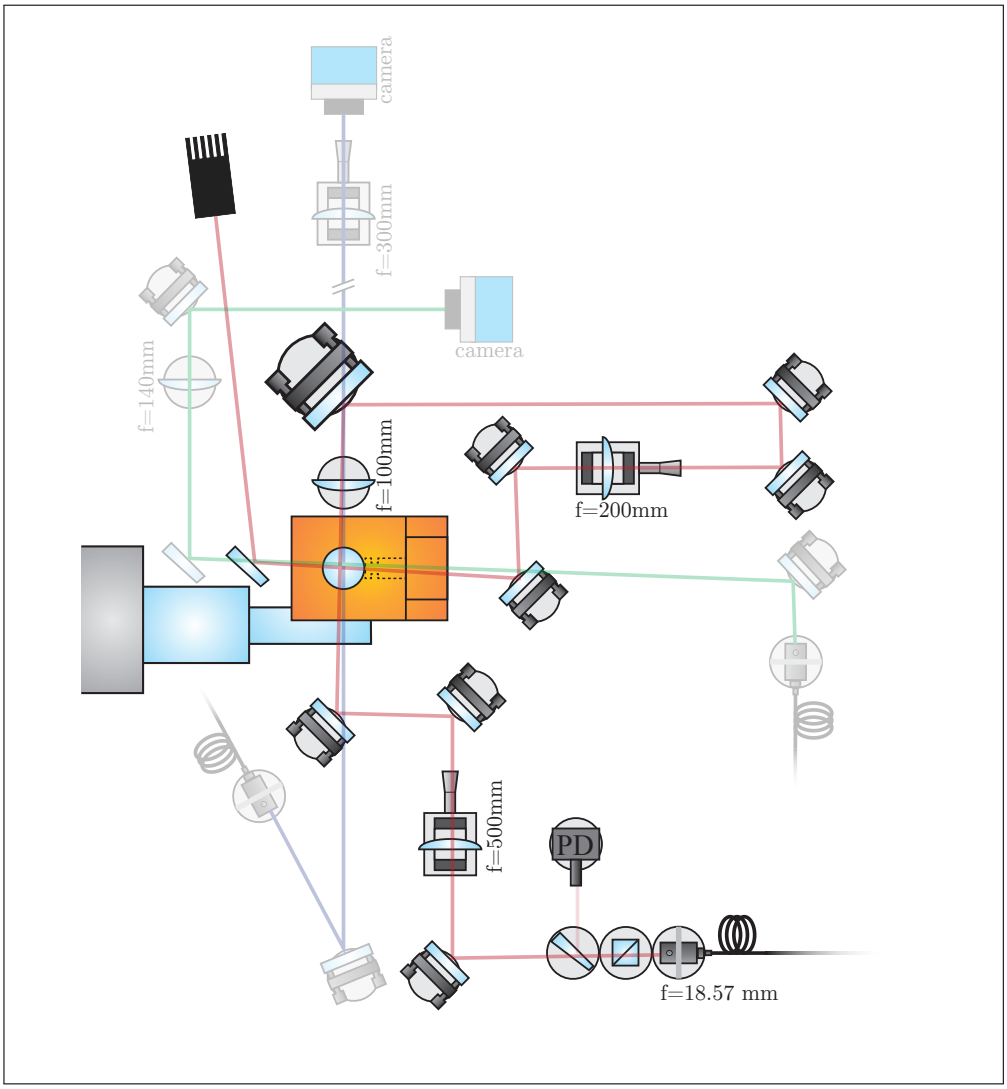

Figure 4.22.: Schematic of the crossed dipole trap. A polarization beam splitter cube after the fiber filters light that is polarized perpendicular to the table. A glass plate splits of a sample of the beam which is used by the photo diode (PD) to quantify the power of the beam.

this value was derived from trap frequency measurements. Since the polarization of the beams is parallel to the table it is tilted by 90° with respect to each other which prevents interferences between the two beams. Since the glass cell has no anti-reflective coating a small part of the beam is reflected by the wall of the chamber and due to the small distance between the wall the second beam interferes with itself. This forms a weak optical lattice as can be seen from the images in Figure 6.6. This lattice could be avoided by tilting the beam slightly as it was also done for the first beam. The maximum tilting angle for the second beam is limited by the tube of the Ioffe coil and not sufficient. Since the lattice is relatively weak it is not disturbing the experiments at the moment. Table 4.3 shows the trap frequencies of the crossed ODT at a power of 16 W and a waist of 189 µm for potassium and rubidium.

	f_{radial} (Hz)	f_{vertical} (Hz)	trap depth (µK)
^{87}Rb	108	152	43
^{39}K	152	214	38

Table 4.3.: Trap frequencies of the crossed dipole trap at a power of 16 W and waist of 189 µm.

4.7. Generation of RF and microwave radiation

Within the experiment radio frequency and microwave radiation is required for the following purposes:

- Microwave radiation at 6.8 GHz
  - for the evaporation of rubidium atoms on the $|2,2\rangle$ to $|1,1\rangle$ transition.
  - for the removal of unwanted atoms in the $|2,1\rangle$ state as shown in Figure 4.23.
- RF radiation at 470 MHz for the transfer of ^{39}K from the $|2,2\rangle$ state to the $|1,1\rangle$ state.
- RF radiation between 40-120 MHz to transfer the atoms between the states in the m_F manifolds.

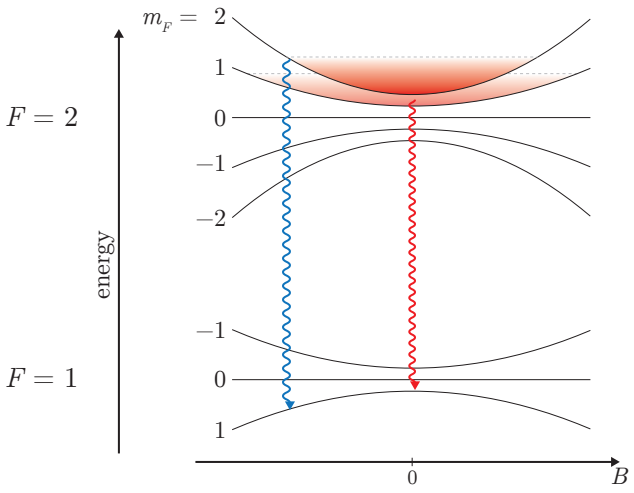

Figure 4.23.: Evaporation with microwave radiation in a QUIC trap. The hottest atoms are transferred from the trapped $|2, 2\rangle$ state to the untrapped $|1, 1\rangle$ state (blue arrow). This produces unwanted atoms in the $|2, 1\rangle$ state which are removed using a second field (red arrow).

Figure 4.24 shows a block diagram of the setup that is used to generate the various frequencies. It was assembled from off-the-shelf components which are connected through SMA connections. The generation of µW radiation is necessary since potassium (^{39}K and ^{41}K) and rubidium have the same magnetic field dependent splitting of their m_F states of 700 kHz/Gauss. Thus evaporation on the transition the $|2, m_F\rangle$ state to the $|2, m_F - 1\rangle$ state cannot be used. Instead the atoms are transferred from $|2, 2\rangle$ to $|1, 1\rangle$. At a frequency of 6.8 GHz this transition is located in the microwave regime of the electromagnetic spectrum.

4.7.1. Microwave generation chain

The generation of frequencies around 6.8 GHz is not trivial since precisely controllable oscillators in this region are simply not available or very expensive. A common approach to generate a microwave signal is to use a frequency multiplier. Since a multiplier also generates other harmonics its signal has to be filtered by a relatively narrow band pass filter.

In this apparatus a multiplier is used to generate a static microwave signal that can be used to prepare a specific hyperfine state with π-pulses or to purify the atomic sample by removing atoms in an undesired state (as shown in Figure 4.23).

To generate this signal a high power synthesizer, producing a signal at 976.4 MHz, is connected to a step recovery diode (SRD). The SRD is a very fast diode which abruptly stop the currently flow when switching from forward to reverse direction which creates higher harmonics. The 7th harmonic is selected with a band pass filter. The resulting signal is then further amplified to a power of 1 mW.

A different approach is used to generate the signal for the evaporative cooling of the atoms. The signal at 6.8 GHz is created by a high frequency voltage controlled oscillator (VCO) which is locked to the master oscillator with a phase locked loop (PLL). This method requires no further filtering of the signal and is therefore suitable to create frequency sweeps over a wide frequency range. In order to generate smooth ramps a *VFG 150* DDS from *Toptica* is used as a master oscillator. It only provides signals up to 150 MHz such that a multiplication factor of 50 was chosen for the PLL.

The two microwave signals are combined with a power combiner. A variable attenuator after the combiner allows to set the desired power level. An amplifier amplifies the combined signal to a power of 1 W. A helical antenna is used to impose the microwave field onto the atoms. In order to protect the amplifier from back-reflections caused by improper impedance matching of the antenna a circulator is installed after the amplifier. The reflected power is thus dumped in a 50 Ω terminator. The frequency generation chain works reliable and allows to evaporate Rubidium very efficient in the QP and QUIC trap.

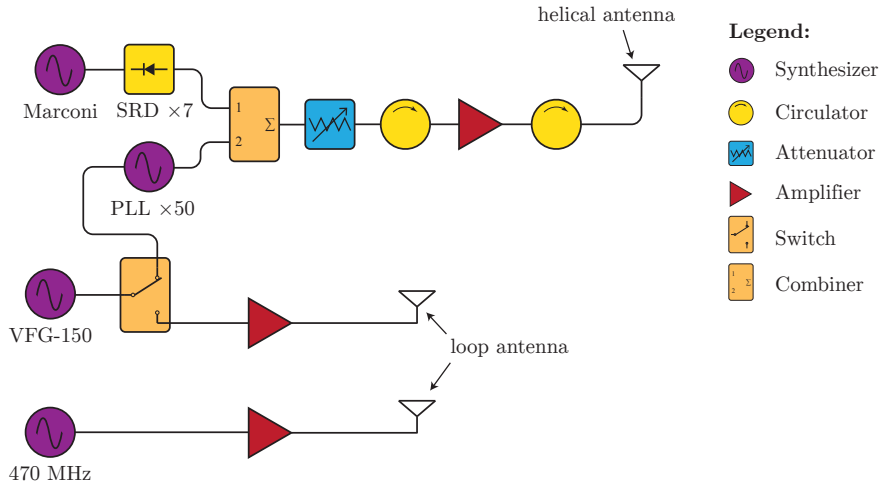

Figure 4.24.: Block diagram of the RF and µW radiation generation chain. Filters have been deliberately left out to improve the clarity.

4.7.2. Radio frequency radiation for state preparation

To utilize a specific magnetic Feshbach resonance the atoms have to be prepared in the correct internal state. To do that either RF/µW π-pulses (see subsection 2.5.1) or rapid adiabatic passages (see subsection 2.5.2) can be used. For transferring atoms from one m_F state to another in the same F manifold rapid adiabatic passages have proven to work most reliable in our experiment. For the passages in ^{39}K RF radiation with a frequency between 50 and 100 MHz is required which can then be used for both potassium and rubidium. In order to transfer the atoms from the $F = 2$ to $F = 1$ state a signal with a frequency of 460 MHz for potassium and 6.8 GHz for rubidium is required. For the latter the setup used for the evaporation can be re-used.

The signal for the rapid adiabatic passages is generated again by the same *VFG 150* as used for the evaporation. Instead of being multiplied by 50 it is directly amplified and irradiated onto the atoms using a simple loop antenna. Since the antenna is not very well matched (the circumference is only about 10 cm compared to a wavelength fo 31 m). A high power of up to 10 W is required. The mismatch was especially critical for the signal at 470 MHz which is generated by another synthesizer. It was necessary to match the impedance of the antenna for this particular wavelength by inserting a capacitor of 20 pF across the loop. Since such a impedance matching has a narrow bandwidth the antenna could not be used for a signal of 100 MHz any more. Therefore two different antennas are used for the two frequencies. This dual-antenna setup allows to transfer potassium from the $|2, 2\rangle$ state into the $|1, 1\rangle$ state and prepare potassium and rubidium in an arbitrary m_F-substate with nearly 100% efficiency.

4.8. Experimental control

Due to the complexity of quantum gas experiments an automatized control of the apparatus is necessary. The computer control of the experiment is based on commercial PCI cards from *National Instruments*. Two digital-to-analog converter (DAC) cards provide 16 analog channels with 8 channels each. They supply a voltage in a range of ±10 V with a resolution of 12 (*NI PCI-6713*) and 16 bits (*NI PCI-6733*). In addition 32 digital channels (5 V TTL level) are provided by one *DIO-32HS* card.

The cards are programmed using *National Instruments'* graphical LabView programming environment. LabView has the advantage that it is easy to learn

while allowing to program time critical application like an experimental control system. In our setup the timing is controlled by a hardware clock which keeps all cards synchronized by triggering the cards. After obtaining a trigger the cards read the next value by direct memory access (DMA) out of the computer's main memory. The timing is therefore independent from the operating system and other software running on the computer. Nevertheless it is advisable to keep the workload of the computer low while running a sequence, since a buffer under-run can occur when the computer is running a task that occupies the PCI bus to much.

The user interface is also programmed in LabView as a so-called virtual instrument (VI) as shown in Figure A.2. The core is a matrix where the column represent the time steps and the rows the different output channels. A calibration curve is assigned to every analog channel that relates the control voltage supplied by the DAC-cards to the physical quantity (e.g., current through the Ioffe coil) that should be changed. This makes the programmed sequence more independent from the underlying hardware as long as the calibration is adjusted to the hardware changes.

The first iteration was programmed in University of Hamburg. It was then used in another Potassium-Rubidium experiment in Hanover where it was adapted to be used on this apparatus. In Aarhus several features were added to the program. To document the work done make the experiments traceable, the parameters of every experimental run are saved. Thus every data point taken can later be related to a specific sequence. In practice any previous run it can now also be loaded into the VI again after this feature was added in Aarhus. The saved metadata can also be used for a fully automatic data evaluation by extracting the relevant parameters out of run description.

The ability of the control program to run successive sequences while varying the parameters was greatly expanded. Beforehand the program could only changed parameters by specifying the column and row index of the value that should be changed that was error prone and impractical if a value should be change in many columns. Here the ability of using variables was added. After being defined by name and value the variable can be assigned to a field by selecting the name from a drop-down list. Since these menus only support numerical values in LabView a hash value of the name is calculated that is then assigned to the drop-down list. In principle a hash map (dictionary) had to be implement which is not available as a primitive LabView data type. The sequences can then be programmed using a 2D matrix where the columns are translated into nested for-loops. The rows of each column are changed in parallel. Since it is not possible to program loops with

an unknown nesting level (recursion is difficult in LabView) the loops had to be implemented in a single loop. To do that the Cartesian product of the column indices and the number of cycles per loop was calculated. This results in a list of doublets containing the index of the current loop and the advancement in this loop. This can be used to easily calculate the value for each loops from withing a single unnested loop. As a later addition is will be easily possible to randomize the loop order to spread out systematic drifts of the experiment in time and thus improving the quality of the recorded data.

5 Sympathetic cooling of potassium in magnetic traps

Given the advances in lasers and the existing knowledge, it is nowadays straightforward to create a ^{87}Rb BEC. The condensation of potassium on the other hand, requires more effort. This is mainly due to the unfavorable level structure of potassium for laser cooling. The hyperfine splitting of the excited $5^2P_{3/2}$ state is on the order of the linewidth, and therefore the probability that both the repumping and cooling light fields drive unwanted transitions is not negligible. This reduces the efficiency of the MOT and optical molasses such that both smaller and hotter ensembles are produced. One way to combat this issue is to implement an additional MOT configuration, namely a 2D MOT [73] which adds complexity to the system. With the help of this technique it is indeed possible to directly evaporate potassium [74] until condensation.

In the experimental setup presented here we chose a much simpler approach, using only a single 3D MOT. Although the efficiency of the optical molasses was significantly improved (as described in section 5.2), the number of potassium atoms is still not sufficient for direct evaporation. It was therefore inevitable to implement sympathetic cooling of potassium in the magnetic trap which is described in section 5.5. Sympathetic cooling describes the process of using one ensemble as a heat reservoir in order to cool the other one. It was first demonstrated in 1997 [75] and proved to be suitable to cool until Bose-Einstein condensation sets in. Within our work, the cooling in a QUIC trap was so efficient that it was possible to create a ^{41}K condensate starting with only 1×10^6 ^{41}K atoms, after transport to the science chamber as described in subsection 5.5.3.

While this technique allows the production of ^{41}K condensates in a QUIC trap it is not possible to create ^{39}K condensates in a standard magnetic trap. Due to the

attractive interaction of ^{39}K at low magnetic fields the ensemble collapses at low temperatures. Hence, the atoms have to be transferred into an optical dipole trap to be able to tune the scattering length to positive values which is described in chapter 6.

Originally it was planned to utilize a hybrid trap [60, 76] to sympathetically cool ^{39}K but as it turned out, this is not possible due to additional heating mechanisms in the quadrupole trap, as described in section 5.6.

5.1. Dual species MOT

The setup used for the dual species MOT is described in section 4.2. During the MOT phase a current of 2.5 A through the MOT coils is used to generate a gradient of 11 G/cm in the vertical direction. For the rubidium MOT 180 mW of cooling light plus 20 mW of repumping light power is available, resulting in the rubidium MOT shown in Figure 5.1. For potassium a total power of 270 mW is used and the intensity is split more evenly between cooling and repumping light. The power ratios are 2 : 1 for ^{39}K and 1 : 1 for ^{41}K. Table 5.1 shows the frequency detunings of the potassium and rubidium light used for the magneto optical traps.

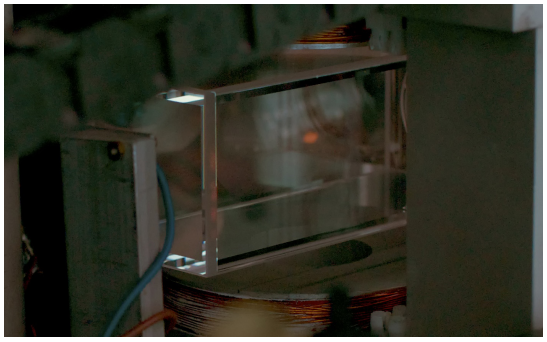

Figure 5.1.: ^{87}Rb MOT with $\sim 1 \times 10^9$ atoms.

The main difficulty of a dual species MOT is that the two MOTs cannot be considered as independent ensembles any more. It has been reported [77] that potassium and rubidium undergo light assisted collision, which lead to losses. The main loss channels are:

Radiative escape: One or two of the atoms are excited and go into an attractive molecular potential. During the de-excitation the pair may emit a photon red to the atomic transition where the excess energy is released in form of kinetic

	$\Delta_{\text{cooling}}/\Gamma$	$\Delta_{\text{repumping}}/\Gamma$
^{87}Rb	-4	0
^{39}K	$-3\frac{2}{3}$	$-5\frac{1}{3}$
^{41}K	-5	-2.5

Table 5.1.: Detuning of cooling and repumping light frequencies in units of the respective linewidth Γ during the MOT phase. The detuning is given relative to the $|2,2\rangle$ to $|3',3\rangle$ transition for the cooling light and relative to the transition $|1,1\rangle$ to $|2',2\rangle$ for the repumping light

energy $\Delta E = h(\nu_1 - \nu_2)$, allowing an atom to escape. Example reaction of the $K - Rb*$ channel:

$$K(4S_{1/2}) + Rb(5S_{1/2}) + h\nu_1 \rightarrow K(4S_{1/2}) + Rb(5P_{3/2}) \\ \rightarrow K(4S_{1/2}) + Rb(5S_{1/2}) + h\nu_2 + \Delta E$$

Hyperfine changing collisions: Only the hyperfine state which is changed and the energy difference between the involved states is converted into kinetic energy. Example reaction channel:

$$K(4S_{1/2}, F = 2) + Rb(5S_{1/2}, F = 3) \\ \rightarrow K(4S_{1/2}, F = 1) + Rb(5S_{1/2}, F = 2) + \Delta E$$

Due to the mass ratio $m_{\text{K}}/m_{\text{Rb}} \simeq 0.45$, the excess energy of the collisions affects potassium much more than rubidium. One possibility to work around this problem is to use a dark spot MOT [78]. In this technique, the light beams are modified such that they have a dark spot in the center. This creates an area without light in the center of the MOT where the coldest atoms can accumulate without undergoing collisions that may lead to an escape from the trap.

Since a dark spot MOT is not trivial to construct we use a very simple alternative. The MOT is simply misaligned slightly. Although the same optical elements are used to direct the light for both atomic species towards the MOT, which results in a subtle displacement of the two MOTs with respect to each other. Slight differences in the beam power ratios and polarizations in combination with the different mass of the two species this leads to this displacement. Figure 5.2 shows the effect of the misalignment. Despite the fact that the initial available number of atoms is higher for well aligned MOTs, the decay of the number of ^{39}K atoms is much faster.

The misalignment results in a gain of a factor two after loading rubidium for 6-8 s which is required for a ^{87}Rb BEC.

For the production of ^{39}K BECs a loading time of 18 s (combined potassium and rubidium-MOT) was chosen. This MOT loading time result in approx. 2×10^9 rubidium atoms and 4×10^7 ^{39}K atoms.

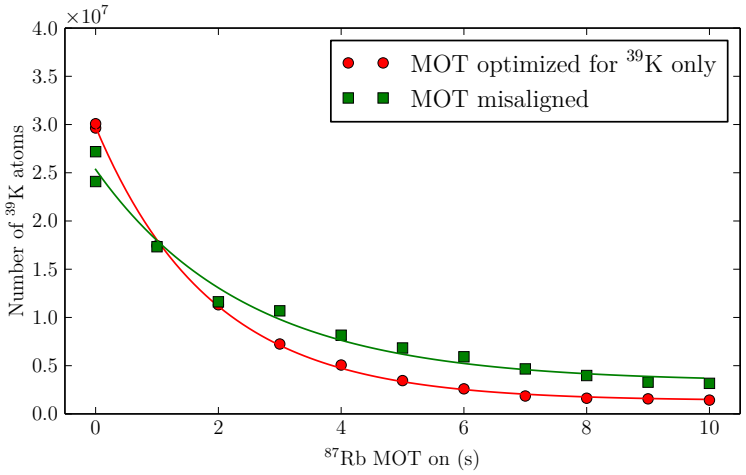

Figure 5.2.: Influence of the MOT alignment on the number of potassium atoms in the science chamber. ^{39}K was loaded for 15 s then the ^{87}Rb MOT was turned on additionally. The ^{39}K atom number decays much fast when the MOTs are well aligned (circles).

5.2. Optical molasses for potassium and rubidium

After loading the MOT an optical molasses is applied to cool atoms below the Doppler limit. A typical optical molasses works efficiently, if the hyperfine splitting Δ is much bigger than the natural linewidth Γ, which is the case for rubidium. In our experiments a 700 µs long molasses at a detuning of 1Γ is sufficient to cool the atoms to 35 µK.

For potassium the situation is unfortunately considerably different. Since the hyperfine splitting $\Delta \simeq 2\Gamma$ a standard molasses is not efficient. However, sub-Dopper cooling is possible when using a more advanced scheme [79, 80], and the small hyperfine splitting is even advantageous in this case. The neighboring states

cause a natural depumping of the atoms into a dark state forth the cooling light. By using the already existing repumping light, the population of the bright state can be controlled precisely. This allows to optimize the fraction of atoms affected by the cooling light while keeping the photon re-absorption low. In the usual case of $\Gamma >> \Delta$ an additional depumping laser would be necessary.

In the case of ^{39}K this is realized by using the following scheme. At the beginning of the molasses phase the repumping laser light is abruptly adjusted to 5% of the initial power and tuned on resonance. The cooling laser is detuned to -0.5Γ. Within 8.5 ms the intensity is linearly ramped down to 50% and the detuning to -2.3Γ as shown in Figure 5.3a. With this scheme a temperature of 117 µK is reached, which is a huge improvement compared to a temperature of 2 mK before the molasses phase.

The procedure is similar for ^{41}K. The repumping laser light is tuned on resonance and adjusted to 5% of the cooling laser power. The cooling laser is tuned to -0.5Γ. It's frequency is then linearly changed withing 7 ms until a detuning of -0.83Γ is reached. This is sketched out in Figure 5.3b. Table 5.2 lists the temperatures and numbers of atoms that were obtained after the optical molasses.

	N	T(µK)
^{87}Rb	2×10^9	20(3)
^{39}K	4×10^7	117(6)
^{41}K	2×10^6	?

Table 5.2.: Starting conditions after the optical molasses. The corresponding numbers for ^{41}K cannot be measured reliably due to a low signal to noise ratio.

5.3. Magnetic transport

After the molasses the atoms are optically pumped into the state $|2,2\rangle$ in order to increase the transfer efficiency. Therefore a homogeneous magnetic field of 15 G is applied to the atoms and σ^+-polarized light, resonant to the transition $F = 2$ to $F' = 2$, is irradiated onto the atoms for 1 ms. Additionally the repumper is used to pump the atoms back into $F = 2$ (see section 4.3). In the case of rubidium the repumper is irradiated onto the atoms using the MOT beams. This is not possible

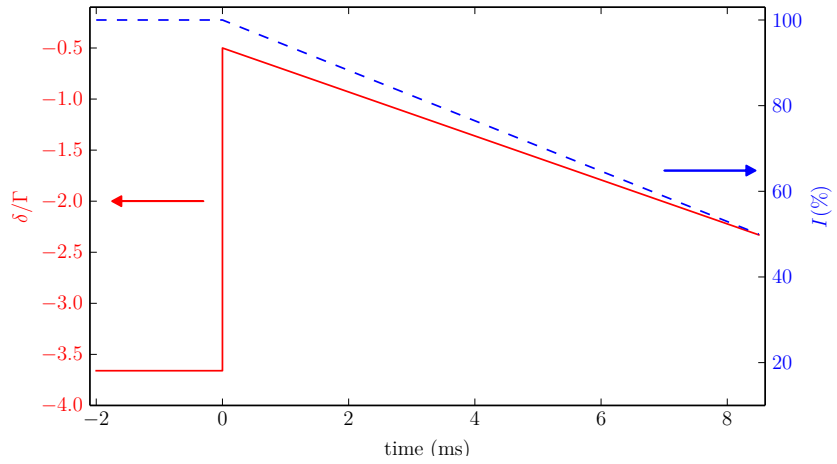

(a) Molasses for ^{39}K

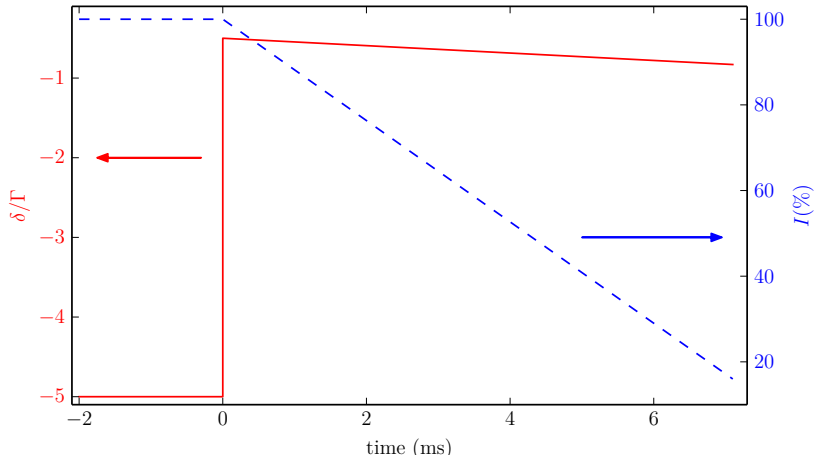

(b) Molasses for ^{41}K

Figure 5.3.: Molasses sequence for ^{39}K and ^{41}K. The detuning δ is given in units of the linewidth Γ and the intensity I is given with respect to the initial intensity during the MOT phase. The repumping light is kept resonant and at 5% of the cooling light intensity.

for potassium since the cooling light cannot be switched off in this case. Thus both lights are irradiated onto the atoms using the optical pumping fiber.

After the optical pumping the current through the transport coils is abruptly increased to 15 A to catch the atoms and then ramped up to 45 A resulting in a gradient of 196 G/cm. The atoms are then moved within 1.2 s to the science chamber and loaded into the stationary QP trap within 800 ms. This is done by decreasing the gradient of the transport coils while increasing the gradient of the stationary coils to 350 G/cm

The initial number of atoms N and temperature T of the atoms after the transport to the science chamber is shown in Table 5.3. Due to an adiabatic compression by an increase of a linear gradient by a factor of a a temperature increase of $a^{2/3}$ [81] is expected. Since the first part of the compression is non-adiabatic a temperature increase of $a =\sim 15$ is expected from previous data [24]. Thus the temperatures obtained in the molasses (see Table 5.2) are consistent with the temperature after the transport.

	N	T(µK)
^{87}Rb	1×10^{9}	315
^{39}K	2×10^{7}	700
^{41}K	1×10^{6}	?

Table 5.3.: Starting conditions for the various isotopes in the QP trap after relaxing it to a gradient of 200 G/cm. The initial temperature of ^{41}K cannot be measured reliably due to a low signal to noise ratio.

5.4. Sympathetic cooling of potassium in a QP trap

Initially a short phase of evaporation in the quadrupole trap is conducted. This is inevitable since the QUIC trap has only a finite trapping volume and therefore the loading of too hot clouds would lead to losses [16]. The potential of our QUIC trap has a saddle point at a radial distance of ~ 7 mm. The rubidium atoms have a thermal radius of 1.3 mm while the potassium atoms have a radius of 3.9 mm. Additionally the confinement of a QP trap is stronger than in a QUIC trap.

The rubidium atoms are therefore first evaporatively cooled for 4 s in the QP

trap using a microwave field which transfers them from the trapped $|2,2\rangle$ state to the untrapped $|1,1\rangle$ state. During the evaporation the gradient is reduced to 220 G/cm. The evaporation in the QP trap is stopped at a frequency offset of 30 MHz. This produces potassium atoms at a temperature of 180 µK. The current through the Ioffe coil is increased to 12.85 A within 1.4 s. This transfers the atoms into the QUIC trap.

5.5. Sympathetic cooling of potassium in a QUIC trap

As described in section 5.6 it is not possible to sympathetically cool potassium with rubidium to quantum degeneracy in a quadrupole trap. As the evaporation of rubidium on the hyperfine transition at 6.8 GHz inevitably produces hot rubidium atoms in the $|2,1\rangle$ state this leads to heating of the potassium. Therefore the sympathetic cooling at low temperatures is continued in a QUIC trap. The construction of a QUIC trap is described in subsection 4.5.2.

To keep the power dissipation low, such that long hold times on the order of one minute and cycle times of 0.5 Hz are possible, a current of 25 A through the quadrupole coils was chosen. Since the trap frequencies that are achievable in a QUIC trap are inverse proportional to the offset field B_0, a compromise between high trap frequencies and a sufficiently high offset field, to avoid spin flips had to be found. In practice an offset field of 1 G was chosen. This field is reached at a current of 12.85 A through the Ioffe coil. When the Ioffe coil is turned on to load the atoms into the harmonic potential, the trap minimum is shifted by 6.5 mm towards the Ioffe coil. This axis is also the main symmetry axis of the trap but provides the smallest confinement as can be seen in Table 4.2 and Table 5.4. A lifetime of over 200 s and a low heating rate of 8 nK/s where achieved in the QUIC trap, measured with rubidium at an initial temperature of 4 µK.

	f_{radial} (Hz)	f_{axial} (Hz)
^{87}Rb	20	13.4
^{39}K	65.9	20.2

Table 5.4.: Trap frequencies of the QUIC trap at a current of 15 A through the quadrupole coils and 9 A through the Ioffe coil. This relaxed trap is used for loading into the optical dipole trap.

5.5.1. Production of ^{87}Rb condensates in the QUIC trap

Rubidium-87 is a commonly used isotope to create Bose-Einstein condensates, since it features a convenient background scattering length of $a = 95.44a_0$ [82]. This allows efficient evaporative cooling both in magnetic and optical traps.

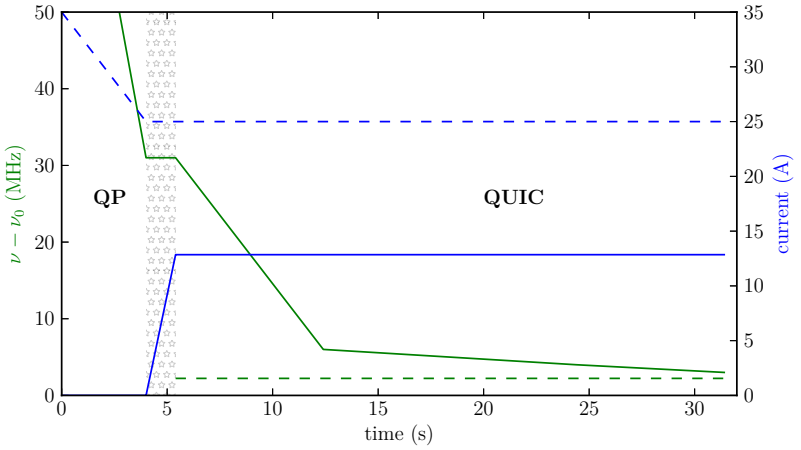

Figure 5.4.: Experimental sequence that leads to the formation of a ^{87}Rb BEC in a QUIC trap. The evaporation is done purely in magnetic potentials. The blue curves show the current through the QP coils (dashed) and Ioffe coil (solid). The green curves show the frequency offset of the used microwave fields from the $F = 2$ to $F = 1$ resonance at 6.834 Ghz. The gray area depicts a change in the trapping geometry.

After the atoms have been trapped in a MOT and transferred to the stationary QP trap, as described in the previous section. Subsequently they are evaporatively cooled as it is shown in Figure 5.4. After the transfer the atoms are evaporated in the quadrupole trap and transferred into the QUIC trap as described in section 5.4. At the same time as the atoms are transferred into the QUIC trap, an additional microwave field is turned on, which has an offset frequency of 1.54 MHz (dashed green line in Figure 5.4). This field removes atoms in the $|2, 1\rangle$ state which would lead to heating (see section 5.6). The frequency is then reduced over the next 26 s. An exponential frequency sweep is approximated by a linear sweep as shown in Figure 5.4.

The efficiency of the evaporation is quantified by the factor

$$\gamma = -\frac{\mathrm{d}\ln D}{\mathrm{d}\ln N} \tag{5.1}$$

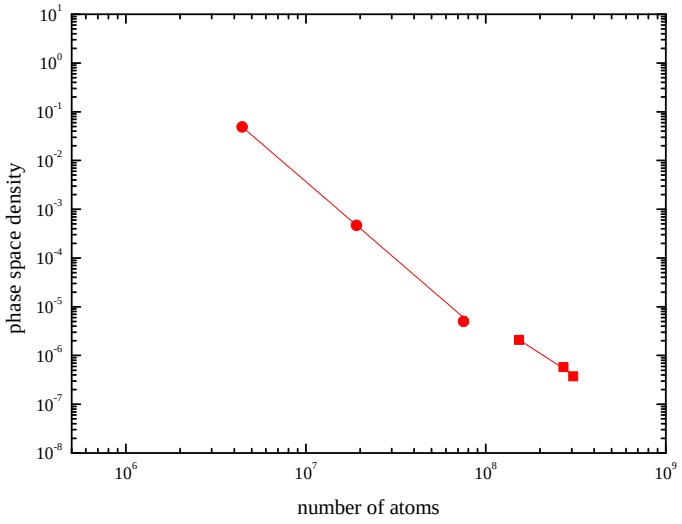

Figure 5.5.: Evaporation sequence of ^{87}Rb in the quadrupole (squares) and the QUIC trap (squares).

where D is the phase space density and N the total number of atoms. The lengths of all evaporation steps were optimized by maximizing γ. Typically $\gamma > 2$ is desirable and for the evaporation in the QP trap $\gamma = 2.4$ was realized as shown in Figure 5.5. The subsequent evaporation in the QUIC trap is more efficient due to the longer lifetimes, since Majorana losses and collisions with atoms in $|2,1\rangle$ are avoided. It has an efficiency of $\gamma = 3.2$. At the end 6×10^5 atoms in the BEC were be reached. Figure 5.6 shows the transition of a thermal cloud to a BEC. The change in aspect ratio after a time of free expansion is characteristic for a BEC compared to a thermal cloud that just expands homogeneously.

5.5.2. Sympathetic cooling of ^{39}K

An efficient sympathetic cooling of ^{39}K requires a fast rethermalisation of the potassium atoms with the rubidium atoms that serve as a coolant. As I discuss in the following, it is therefore even more beneficial to have high trapping frequencies than in the case of rubidium. First of all the inter species scattering length $a_{87-39} \simeq 28a_0$ [83] between potassium and rubidium is by a factor of three smaller than the intra-species scattering length of rubidium. Thus the evaporation ramps have to be considerably longer than for the evaporative cooling of rubidium alone

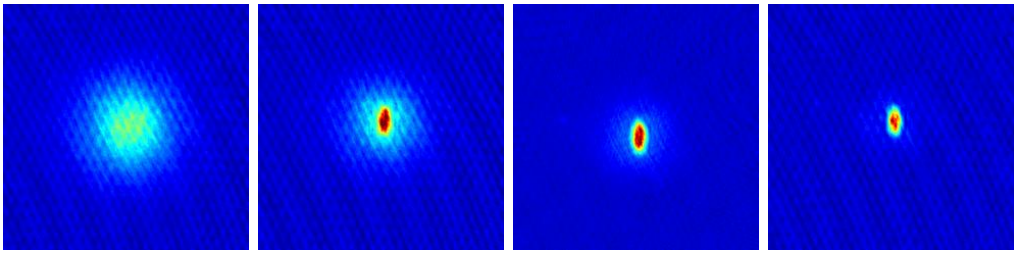

Figure 5.6.: Different steps in the transition from a thermal ^{87}Rb could to a pure BEC. The second and third image show a bi-modal distribution since both thermal and condensed atoms are present. Imaged 22 ms after the release from the QUIC trap.

in order to allow for an efficient rethermalisation. Secondly, the overlap of the two clouds has to be sufficiently high during the evaporation such that a rethermalisation is possible. As discussed in [84] this depends strongly on the confinement by the trap. The thermal radii of the two species scale with $1/\omega_r$, while the gravitational sags scale with g/ω_r^2.

Thus the QUIC trap was constructed to realize as high trap frequencies as possible. That increases the overlap of the clouds as well as it increases the rethermalisation rate. Given the radial trap frequencies in a typical experiment (see Table 4.2) the difference in gravitational sag is only 2.5 µm while the thermal radius of potassium at 100 nK is still 2.9 µm in our QUIC trap. Therefore the trap does not impose a limit on the cooling ability.

The following experimental sequence is used to realize sympathetic cooling in a QUIC trap. Initially the dual-species MOT is loaded as outlined in section 5.1 and the atoms are cooled an trapped as described in section 5.2. The atoms are then transported to the science chamber where the 2×10^7 potassium and 1×10^9 rubidium atoms are initially available in the QP trap. The rubidium is then evaporated using the procedure shown in Figure 5.7. The evaporation is started in the QP trap and has the same duration of 4 s as the evaporation of rubidium only. A longer duration is not beneficial at this point since the QP trap inherently suffers from shorter lifetimes as discussed earlier. But due to the strong confinement in a QP trap it is still beneficial to begin the sympathetic cooling in the QP trap. The potassium-rubidium mixture is then loaded into the QUIC trap withing 1.4 s by increasing the current through the Ioffe coil.

In the QUIC trap the second microwave field is turned on in order to the remove the unwanted atoms in $|2,1\rangle$. Rubidium is then evaporated in three steps within

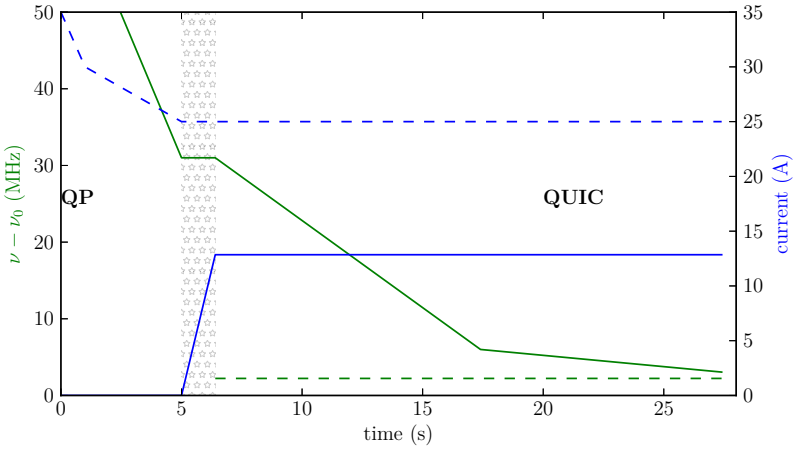

Figure 5.7.: The sequence for sympathetic cooling of ^{39}K with ^{87}Rb in a QUIC trap. The blue curves show the current through the QP coils (dashed) and Ioffe coil (solid). The green curves show the frequency offset of the used microwave fields from the $F = 2$ to $F = 1$ resonance at 6.834 Ghz. The gray area depicts a change in the trapping geometry.

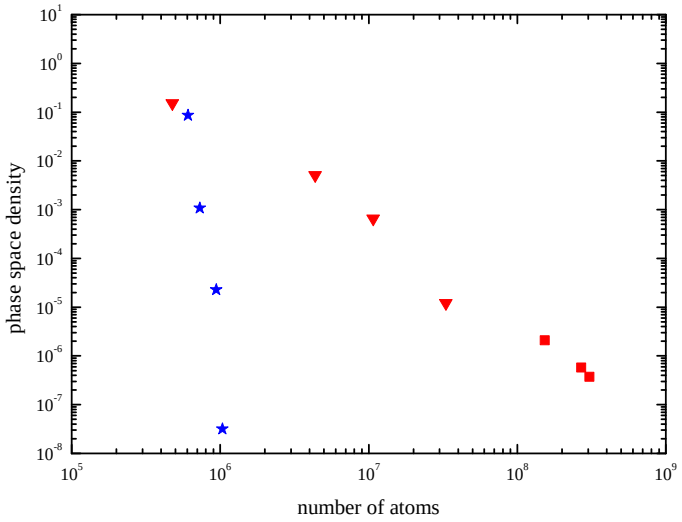

Figure 5.8.: Phase space density as a function of the number of atoms during the sympathetic cooling of potassium (stars) with rubidium (triangles in the QUIC, squares in QP).

20 s. This leaves about the same amount of potassium and rubidium in the trap such that 9×10^5 potassium atoms at a phase space density of 0.1 are left at this point. The efficiency of the rubidium evaporation significantly reduced to $\gamma = 1.5$ at the end since it acts as a coolant for ^{39}K. For the sympathetic cooling $\gamma_{\mathrm{sym}} = 24$ is measured is comparable to values reported before [84]. Ideally γ_{sym} should be close to infinite and it is thus just a measure of additional loss processes that are imposed on the potassium. Since roughly the same γ_{sym} is reported in [84], it can be concluded that it is typical to have such efficiencies for sympathetic cooling of potassium in a QUIC trap.

Due to our strong QUIC trap it was thus possible to cool the potassium so efficiently that only ~ 1.5 orders of magnitude in phase space density have to be obtained until a BEC will start to form. Thus it should be possible to realize a ^{39}K BEC by direct evaporation in an optical dipole trap which is presented in section 6.5.

5.5.3. Condensation of ^{41}K

With a natural abundance of 6.73% ^{41}K is more then ten times abundant than ^{39}K. Additionally the hyperfine splitting of the excited state is only 17 MHz. This makes the starting conditions much more difficult than for ^{39}K but in contrary to ^{39}K the scattering length is positive $a_{41} \sim 60a_0$ [85]. This makes it possible to condensate ^{41}K directly in a QUIC trap without having to use Feshbach resonances. Additionally, the inter-species scattering length is $a_{87-41} \sim 163a_0$ [76] which allows an efficient rethermalisation with ^{87}Rb.

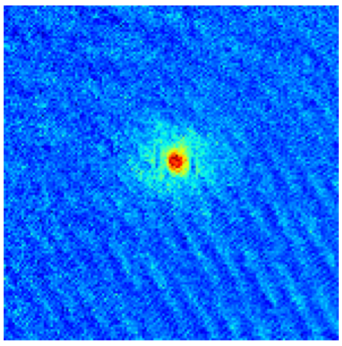

Figure 5.9.: ^{41}K BEC in free expansion after being released from the QUIC trap.

Figure 5.10 shows the sequence used to create a ^{41}K BEC. First a rubidium MOT is loaded for 10 s then the potassium MOT is turned on and a dual species

MOT is loaded for 35 s. Finally 2×10^6 potassium and 1×10^9 rubidium atoms are transferred into the quadrupole trap. The rubidium is then evaporated in the QP trap for 2 s. This time was chosen as short as possible to avoid heating of the potassium due to rubidium atoms produced in the $|2,1\rangle$ state which is especially crucial since the initial number of potassium atoms is so low. Then the atoms are loaded into the QUIC trap within 1.4 s. In the QUIC trap a second microwave field at 6836.223 MHz is used to remove the atoms in the $|2,1\rangle$ at the trap center. The rubidium is then slowly evaporated within 48 s. At the end a ^{41}K condensate with 1×10^4 atoms was obtained, which is shown in Figure 5.9. Unfortunately all rubidium atom was removed in this process but further optimization of the evaporation ramps should make it possible to obtain a dual species ^{87}Rb−^{41}K Bose-Einstein condensates.

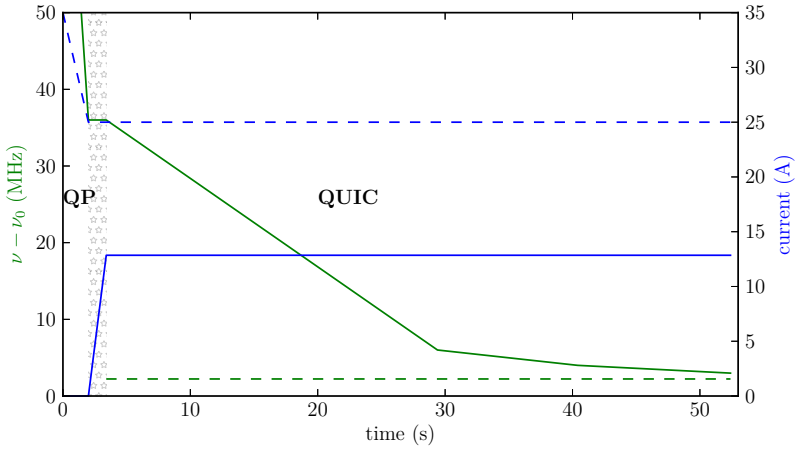

Figure 5.10.: Sequence for the sympathetic cooling of ^{41}K. The blue curves show the current through the QP coils (dashed) and Ioffe coil (solid). The green curves show the frequency offset of the used microwave fields from the $F = 2$ to $F = 1$ resonance at 6.834 Ghz. The gray area depicts a change in the trapping geometry.

5.6. General problems of cooling in a hybrid trap

In the initial experiment, a hybrid trap [36, 60] was used in an attempt to sympathetically cool potassium with rubidium. In a similar strategy to the one outlined in section 5.4, a simple quadrupole trap was used to perform the initial cooling

steps. Since the inter-species scattering length for ^{87}Rb–^{39}K collisions is small long evaporation times are required. That is problematic since the lifetime in a quadrupole trap is inevitably limited by Majorana losses. This problem can be circumvented by loading into the optical trap before the losses become relevant. Unfortunately the evaporation of rubidium on the hyperfine transition also has the drawback of producing hot atoms in the $|2,1\rangle$ state [86, 87].

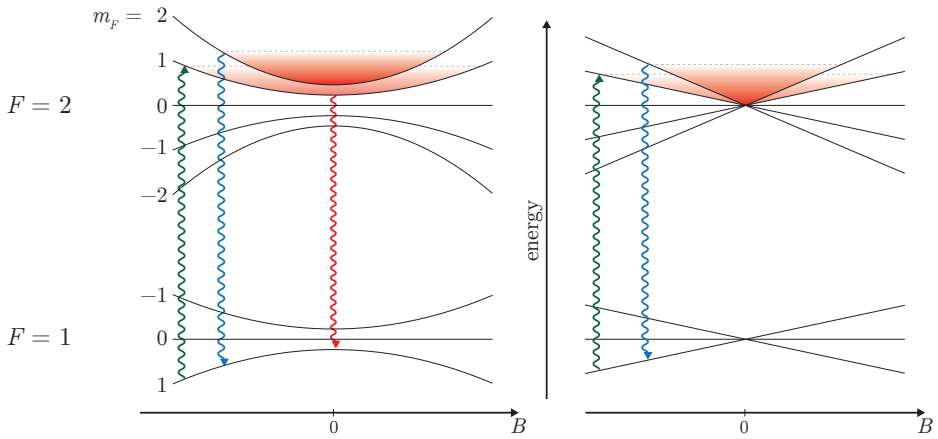

Figure 5.11.: The figure shows the energies of the $|F, m_F\rangle$ states depending on the position in a confining potential. The units are arbitrary. Right: The situation in a quadrupole trap with degenerating energies is shown. Left: situation in a QUIC trap. The arrows depict different transitions that can be driven by a microwave field. The blue and green arrows have the same length.

The process is sketched in Figure 5.11. The left diagram shows the energies of the magnetic substates in a quadrupole trap versus the radial position. The red arrow depicts the microwave field transferring the atoms from the $|2,2\rangle$ to the $|1,1\rangle$ state. The atoms are then in a anti-trapped state and accelerate outwards while gaining kinetic energy. The green arrow shows a second position at which the microwave field is resonant to an allowed transition. There the accelerated atom can be transferred to the trapped $|2,1\rangle$ state. Thus this process can lead to heating instead of cooling. Although only a small fraction is transferred back into the trap this effect is fatal for the sympathetically cooled potassium since typically only $1{\times}10^7$ potassium atoms are available.

Figure 5.12 shows the effect of the heating. Potassium and rubidium were held in the quadrupole trap at a gradient of 133 G/cm. The frequency of the

microwave field, used for the evaporation of rubidium, was kept constant such that the temperature of rubidium stays constant. The potassium was simultaneously heated up. This is caused by the rubidium as shown by a temperature measurement of the potassium without the presence of the rubidium. This process limited the temperature and atom number that were archived to 100 µK and and 4×10^6 atoms from which only 1×10^5 potassium atoms could be transferred into the optical dipole trap. These starting conditions are insufficient to produce a potassium Bose-Einstein condensate and make a dual species condensate even less feasible.

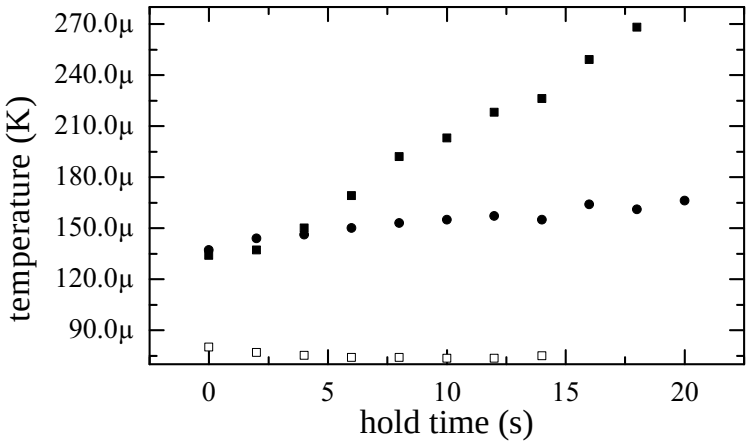

Figure 5.12.: Heating due to rubidium atoms being transferred into the $|2,1\rangle$ state. The heating rate of the potassium atoms (black squares) is increased when it is held in the trap while rubidium (white squares) is constantly evaporated. This is not the case if the rubidium was removed (circles).

It is clear from these results that atoms in the $|2,1\rangle$ have to be removed [88]. Two different methods were experimentally investigated:

- Increasing the loss rate for atom in the $|2,1\rangle$ state by adding an additional microwave field addressing atoms close to the center of the trap.

- Purifying the sample in the magnetic trap by going below gravity compensation for $m_F = 1$.

The first method uses the fact that atoms below a certain temperature are lost due to Majorana spin flips. According to [69] atoms of velocity v are lost as soon they

enter an ellipse of radius

$$r_{\text{hole}} = \sqrt{\frac{v(T)\hbar}{\mu B'}} \tag{5.2}$$

in the center of the QP trap. Here B' is the magnetic field gradient, $\mu = m_F g_F \mu_B$ and $v(T)$ the mean velocity of the atoms at the temperature T. The size of this hole is bigger for atoms in the $|2,2\rangle$ state than for atoms in the $|2,1\rangle$ state. The energy shift of these atoms would also be weaker. We thus used a second µ-wave field whose frequency is close to resonance and should primarily evaporate atoms in the $|2,1\rangle$ state that are within the Majorana hole. By placing this second knife at exactly r_{hole} for a sample at 100 µK this should remove all atoms in $|2,1\rangle$ below a temperature of 1.5 µK. This method was not efficient, due to the fact that the atoms were still relatively hot and only an insignificant fraction of them had a temperature below 1.5 µK.

The second idea of purifying the sample using the gravity was also not successful since the losses were to high such that only 1×10^5 potassium atoms were transferred into the dipole trap at temperature of 10 µK.

6 Ultra-cold gases with tunable interactions

The tunability of the scattering length of ^{39}K provides many experimental prospects but comes at a large price in terms of the required experimental complexity. Potassium is in general much more difficult to trap than rubidium which limits the possible number of atoms than can be realized in a 3D MOT. Additionally it has a negative s-wave scattering length, which makes it practically impossible to create a BEC in a magnetic trap. To tackle the first problem sympathetic cooling with rubidium can be used, which was presented in chapter 5. To circumvent the second problem an optical dipole trap is used to trap the atoms in order to use a magnetic Feshbach resonance to tune the scattering length. The design considerations for an optical dipole trap for sympathetic cooling are discussed in section 6.1. In section 6.2 I report on the creation of a ^{87}Rb BEC in the optical dipole trap which serves as a test for the creation of the ^{39}K BEC. I then present the accessible Feshbach resonances in ^{39}K in section 6.3. Additionally the neighboring inter-species resonances with ^{87}Rb will be discussed. To be able to use the Feshbach resonances, the atoms have to be prepared in a particular internal state and hence the state preparation is described in section 6.4.In section 6.5 I report on the successful condensation of ^{39}K in an optical dipole trap. Concluding this chapter the control of the interactions is presented in section 6.6.

6.1. Confinement in optical dipole traps

To achieve optimal sympathetic cooling, additional constraints arise for the design of an optical dipole trap. The effective potential acting on the atoms is

$$U(\mathbf{r}) = U_{\mathrm{dip}}(\mathbf{r}) - mgr_z, \tag{6.1}$$

where m is the mass of the atom and $g = 9.81\,\mathrm{m/s^2}$ the gravitational acceleration.

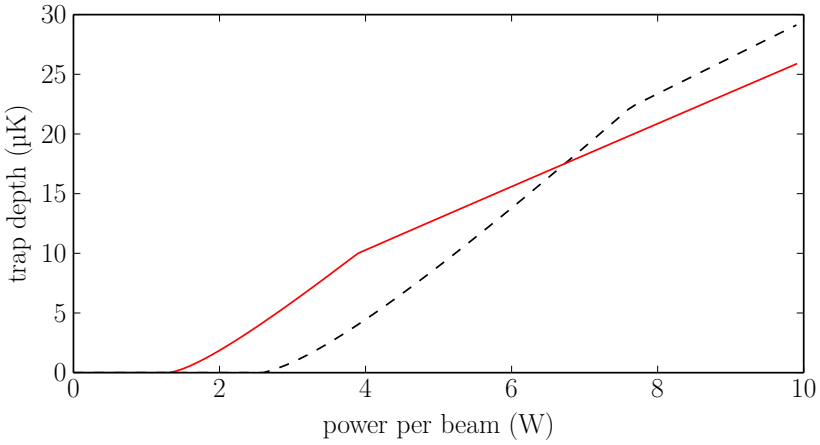

Figure 6.1.: Trap depth of a crossed optical dipole trap versus power per beam for potassium (red line) and rubidium (black dashed line). The beam waists are 180 µm and the angle between the two beams is 90°. Note that at low power the trapping potential is deeper for ^{39}K than for ^{87}Rb. This is due to gravity as explained in the text.

Figure 6.1 shows the effect of gravity on the potential of a crossed ODT. At high powers the dipole trap is deeper for the rubidium atoms than for potassium atoms. This is due to the smaller detuning for rubidium than for potassium. At lower powers gravity affects the potential such that it becomes deeper for potassium since its mass is only half as big. In a crossed optical dipole trap that is oriented in horizontal direction the horizontal confinement is mainly mediated only one of the two beams while the vertical confinement is provided by both beams. This causes the slow abruptly to double at lower powers when the gravity starts to become more important and is visible in for of a kink in Figure 6.1. Thus the two curves cross at some point. From this point on the trapping potential is stronger for potassium and sympathetic cooling with rubidium is possible. As shown in

Figure 6.2, the trap depth at which this crossing occurs increases linearly with the beam waist. On the other hand the power required to reach this point grows more than linear. That technically limits the maximum waist that can be used. Taking all this into consideration a target waist of 180 µm was chosen for designing the optical dipole trap.

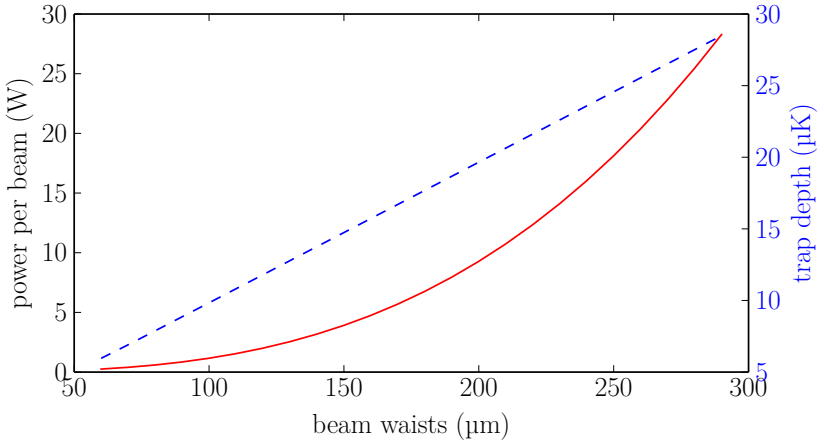

Figure 6.2.: This graph shows the power needed to trap both ^{39}K and ^{87}Rb equally strong (solid, red) and the corresponding trap depth (blue, dashed) versus the diameter of the waists.

To check whether this waist is suited for sympathetic cooling the overlap of the two clouds depending on the power was calculated. Figure 6.3 shows the sum of the thermal radii $r_{\mathrm{K}} + r_{\mathrm{Rb}}$ and the differential gravitational sag of the two clouds in dependence of the power. Thermal equilibrium was assumed such that both clouds have a temperature of $U_{\mathrm{Rb}}/10$. The sag is smaller than the sum of the radii until a temperature of 500 nK and hence an efficient evaporation is feasible above this temperature. Below that point the sag grows considerably but sympathetic cooling should still be possible until it corresponds to twice the radius which is equivalent to a temperature of 100 nK, well below the critical temperature.

6.2. ^{87}Rb BEC in the crossed ODT

In order to test the performance of the crossed dipole trap the last steps of the evaporation of rubidium were performed in the ODT. The initial sequence was the same as described in subsection 5.5.1 with the exception that the final evaporation

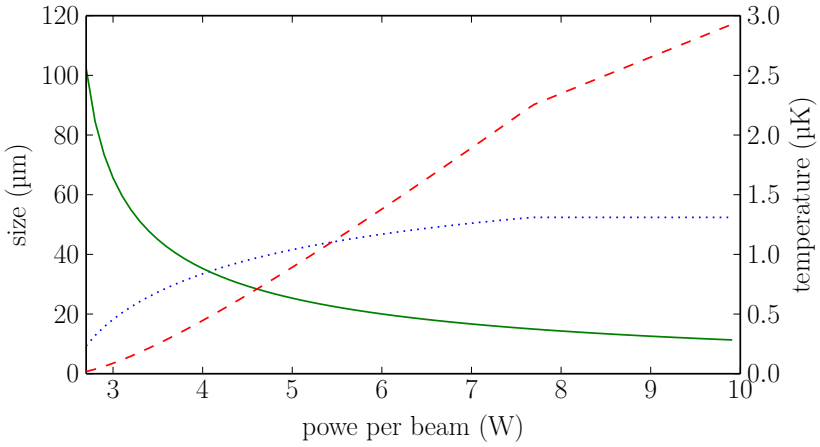

Figure 6.3.: Differential sag of potassium and rubidium (green line) versus the optical power in each beam in a crossed ODT. A waist of 180 µm was used for the calculating. The dotted blue line shows the sum of the thermal radii of potassium and rubidium in that trap. Until a power of about 4 W efficient sympathetic cooling is possible. That corresponds to a temperature of 500 nK as can be seen from the red dashed line which shows the temperature estimate for rubidium.

step in the QUIC trap was removed such that the evaporation in the QUIC trap had a total duration of 19 s. The sequence is sketched in Figure 6.4. The last evaporation step in the QUIC trap was then adjusted until a temperature of 1.8 µK was reached. This is the temperature we expected to reach in the worst case for potassium and rubidium by sympathetic cooling (as reported for a much weaker trap [84]). At this point 4.3×10^6 rubidium atoms are available in the QUIC trap.

The QUIC trap is then relaxed to 13.4 Hz axially and 56 Hz radially. This shifts the atoms towards the center of the trap by 1 mm, which improves the imaging quality at long expansion times since diffraction of the imaging light at internal structures in the glass cell is avoided. The atoms are then loaded into the optical dipole trap by turning the QUIC trap off over a duration of 1 s while the power of the optical dipole trap is increased to 10 W at the same time. This corresponds to a trap depth of $\sim$ 20 µK and trap frequencies of 85 and 118 Hz. During the loading process almost 100% of the atoms are transferred into the dipole trap. This high transfer rate is achieved since the atoms were already cooled down to 1/10 of the trap depth such that no atoms are lost by free evaporation. Moreover the

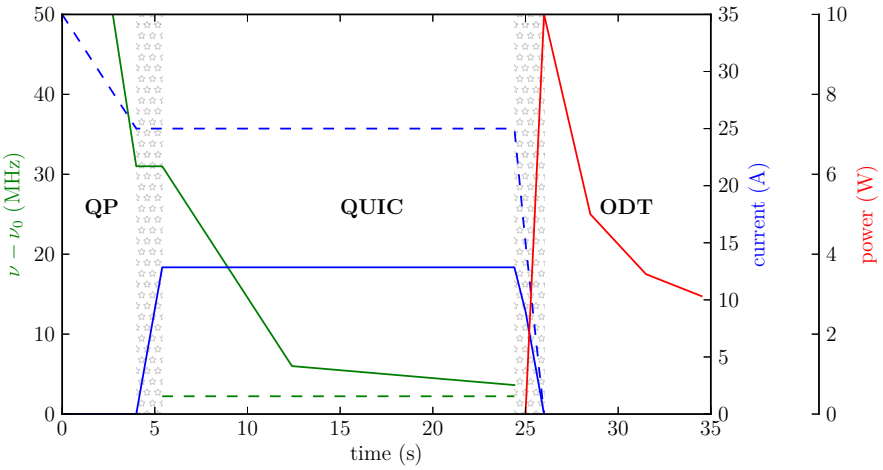

Figure 6.4.: Evaporation sequence of ^{87}Rb first in a quadrupole, then in a QUIC trap and at the end all-optical in a crossed optical dipole trap. The green curves show the frequency-offsets from resonance of the microwave radiation used for evaporative cooling. The blue lines show the currents used for the QP coils (dashed) and the Ioffe coil. The red line shows the power of the optical dipole trap. The structured area marks transitions to another trap geometry.

large waist of approx. 189 µm allows good mode matching with the in-trap size of the atomic cloud in the QUIC trap. The power of the dipole trap is then linearly decreased in three steps over a total duration of 8.2 s down to 2.9 W. The final trap has a frequency of ~ 40 Hz in all axes. At this point condensation was reached with $5{\times}10^4$ atoms in the BEC fraction.

Figure 6.5 shows the efficiency of the complete evaporation of rubidium. A factor $\gamma = 2.79$ was reached in the optical dipole trap which is only slightly worse than in the QUIC trap. This is very promising since it means that not much heating is induced by the optical dipole trap in comparison to the evaporation in the QUIC trap.

The transition of the thermal rubidium cloud to a BEC is shown in Figure 6.6. In the last pictures two additional clouds are visible. These clouds appear due to an imperfect alignment of the optical dipole trap. Some fraction of the beam is reflected and forms an optical lattice. This lattice imposes a momentum of $\hbar k$ onto parts of the BEC which translates into a spatial separation in TOF. The formation of the optical lattice could be circumvented by increasing the angle of the

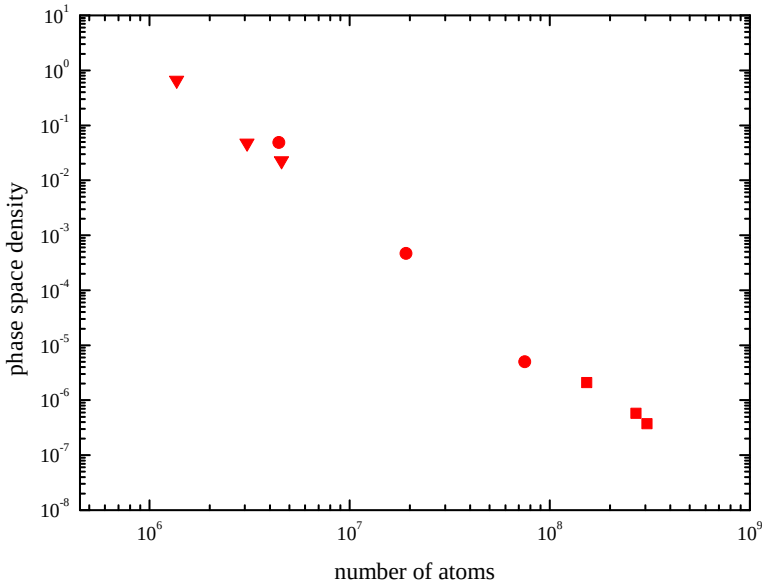

Figure 6.5.: Evaporation sequence of ^{87}Rb in a quadrupole (squares), QUIC (circles) and a crossed optical dipole trap (triangles).

dipole trap beam with respect to the surface of the glass cell. This is unfortunately not easily implemented in the current setup, since the relevant dipole beam is directed through a hole in the Ioffe coil which limits the maximum angle that can be obtained.

6.3. Utilization of magnetic feshbach resonances

Potassium provides a rich structure of accessible feshbach resonances. This can be seen in Table 6.1, which shows measured positions and widths of all known ^{39}K-resonances with a width larger than 0.1 G at fields below 1000 G. To utilize resonances with a smaller width it is necessary to control the magnetic field to a higher degree of precision than it is possible for us at the moment. Our current-supply is able to control the current through the magnetic coils with a precision < 10 ppm which allows control of the magnetic field produced of ± 0.1 G precision at a field of 1000 G. The resonance should therefore have at least a width that is ten times bigger then this.

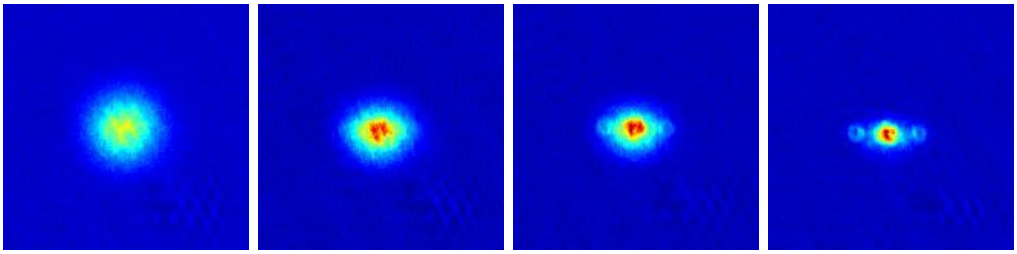

Figure 6.6.: Transition of a thermal rubidium cloud into a pure ^{87}Rb-BEC in a crossed an optical dipole trap. In the last pictures the influence of an residual lattice is visible. The images are taken after release from the ODT.

m_F	B_0(G)	ref.	$-\Delta_{\mathrm{th}}$(G) [89]	$a_{\mathrm{bg}}(a_0)$ [89]
1	25.85(10)	[89]	0.47	−33
	402.6(2)	[90]	52	−29
	752.3(1)	[89]	0.4	−35
0	58.92(3)	[90]	9.6	−18
	65.67(5)	-”-	7.9	−18
-1	33.64(15)	-”-	−55	−19
	162.35(18)	-”-	37	−19
	560.72(20)	-”-	56	−29

Table 6.1.: Measured Feshbash resonance position B_0, theoretical widths Δ_{th} in background scattering lengths a_{bg} in ^{39}K.

Fields over 1000 G are difficult to access due to the coils we use. One problem is that the thermal load applied to the coils will be too high and thus only a short usage of the coils with currents higher than 100 A is possible. A much severe problem is that the field decay of our coils is rather slow. It currently takes 10 ms for the field to drop to the noise level at 100 G and the resonances at 403 G and 561 G (see Table 6.1) have not been accessed on this experimental apparatus for this reason. There are several possibilities to overcome this limitation.

One option would be to construct the coil holder from a non-conducting material such as PTFE (Teflon) to avoid eddy currents. The big drawback of this option is that it makes the cooling of the coils much more difficult, since the heat conductivity of Teflon is very low. This would require a different cooling concept which would not allow for such a compact trap. The second possibility would be to simply image at a high field. For both potassium and rubidium the frequencies of the transition

$\|F, m_F\rangle$	B_0(G)	Δ_{th}(G)	$a_{\mathrm{bg}}(a_0)$
$\|1, 1\rangle$	317.9(5)	7.6	34
	531.2(3)	2.5	35
$\|1, -1\rangle$	117.6(4)	−1.3	35

Table 6.2.: Measured Feshbash resonance position B_0, theoretical widths Δ_{th} and background scattering lengths a_{bg} for ^{39}K and ^{87}Rb being in the same state [91].

used for imaging shift by -710 kHz/G which results in a shift of -355 MHz at 500 G. Such a detuning is not easy to realize and it might be necessary to construct an additional laser for high field detection. The third option would be to actively compensate the eddy currents by letting the currents through the coil overshoot in a controlled way [92]. For this the eddy currents in the coil would have to be modeled in an accurate way and especially the current supply would have to be able to deliver negative currents to force the field to zero. While this approach sounds more costly than to build a new laser it offers more advantages. The apparatus would not only be able to turn off the magnetic field very quickly but would also reach every designated field quick. That will be a major improvement when working with very cold clouds at very high scattering lengths where the reaction dynamics is very fast.

These limitations make it currently impractical to work with potassium in the $|1, 1\rangle$ state which features a very wide resonance at 402.6 G, and two inter-species resonances as shown in Figure 6.7. Table 6.2 shows the exact positions of these resonances. The inter-species scattering length is positive and almost constant in a range where the scattering length of potassium can be tuned from slightly negative over zero (at 350.4 G) to very high interaction. While this provides interesting possibilities for experiments with potassium-rubidium mixtures, it is not possible to change the inter-species interaction at a point where the intra-species scattering length of potassium is positive.

Fortunately the $|1, -1\rangle$ state provides a more promising Feshbach structure which is plotted in Figure 6.8. Due to the different sign of the two homonuclear ^{39}K resonances at 33.64 and 162.35 G a "valley" of positive scattering length can be found between them. An inter-species resonance is situated in this valley at 117.6 G. This makes the state $|1, -1\rangle$ state ideal to investigate ultra-cold interactions between ^{39}K and ^{87}Rb. Since both ^{39}K-resonances are very wide (with $\Delta_{\mathrm{th}} = -55$ G and 37 G) it is possible to create a ^{39}K-BEC on both sides of this valley. Thus one can

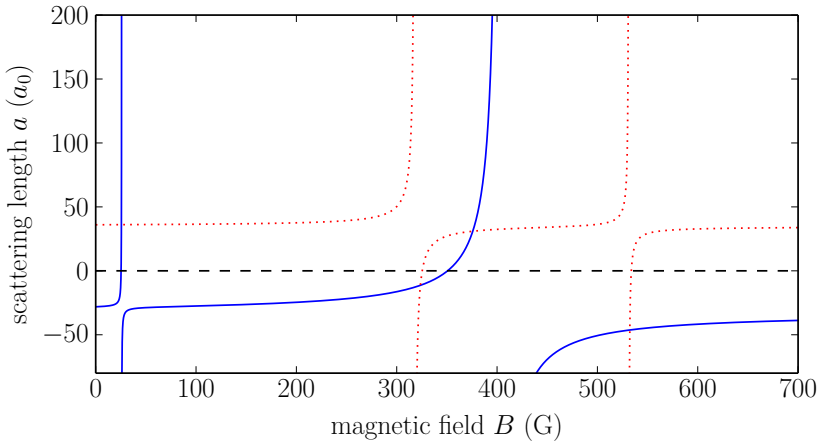

Figure 6.7.: Inter-species ^{39}K Feshbach resonances (blue) and ^{39}K–^{87}Rb intra-species resonances (dotted red), calculated according to Equation 2.55 using the values of Table 6.1 and Table 6.2. Both isotopes are in the $|1, 1\rangle$ state.

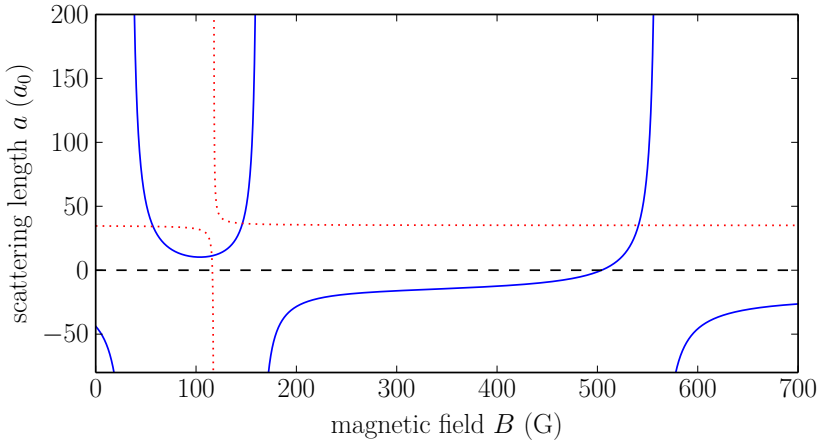

Figure 6.8.: Inter-species ^{39}K Feshbach resonances (blue) and ^{39}K–^{87}Rb intra-species resonances (dotted red), calculated according to Equation 2.55 using the values of Table 6.1 and Table 6.2. Both isotopes are in the $|1, -1\rangle$ state.

approach the inter-species resonance from both sides without having to pass it with a BEC.

In addition to the two resonances at a low field, a single very wide ($\Delta = 56\,\mathrm{G}$) ^{39}K resonance exits at 560.72 G. It features a very broad zero-crossing of the scattering length which allows to study basically interaction-free potassium at very low temperatures.

6.4. State preparation

To access the Feshbach resonances the atoms first have to be prepared in the designated internal state, and the field should be known precisely. Rapid adiabatic passages are used for both the state preparation and the magnetic field calibration.

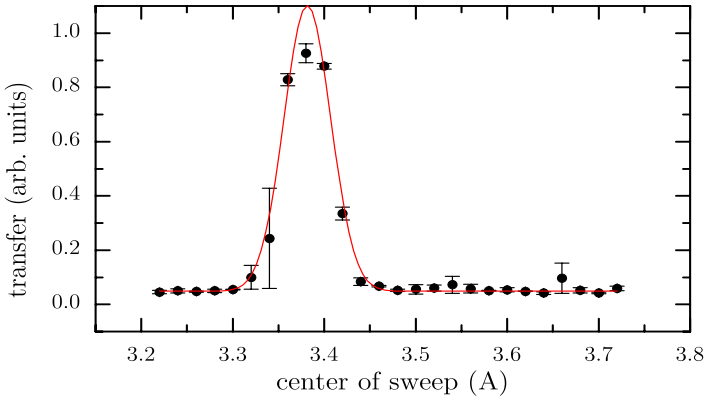

Figure 6.9.: Measurement of the current corresponding to a field of 33.6 G at the place of the atoms. A Gaussian was used as a fitting model to determine the center of the resonance.

To calibrate the magnetic field rubidium was used, since it provides a better signal-to-noise ratio than potassium. The calibration was carried out by first preparing a cold sample of ^{87}Rb in the optical dipole trap. The Breit-Rabi formula (2.50) was used to calculate the frequency for transition from the $|2,2\rangle$ state to the $|2,1\rangle$ state for a specific magnetic field. The RF-radiation was then applied to the atoms for 200 ms while the current through the Helmholtz coils was swept over a range of 100 mA. The center of the sweep was changed in steps of 20 mA until a transfer from $|2,2\rangle$ to $|2,1\rangle$ was observed. To verify the transfer an inhomogeneous field is applied for 20 ms directly after the release from the trap. This leads to a

spatial separations of the differenct spin components in this Stern-Gerlach-type experiment as shown in Figure 6.9.

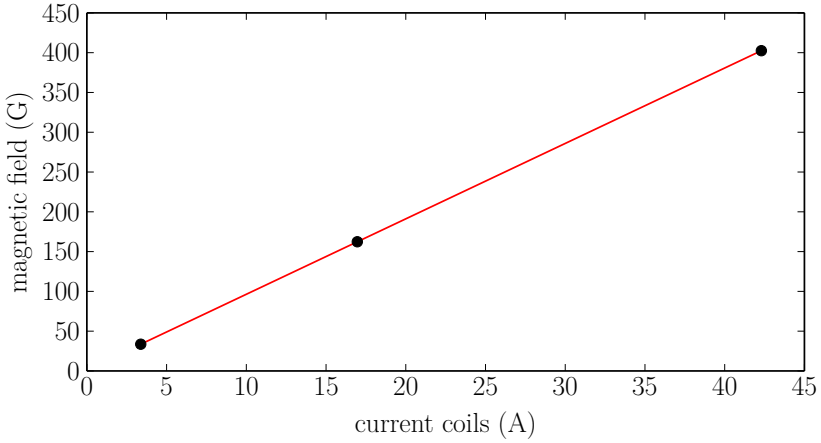

Figure 6.10.: Measurement of the absolute magnetic field and calibration of the Helmholtz coils. The magnetic field at the crossing point of the ODT is $1.55(5)\,\mathrm{G} + 9.479(2)\,\mathrm{G/A}$

By combining several such measurements (see Figure 6.10) we can determine the absolute magnetic offset field and the field produced by the coils. The offset field was found to be $1.55(5)\,\mathrm{G}$. This field is intentionally produced by the compensation coils in order to preserve the spin orientation of the atoms while they are held in the dipole trap.

To make use of the Feshbash resonances the potassium atoms have to be transferred from the $|2,2\rangle$ to the $|1,1\rangle$ state. To accomplish the transfer RF-radiation at 470 Mhz is irradiated onto the atoms with a power of 10 W while the magnetic field is linearly swept from 4.16 G to 3.2 G within 10 ms. Thus the avoided crossing shown in Figure 6.11 is used to achieve the state transfer. The efficiency of the transfer is verified by a Stern-Gerlach experiment (see Figure 6.12a). Its efficiency is close to 100% since no atoms are visible at the position of the $|2,2\rangle$ state.

To detect the transferred atoms in the $F = 1$ manifold they are pumped into the $F = 2$ manifold prior to the detection. This is achieved by using an additional beam of repumping light that is directed from below onto the atoms. It is turned on 200 µs before the detection pulse such that the heating caused by the repump laser does not translate into a change of the density profile. The repumping process is not very efficient such that the apparent number of atoms after repumping is

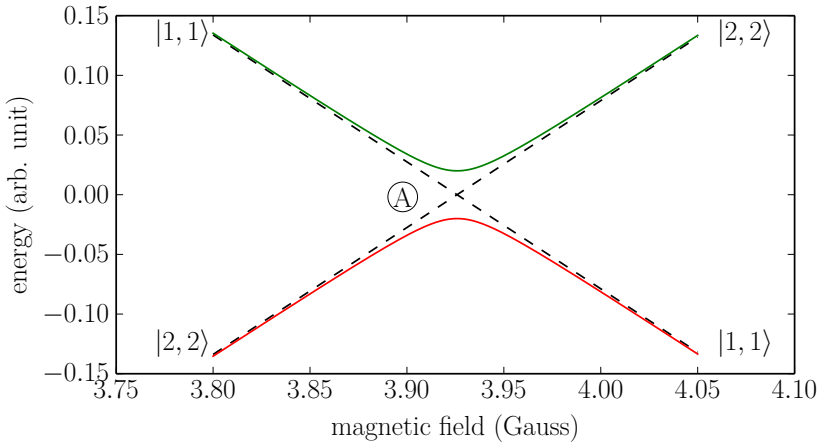

Figure 6.11.: Rapid adiabatic sweep to transfer potassium atoms from the state $|2,2\rangle$ to $|1,1\rangle$. Since no other transitions are possible due to the selection rule $\Delta m_F \pm 1$ the sweep can be done at a fairly low field. The position of the avoided crossing corresponds to a RF field at a frequency of 470 MHz.

roughly factor of 2 lower than the real one. This factor has been determined by comparing the number of atoms with and without the transfer.

Initially a sweep of the RF frequency was used for the subsequent transfer into the $|1,-1\rangle$ state as shown in Figure 2.4. Since the first transfer to $F = 1$ was unreliable the antenna was impedance matched to 470 Mhz by adding a 22 pF capacitor across the connectors of the antenna. This made the antenna unsuitable for the use at other frequencies. Thus a new antenna had to be installed for the second sweep which exhibited resonant behavior in the region of the sweep. It was therefore decided to hold the frequency fixed at 53 MHz and employ another magnetic field sweep. To transfer the atoms from $|1,1\rangle$ to $|1,-1\rangle$ the field was ramped from 99.47 G to 67.9 G during 10 ms. This transfer is again close to 100% efficient as shown in Figure 6.12b. As shown in Figure 6.12 the potassium atoms can thus be prepared in arbitrary states with high efficiency.

In a final step before the production of the BEC the relevant ^{39}K Feshbach resonances were investigated to confirm that the system is performing as expected. In the following data on the resonance at 33.64 G is presented. Since the three body loss coefficient scales with a^4 a high loss due to three body collisions is expected close to the resonance. Moreover as the coldest atoms have the highest probability

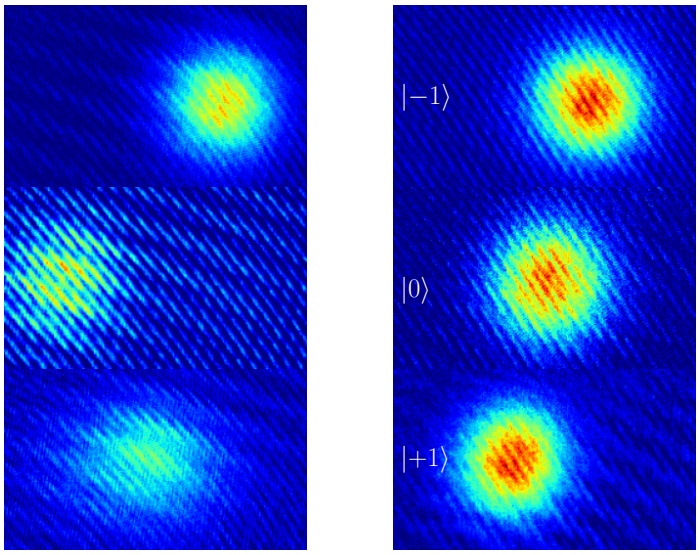

(a) ^{39}K atoms in $|F, m_F\rangle$ (b) ^{39}K atoms in $F = 1$, $|m_F\rangle$

Figure 6.12.: Stern-Gerlach type experiment which displaces the atoms in TOF, depending on their internal state. The image sequence (a) shows the atoms for the complete state transfer. Top: $|2, 2\rangle$. Middle: $|1, 1\rangle$. Bottom: $|1, -1\rangle$. (b) shows the atoms in the different m_F states of the $F = 1$ manifold.

to collide, leading to heating.

To measure the losses at the resonance a sample of ^{39}K in the state $|1, -1\rangle$ at a temperature of $\approx 250\,\mathrm{nK}$ was prepared in the optical dipole trap. Then the magnetic field was swept very over the resonance from 39.05 G to 32.42 G. This was done to minimize the intrinsic asymmetry of the curve caused by the fact that the atoms held at a field above 33.64 G will not suffer from enhanced losses. The atoms held at fields below 33.64 G on the other hand will experience losses from crossing the resonance independent of the actual scattering length they are held at for the measurement. The final measurement is performed by sweeping the field to the target value within 200 ms and holding the atoms there for 5 s. Figure 6.13 shows the results. It is clear that the temperature rises by 200 nK at the resonance. The losses show the characteristic asymmetric feature around the resonance. There are hardly any losses at high scattering lengths while they are drastic at negative

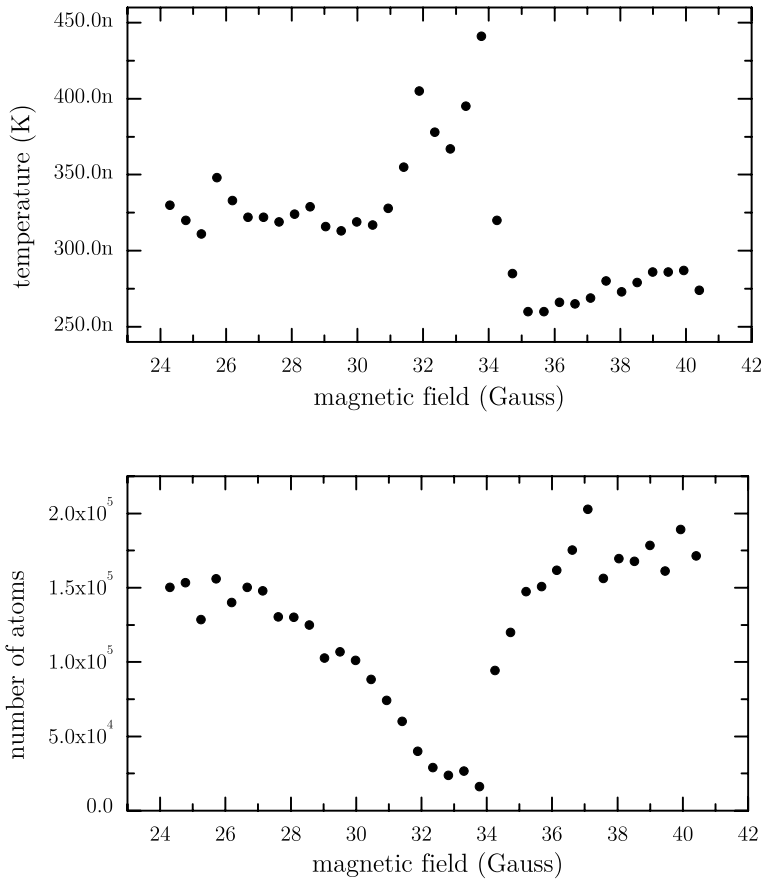

Figure 6.13.: Loss measurements at the homonuclear Feshbach resonance at 33.64 G.

scattering lengths. Thus it was shown that the magnetic field could be controlled precise enough to be able to investigate the various Feshbach resonances that show the expected loss features.

6.5. Production of ^{39}K condensates

The sympathetic cooling in the QUIC trap is sufficiently efficient such that that direct evaporation of potassium in the crossed optical dipole trap was attempted. The sequence used for this evaporation is sketched in Figure 6.14. After loading the dual species MOT, transport to the science cell and sympathetic cooling as described in section 5.5 1×10^6 potassium atoms at a PSD of 0.1 are obtained in the QUIC trap. The QUIC trap is relaxed by reducing the current through the

Anti-Helmholtz coil to 15 A and the current through the Ioffe coil to 9 A. The axial and radial trap frequencies for potassium are at this point 20.2 and 65.9 Hz. The atoms are loaded into the crossed dipole trap at a power of 6 W which corresponds to trap frequencies of 92 and 130 Hz.

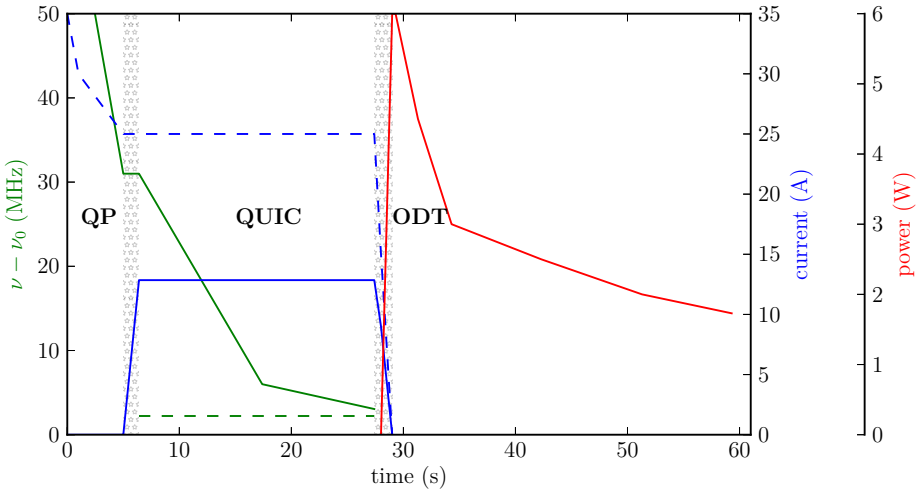

Figure 6.14.: Schematic of the experimental sequence that leads to a ^{39}K BEC. The green curves show the frequency-offsets from resonance of the microwave radiation used for evaporative cooling. The blue lines show the currents used for the QP coils (dashed) and the Ioffe coil. The red line shows the power of the optical dipole trap. The structured area marks transitions to another trap geometry.

The transfer from the state $|2, 2\rangle$ to $|1, -1\rangle$ is the performed within 300 ms as described in section 6.4. The magnetic field is then adjusted to 40.6 G and the field is kept at this value during the rest of the evaporation. This corresponds to $a = 139a_0$. Afterward the atoms are evaporatively cooled by reducing the power of the dipole trap beam within $2, 3, 8, 8$ and 9 s to $4.5, 3, 2.5, 2$ and 1.73 W respectively. The increase of phase space density versus atom number is shown in Figure 6.15. The evaporation is very efficient which is as $\gamma = 2.8$.

At this point the potassium atoms start to accumulate in the ground state. Figure 6.16 shows the transition from a thermal cloud to a BEC of ^{39}K. About $2{\times}10^5$ atoms are obtained in a pure BEC with a lifetime above 20 s. These numbers are comparable to other experiments which reported $4{\times}10^5$ atoms by using the same path [84] while starting with ten times more potassium and rubidium atoms

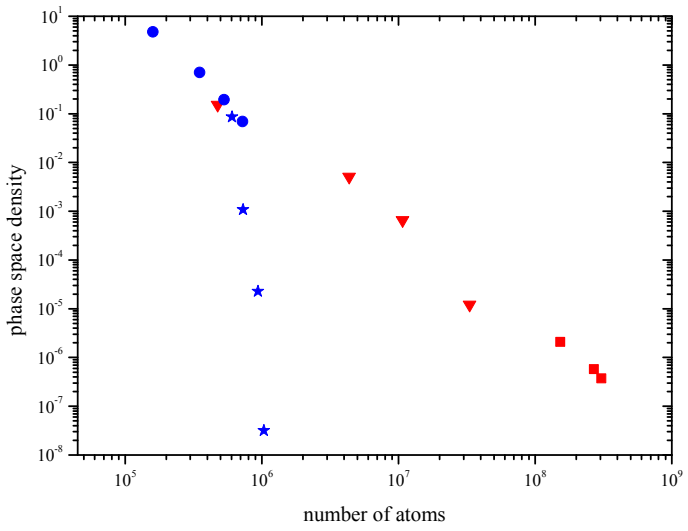

Figure 6.15.: Phase space density as a function of atom number. Rubidium (red) in the QP (squares) and QUIC (triangles) trap. Potassium (blue) in the QUIC (stars) and optical dipole trap (circles).

initially.

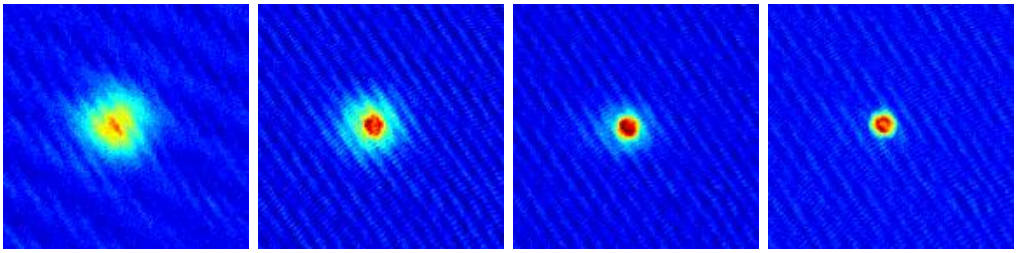

Figure 6.16.: Transition of a thermal ^{39}K-cloud to a BEC. Images taken 13 ms after the release from the crossed dipole trap.

6.6. Influence of the interaction

The successful creation of a single species ^{39}K BEC now allows for initial investigations of the influence of the scattering length on the condensate. In a first measurement the lifetime of the BEC was determined as a function of the scatter-

ing length. It is expected that the lifetime decreases when the scattering length increases due to enhanced three-body collisions. In a second measurement is the dependence of the size of the BEC after time-of-flight was investigated, depending on the scattering length.

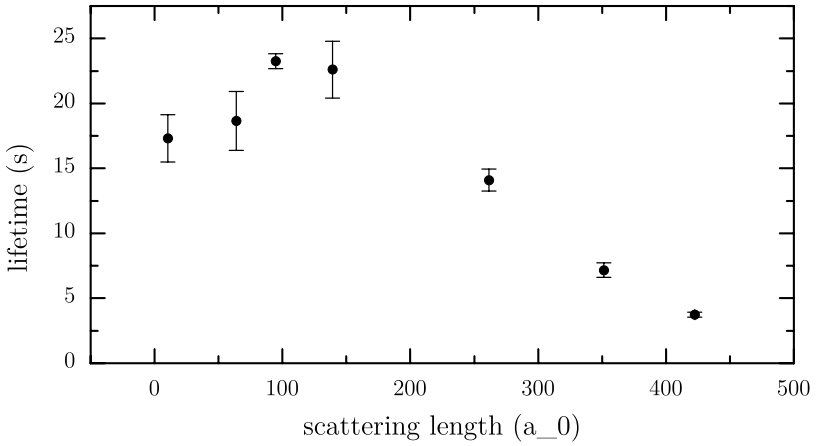

Figure 6.17.: The lifetime as a function of a. To measure the lifetime the atoms were held in the optical dipole trap for different amounts of time. An exponential decay was fitted to the number of atom from which the decay constant was extracted.

To measure the lifetime a BEC was produced as described in section 6.5 in a final trap with a depth of 160 nK. The trap depth was then increased to 270 nK within one second while the magnetic field was adjusted to its desired value at the same time. Then the hold time in this trap was varied to measure the lifetime. This procedure was repeated for different magnetic fields corresponding to different scatterings lengths. Figure 6.17 shows the results of this measurement. As expected the lifetime decreases from 24 s at $a = 100a_0$ to 4 s at $a = 423a_0$. Surprisingly the lifetime seems to drop at low scattering lengths. Since the error is considerably larger at long lifetimes this can be attributed partially to measurement errors. It may also indicate that the change of scattering length becomes non-adiabatic leading to heating and atom loss.

To investigate the behavior more quantitatively the loss rate is shown as a function of a in Figure 6.18, using the same data. The three body loss rate is given by [93]

$$\gamma_3 \equiv -\dot{N}/N = L_3\langle n^2\rangle. \tag{6.2}$$

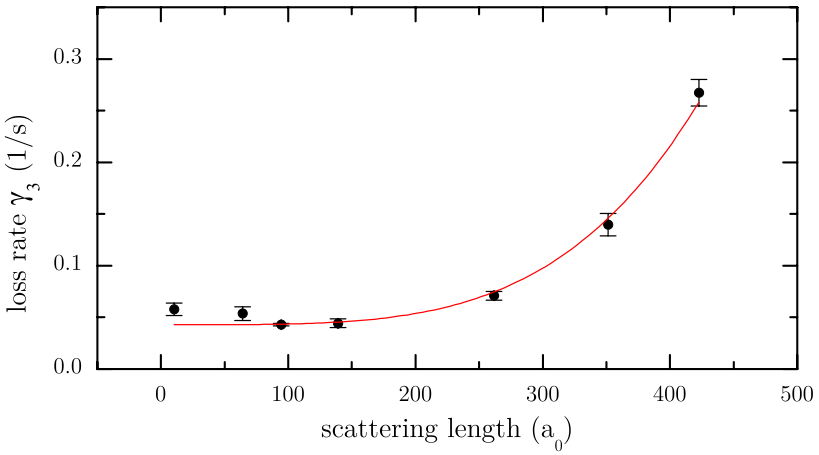

Figure 6.18.: Loss rate of the particles in a ^{87}Rb BEC as a function of the scattering length a. The red curve is a fit to the data with the model (6.3) depending with the 4th power on a. It was fitted with an offset accounting for a-independent loss processes.

Here N is the atom number, n the density and L_3 the three body loss coefficient. The angled brackets denote the average over the density distribution of the trapped gas. According to [94] L_3 is related to a as

$$L_3 = n_l C \frac{\hbar}{m} a^4 \tag{6.3}$$

where $n_l = 3$ is the number of atoms lost per recombination process and C is a dimensionless factor, which was predicted [95–97] to have a value between zero and maximally 67.9. In particular [97] predicts it to change between zero and maximum near a Feshbach resonance. In our case the fit gives $C = 80$ which is slightly above the maximal predicted value and clearly points to the need for further investigation. Despite the numerical deviation the model $L_3 \propto a^4$ fits very well.

To measure the size in dependence of the scattering length a BEC was created as described in section 6.5. Then the magnetic field was swept to the target field within 1 s. At this point the BEC was released from the trap and an absorption image was taken after 18 ms time-of-flight. At the beginning of the expansion the density is still high such that the interactions can influences the expansion of the cloud during the initial phase of the free expansion. Thus the magnetic field was kept on for the first 5 ms of TOF. Then it was turned off to be able to take an image. At long expansion times t the size $\sigma(t)$ of the BEC can be approximated

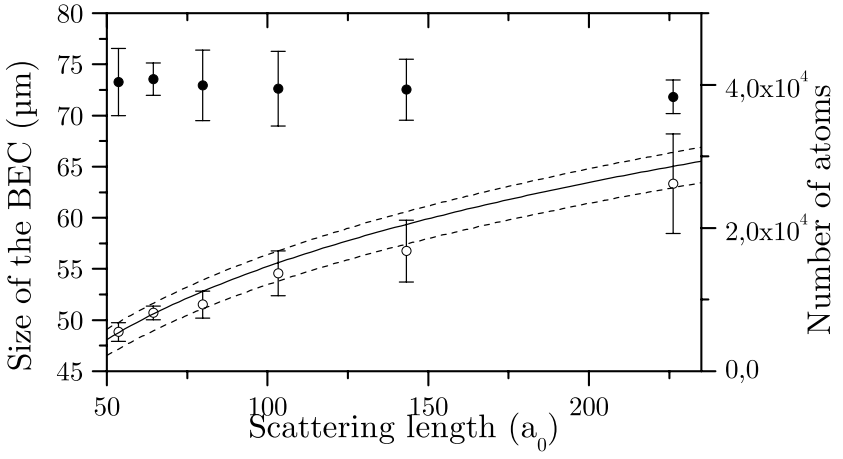

Figure 6.19.: Size of a ^{39}K BEC after 18 ms TOF as a function of a (triangles). The black line is calculated from (6.4). The dashed lines enclose the uncertainty region due to the error in atom number (squares).

linearly by [16]

$$\sigma(t) = \sqrt{\frac{2\mu}{m}}t, \tag{6.4}$$

where m is the mass of the atoms and μ the chemical potential which is given by [98]

$$\mu = \frac{\hbar\overline{\omega}}{2}\left(\frac{15aN}{r_{\mathrm{ho}}}\right)^{2/5}. \tag{6.5}$$

It depends on the harmonic oscillator length $r_{\mathrm{ho}} = \sqrt{\hbar/m\overline{\omega}}$, the number of atoms N and on the scattering length a where $\overline{\omega}$ is the geometric mean of the trap frequencies. In this case the Thomas-Fermi approximation was used which is valid for the given number of atoms and the scattering lengths that were investigated.

Figure 6.19 shows the results of this measurement. The black curve was calculated from (6.4). An uncertainty region is given (dashed lines), accounting for the error in the atom number measurement. The data points fit well with the theory in this range of a showing that good initial control and understanding of the system has been reached.

7 Conclusion and Outlook

Within this thesis a reliable experimental apparatus to produce pure ^{87}Rb and ^{39}K BECs, each consisting of well above 1×10^5 atoms, was realized. In addition ^{41}K BECs can be produced but further optimization will be necessary to improve the atom number and stability. The ability to manipulate the scattering length of potassium was demonstrated and good first understanding of the observed behavior was achieved.

The next practical experimental goal is to create a dual-species condensate consisting of ^{39}K and ^{87}Rb. To obtain this goal two options exist. Either the original plan of performing the last steps of sympathetic cooling with rubidium in the optical dipole trap can be followed. To follow this path more rubidium has to be retained in the QUIC trap before loading into the optical dipole trap. An alternative path would be to profit from the very efficient evaporation in the QUIC trap and sacrifice most rubidium in the evaporation process in the QUIC. The potassium can then be used as a coolant for rubidium in the dipole trap. To follow this path, the waists of the dipole trap have to be adjusted such that the trap depth is higher for potassium than for rubidium at the end of the evaporation sequence. It has to be evaluated which method will be more efficient.

Due to the large tunability of ^{39}K many avenues also exist for the sole usage of potassium. The zero crossing of the scattering length of ^{39}K at 350.4 G for the $|1,1\rangle$ state and 505.7 G for the $|1,-1\rangle$ state can be used to greatly improve the coherence time of atomic clocks. It was previously demonstrated on this apparatus how an effect called spin self-rephasing can be used to improve the coherence time of an ensemble and a coherence time of 26 s on the rubidium clock transistion was obtained [36]. This spin self-rephasing was achieved by adjusting the density of the

ensemble. Instead of changing the density, which was done by removing atoms from the cloud, the scattering length could be adjusted. Due to the broad resonance, the scattering length can be adjusted very precisely and all atoms are preserved which increases the signal to noise ratio. Using non-destructive imaging techniques the density could be monitored and the scattering length thus adjusted accordingly.

A second interesting experimental scenario for experiments with ^{39}K arises since the scattering length diverges at a Feshbach resonance and the system only depends on the density, thus becoming universal. It was recently shown that it is possible to investigate this regime with Bosons since the rethermalisation processes run faster then losses through three body collisions [93]. Due to the broad resonances, potassium is an ideal candidate to investigate these reactions.

An even broader range of experiments will be available once dual-species condensates can be created. In this case the inter-species feshbach resonances can be used to associate hetero-nuclear molecules [99]. Since the lifetime of these potassium-rubidium dimers is limited [100] an optical lattice has to be used to suppress the losses. From there on many avenues exist. It is possible to investigate chemical reactions under the constrained dimensionality provided by an optical lattice. The usage of a single lattice beam would form 2D-pancakes. By adding a second lattice cigar-shaped potentials would form and thus provide a 1D geometry. In the long term it may be possible to transfer the atoms into a deeply bound state which features a large electric dipole moment. This would allow access to regimes that lead to quantum phases like supersolids and checkerboard phases or superfluidity with anisotropic pairing [101].

Through the combination of potassium and rubidium one automatically creates an impurity of one species in the BEC of the other. The interaction of the impurity with the BEC leads to a polaron which is a quasi-particle which corresponds the distortion to the containing condensate. These polarons have been investigates in the weak coupling regime [102, 103]. The usage of ^{39}K and ^{87}Rb enables the possibility to adjust the interaction between the two species. This will influence the dynamics of the polaron that arises from the interaction of the impurity with the BEC. Especially the case of the strong coupling regime can be investigated and it is an interesting question at which interaction strength the polaron stays a quasi particle or breaks up such that a molecule is formed.

Due to the species dependent optical dipole force an optical lattice in principle allows to restrict the polaron to 2D while the BEC is largely unaffected which creates an interesting mixed 2D, 3D system. It is even possible to freeze the polaron completely such that a static scattering center in the BEC is created. It

is an important question whether a similar effect to the Anderson orthogonality catastrophe [104] in fermions could also occur in bosonic systems.

Both ^{39}K and combination of ^{39}K and ^{87}Rb thus provide many prospects and the experimental apparatus is now in an excellent condition to tackle these timely scientific questions.

List of Figures

List of Tables

Bibliography

[1] A. Einstein. Quantentheorie des idealen einatomigen Gases, Zweite Abhandlung. *Sitzungsberichte der Preußischen Akademie der Wissenschaften, Physikalisch-Mathematische Klasse, Berlin*, 1925.

[2] S. N. Bose. Plancks Gesetz und Lichtquantenhypothese. 26:178–181, 1924.

[3] M. H. Anderson, J. R. Ensher, M. R. Matthews, C. E. Wieman, and E. A. Cornell. Observation of Bose-Einstein Condensation in a Dilute Atomic Vapor. *Science*, 269(5221):198–201, 1995. doi:10.1126/science.269.5221.198. URL `http://www.sciencemag.org/content/269/5221/198.abstract`.

[4] K. B. Davis, M. O. Mewes, M. R. Andrews, N. J. van Druten, D. S. Durfee, D. M. Kurn, and W. Ketterle. Bose-Einstein Condensation in a Gas of Sodium Atoms. *Phys. Rev. Lett.*, 75:3969–3973, Nov 1995. doi:10.1103/PhysRevLett.75.3969. URL `http://link.aps.org/doi/10.1103/PhysRevLett.75.3969`.

[5] J. R. Abo-Shaeer, C. Raman, J. M. Vogels, and W. Ketterle. Observation of Vortex Lattices in Bose-Einstein Condensates. *Science*, 292(5516):476–479, 2001. doi:10.1126/science.1060182. URL `http://www.sciencemag.org/content/292/5516/476.abstract`.

[6] M. R. Andrews, C. G. Townsend, H.-J. Miesner, D. S. Durfee, D. M. Kurn, and W. Ketterle. Observation of Interference Between Two Bose Condensates. *Science*, 275(5300):637–641, 1997. doi:10.1126/science.275.5300.637. URL `http://www.sciencemag.org/content/275/5300/637.abstract`.

[7] M. Fattori, C. D'Errico, G. Roati, M. Zaccanti, M. Jona-Lasinio, M. Modugno, M. Inguscio, and G. Modugno. Atom Interferometry with a Weakly Interacting Bose-Einstein Condensate. *Phys. Rev. Lett.*, 100:080405, Feb 2008. doi:10.1103/PhysRevLett.100.080405. URL `http://link.aps.org/doi/10.1103/PhysRevLett.100.080405`.

[8] Naomi S Ginsberg, Sean R Garner, and Lene Vestergaard Hau. Coherent control of optical information with matter wave dynamics. *Nature*, 445(7128): 623–626, 2007.

[9] Jonathan Simon, Waseem S Bakr, Ruichao Ma, M Eric Tai, Philipp M Preiss, and Markus Greiner. Quantum simulation of antiferromagnetic spin chains in an optical lattice. *Nature*, 472(7343):307–312, 2011.

[10] S Ospelkaus, K-K Ni, D Wang, MHG De Miranda, B Neyenhuis, G Quéméner, PS Julienne, JL Bohn, DS Jin, and J Ye. Quantum-state controlled chemical reactions of ultracold potassium-rubidium molecules. *Science*, 327(5967): 853–857, 2010.

[11] Christopher J Pethick and Henrik Smith. *Bose-Einstein condensation in dilute gases*. Cambridge University Press, 2008.

[12] Robert Lorne Dugald Campbell. *Thermodynamic properties of a Bose gas with tuneable interactions*. PhD thesis, University of Cambridge, 2011.

[13] Alexander L. Gaunt, Tobias F. Schmidutz, Igor Gotlibovych, Robert P. Smith, and Zoran Hadzibabic. Bose-Einstein Condensation of Atoms in a Uniform Potential. *Phys. Rev. Lett.*, 110:200406, May 2013. doi:10.1103/PhysRevLett.110.200406. URL `http://link.aps.org/doi/10.1103/PhysRevLett.110.200406`.

[14] L. Pitaevskii and S. Stringari. *Bose-Einstein Condensation*. Oxford University Press, 2003.

[15] N. N. Bogoliubov. On the theory of superfluidity. 11(23), 1947.

[16] W. Ketterle, D. S. Durfee, and D. M. Stamper-Kurn. Making, probing and understanding Bose-Einstein condensates. *Proceedings of the International School of Physics - Enrico Fermi*, cond-mat/9904034, April 1999.

[17] R. Dubessy, K. Merloti, L. Longchambon, P.-E. Pottie, T. Liennard, A. Perrin, V. Lorent, and H. Perrin. Rubidium-87 Bose-Einstein condensate in an optically plugged quadrupole trap. *Phys. Rev. A*, 85:013643, Jan 2012. doi:10.1103/PhysRevA.85.013643. URL `http://link.aps.org/doi/10.1103/PhysRevA.85.013643`.

[18] D. M. Brink and C. V. Sukumar. Majorana spin-flip transitions in a magnetic trap. *Phys. Rev. A*, 74:035401, Sep 2006. doi:10.1103/PhysRevA.74.035401. URL `http://link.aps.org/doi/10.1103/PhysRevA.74.035401`.

[19] Myoung-Sun Heo, Jae-yoon Choi, and Yong-il Shin. Fast production of large ^{23}Na Bose-Einstein condensates in an optically plugged magnetic quadrupole trap. *Phys. Rev. A*, 83:013622, Jan 2011. doi:10.1103/PhysRevA.83.013622. URL `http://link.aps.org/doi/10.1103/PhysRevA.83.013622`.

[20] N. Hinkley, J. A. Sherman, N. B. Phillips, M. Schioppo, N. D. Lemke, K. Beloy, M. Pizzocaro, C. W. Oates, and A. D. Ludlow. An Atomic Clock with 10–18 Instability. *Science*, 341(6151):1215–1218, 2013. doi:10.1126/science.1240420. URL `http://www.sciencemag.org/content/341/6151/1215.abstract`.

[21] M. Scherer, B. Lücke, G. Gebreyesus, O. Topic, F. Deuretzbacher, W. Ertmer, L. Santos, J. J. Arlt, and C. Klempt. Spontaneous Breaking of Spatial and Spin Symmetry in Spinor Condensates. *Phys. Rev. Lett.*, 105:135302, Sep 2010. doi:10.1103/PhysRevLett.105.135302. URL `http://link.aps.org/doi/10.1103/PhysRevLett.105.135302`.

[22] B. Lücke, M. Scherer, J. Kruse, L. Pezzé, F. Deuretzbacher, P. Hyllus, O. Topic, J. Peise, W. Ertmer, J. Arlt, L. Santos, A. Smerzi, and C. Klempt. Twin Matter Waves for Interferometry Beyond the Classical Limit. *Science*, 334(6057):773–776, 2011. doi:10.1126/science.1208798. URL `http://www.sciencemag.org/content/334/6057/773.abstract`.

[23] Rudolf Grimm, Matthias Weidemüller, and Yurii B Ovchinnikov. Optical dipole traps for neutral atoms. *Advances in atomic, molecular, and optical physics*, 42:95–170, 2000.

[24] G. Kleine-Büning. *Lange Kohärenzzeit optisch gefangener Ensembles*. PhD thesis, University of Hannover, 2011.

[25] M. S. Safronova, Bindiya Arora, and Charles W. Clark. Frequency-dependent polarizabilities of alkali-metal atoms from ultraviolet through infrared spectral regions. *Phys. Rev. A*, 73:022505, Feb 2006. doi:10.1103/PhysRevA.73.022505. URL `http://link.aps.org/doi/10.1103/PhysRevA.73.022505`.

[26] C. Kittel. *Introduction to Solid State Physics*. Wiley, 7 edition, 1995.

[27] Henrik Kjær Andersen. *Bose-Einstein condensates in Optical lattices*. PhD thesis, Aarhus University, 2008.

[28] Seo Ho Youn, Mingwu Lu, Ushnish Ray, and Benjamin L. Lev. Dysprosium magneto-optical traps. *Phys. Rev. A*, 82:043425, Oct 2010. doi:10.1103/PhysRevA.82.043425. URL `http://link.aps.org/doi/10.1103/PhysRevA.82.043425`.

[29] C. C. Gerry and P. L. Knight. *Introductory Quantum Optics*. Cambridge, 2005.

[30] Mark Fox. *Quantum Optics: An Introduction: An Introduction*, volume 15. Oxford university press, 2006.

[31] T L Gustavson, A Landragin, and M A Kasevich. Rotation sensing with a dual atom-interferometer Sagnac gyroscope. *Classical and Quantum Gravity*, 17(12):2385, 2000. URL `http://stacks.iop.org/0264-9381/17/i=12/a=311`.

[32] Achim Peters, Keng Yeow Chung, and Steven@articletakamoto2005optical, title=An optical lattice clock, author=Takamoto, Masao and Hong, Feng-Lei and Higashi, Ryoichi and Katori, Hidetoshi, journal=Nature, volume=435, number=7040, pages=321–324, year=2005, publisher=Nature Publishing Group Chu. Measurement of gravitational acceleration by dropping atoms. *Nature*, 400(6747):849–852, 1999.

[33] Masao Takamoto, Feng-Lei Hong, Ryoichi Higashi, and Hidetoshi Katori. An optical lattice clock. *Nature*, 435(7040):321–324, 2005.

[34] J. B. Fixler, G. T. Foster, J. M. McGuirk, and M. A. Kasevich. Atom Interferometer Measurement of the Newtonian Constant of Gravity. *Science*, 315(5808):74–77, 2007. doi:10.1126/science.1135459. URL `http://www.sciencemag.org/content/315/5808/74.abstract`.

[35] Andreas Wicht, Joel M Hensley, Edina Sarajlic, and Steven Chu. A Preliminary Measurement of the Fine Structure Constant Based on Atom Interferometry. *Physica Scripta*, 2002(T102):82, 2002. URL `http://stacks.iop.org/1402-4896/2002/i=T102/a=014`.

[36] G Kleine Büning, J Will, W Ertmer, E Rasel, Jan Arlt, C Klempt, F Ramirez-Martinez, F Piéchon, and P Rosenbusch. Extended coherence time on the clock transition of optically trapped Rubidium. *Physical Review Letters*, 106 (24):240801, 2011. doi:10.1103/PhysRevLett.106.240801.

[37] J. C. Camparo and R. P. Frueholz. Parameters of adiabatic rapid passage in the 0-0 hyperfine transition of ^{87}Rb. *Phys. Rev. A*, 30(2):803–811, 1984. doi:10.1103/PhysRevA.30.803.

[38] D. A. Steck. Rubidium 87 *D* Line Data. Technical report, Oregon Center for Optics and Department of Physics, 2010. URL `http://steck.us/alkalidata`.

[39] TG Tiecke. Properties of potassium. Technical report, 2010.

[40] J. J. Sakurai. *Modern Quantum Mechanics*. Addison-Wesley, 1994.

[41] A. J. Moerdijk, B. J. Verhaar, and A. Axelsson. Resonances in ultracold collisions of ^{6}Li, ^{7}Li, and ^{23}Na. *Phys. Rev. A*, 51:4852–4861, Jun 1995. doi:10.1103/PhysRevA.51.4852. URL `http://link.aps.org/doi/10.1103/PhysRevA.51.4852`.

[42] Cheng Chin, Rudolf Grimm, Paul Julienne, and Eite Tiesinga. Feshbach resonances in ultracold gases. *Rev. Mod. Phys.*, 82:1225–1286, Apr 2010. doi:10.1103/RevModPhys.82.1225. URL `http://link.aps.org/doi/10.1103/RevModPhys.82.1225`.

[43] HERMAN FESHBACH. Unified Theory of Nuclear Reactions. *Rev. Mod. Phys.*, 36:1076–1078, Oct 1964. doi:10.1103/RevModPhys.36.1076. URL `http://link.aps.org/doi/10.1103/RevModPhys.36.1076`.

[44] U. Fano. Effects of Configuration Interaction on Intensities and Phase Shifts. *Phys. Rev.*, 124:1866–1878, Dec 1961. doi:10.1103/PhysRev.124.1866. URL `http://link.aps.org/doi/10.1103/PhysRev.124.1866`.

[45] Eddy Timmermans, Paolo Tommasini, Mahir Hussein, and Arthur Kerman. Feshbach resonances in atomic Bose–Einstein condensates. *Physics Reports*, 315(1–3):199 – 230, 1999. ISSN 0370-1573. doi:http://dx.doi.org/10.1016/S0370-1573(99)00025-3. URL `http://www.sciencedirect.com/science/article/pii/S0370157399000253`.

[46] Elizabeth A Donley, Neil R Claussen, Sarah T Thompson, and Carl E Wieman. Atom–molecule coherence in a Bose–Einstein condensate. *Nature*, 417(6888): 529–533, 2002.

[47] Jens Herbig, Tobias Kraemer, Michael Mark, Tino Weber, Cheng Chin, Hanns-Christoph Nägerl, and Rudolf Grimm. Preparation of a Pure Molecular Quantum Gas. *Science*, 301(5639):1510–1513, 2003. doi:10.1126/science.1088876. URL `http://www.sciencemag.org/content/301/5639/1510.abstract`.

[48] Simon Stellmer, Benjamin Pasquiou, Rudolf Grimm, and Florian Schreck. Creation of Ultracold Sr_2 Molecules in the Electronic Ground State. *Phys. Rev. Lett.*, 109:115302, Sep 2012. doi:10.1103/PhysRevLett.109.115302. URL `http://link.aps.org/doi/10.1103/PhysRevLett.109.115302`.

[49] Elena Kuznetsova, Marko Gacesa, Philippe Pellegrini, Susanne F Yelin, and Robin Côté. Efficient formation of ground-state ultracold molecules via STIRAP from the continuum at a Feshbach resonance. *New Journal of Physics*, 11(5):055028, 2009. URL `http://stacks.iop.org/1367-2630/11/i=5/a=055028`.

[50] Jacob F Sherson, Sung Jong Park, Poul L Pedersen, Nils Winter, Miroslav Gajdacz, Sune Mai, and Jan Arlt. The pump–probe coupling of matter wave packets to remote lattice states. *New Journal of Physics*, 14(8):083013, 2012. URL `http://stacks.iop.org/1367-2630/14/i=8/a=083013`.

[51] Poul L. Pedersen, Miroslav Gajdacz, Nils Winter, Andrew J. Hilliard, Jacob F. Sherson, and Jan Arlt. Production and manipulation of wave packets from ultracold atoms in an optical lattice. *Phys. Rev. A*, 88:023620, Aug 2013. doi:10.1103/PhysRevA.88.023620. URL `http://link.aps.org/doi/10.1103/PhysRevA.88.023620`.

[52] Poul L Pedersen. Dynamics of Bose-Einstein condensates in optical lattices. Part A Report.

[53] L. Viverit, C. Menotti, T. Calarco, and A. Smerzi. Efficient and Robust Initialization of a Qubit Register with Fermionic Atoms. *Phys. Rev. Lett.*, 93:110401, 2004.

[54] Sung Park, Henrik Andersen, Sune Mai, Jan Arlt, and Jacob Sherson. Dynamical control of matter-wave splitting using time-dependent optical lattices. *Phys. Rev. A*, 85(3):033626, March 2012. ISSN 1050-2947. doi:10.1103/PhysRevA.85.033626. URL `http://link.aps.org/doi/10.1103/PhysRevA.85.033626`.

[55] W. Salzmann, T. Mullins, J. Eng, M. Albert, R. Wester, M. Weidemüller, A. Merli, S. M. Weber, F. Sauer, M. Plewicki, F. Weise, L. Wöste, and A. Lindinger. Coherent Transients in the Femtosecond Photoassociation of Ultracold Molecules. *Phys. Rev. Lett.*, 100(23):233003, Jun 2008. doi:10.1103/PhysRevLett.100.233003.

[56] E. Goulielmakis, Z.-H. Loh, A. Wirth, R. Santra, N. Rohringer, V. S. Yakovlev, S. Zherebtsov, T. Pfeifer, A. M. Azzeer, M. F. Kling, S. R. Leone, and F. Krausz. Real-time observation of valence electron motion. *Nature*, 466 (7307):739–43, August 2010. ISSN 1476-4687. doi:10.1038/nature09212. URL `http://www.ncbi.nlm.nih.gov/pubmed/20686571`.

[57] N. F. Scherer, R. J. Carlson, A. Matro, M. Du, A. J. Ruggiero, V. Romero-Rochin, J. A. Cina, G. R. Fleming, and S. A. Rice. Fluorescence-detected wave packet interferometry: Time resolved molecular spectroscopy with sequences of femtosecond phase-locked pulses. *J. Chem. Phys.*, 95(3):1487, 1991. ISSN 00219606. doi:10.1063/1.461064. URL `http://link.aip.org/link/JCPSA6/v95/i3/p1487/s1&Agg=doi`.

[58] J. L. Herek, A. Materny, and A. H. Zewail. Femtosecond control of an elementary unimolecular reaction from the transition-state region. *Chem. Phys. Lett.*, 228(1-3):15–25, September 1994. ISSN 00092614. doi:10.1016/0009-2614(94)00910-4. URL `http://linkinghub.elsevier.com/retrieve/pii/0009261494009104`.

[59] J. Will. *Symmetrieabhängige Frequenzverschiebungen in Atomuhren*. PhD thesis, University of Hanover, 2012.

[60] G Kleine Büning, J Will, W Ertmer, C Klempt, and Jan Arlt. A slow

gravity compensated atom laser. *Applied Physics B*, 100(1):117–123, 2010. doi:10.1007/s00340-010-4078-7.

[61] C. Klempt, T. van Zoest, T. Henninger, O. Topic, E. Rasel, W. Ertmer, and J. Arlt. Ultraviolet light-induced atom desorption for large rubidium and potassium magneto-optical traps. *Phys. Rev. A*, 73(1):13410, 2006. doi:10.1103/PhysRevA.73.013410.

[62] L. Ricci, M. Weidemüller, T. Esslinger, A. Hemmerich, C. Zimmermann, V. Vuletic, W. Köning, and T. W. Hänsch. A compact grating-stabilized diode laser system for atomic physics. 117:541–549, June 1995.

[63] O. Schmidt, K.-M. Knaak, R. Wyands, and D. Meschede. Cesium saturation spectroscopy revisited: How to reverse peaks and observe narrow resonances. 59:167–178, 1994.

[64] U. Schünemann, H. Engler, R. Grimm, W. Weidemüller, and M. Zielonkowski. Simple scheme for tunable frequency offset locking of two lasers. 70(1): 242–243, January 1999. doi:10.1063/1.1149573.

[65] G. R. Hadley. Injection Locking of Diode Lasers. QE-22(3):419–426, March 1986. doi:10.1109/JQE.1986.1072979.

[66] J.N. Walpole. Semiconductor amplifiers and lasers with tapered gain regions. *Optical and Quantum Electronics*, 28(6):623–645, 1996. ISSN 0306-8919. doi:10.1007/BF00411298. URL `http://dx.doi.org/10.1007/BF00411298`.

[67] Bernd Lücke. Aufbau und Planung einer Hybridfalle zur Erzeugung ultrakalter Quantengase. Master's thesis, 2009.

[68] H.J. Metcalf and P. Van der Straten. *Laser cooling and trapping of atoms*. Springer, New York, 1999.

[69] Wolfgang Petrich, Michael H. Anderson, Jason R. Ensher, and Eric A. Cornell. Stable, Tightly Confining Magnetic Trap for Evaporative Cooling of Neutral Atoms. *Phys. Rev. Lett.*, 74(17):3352–3355, Apr 1995. doi:10.1103/PhysRevLett.74.3352.

[70] Tilman Esslinger, Immanuel Bloch, and Theodor W. Hänsch. Bose-Einstein condensation in a quadrupole-Ioffe-configuration trap. *Phys. Rev. A*, 58: R2664–R2667, Oct 1998. doi:10.1103/PhysRevA.58.R2664. URL `http://link.aps.org/doi/10.1103/PhysRevA.58.R2664`.

[71] D. Sofikitis, G. Stern, L. Kime, E. Dimova, A. Fioretti, D. Comparat, and P. Pillet. Loading a dipole trap from an atomic reservoir. *The European Physical Journal D*, 61(2):437–442, 2011. ISSN 1434-6060. doi:10.1140/epjd/e2010-10261-5. URL `http://dx.doi.org/10.1140/epjd/e2010-10261-5`.

[72] Carlos R. Menegatti, Bruno S. Marangoni, Nadia Bouloufa-Maafa, Olivier Dulieu, and Luis G. Marcassa. Trap loss in a rubidium crossed dipole trap by short-range photoassociation. *Phys. Rev. A*, 87:053404, May 2013. doi:10.1103/PhysRevA.87.053404. URL `http://link.aps.org/doi/10.1103/PhysRevA.87.053404`.

[73] K Dieckmann, RJC Spreeuw, M Weidemüller, and JTM Walraven. Two-dimensional magneto-optical trap as a source of slow atoms. *Physical Review A*, 58(5):3891, 1998. doi:10.1103/PhysRevA.58.3891.

[74] M. Landini, S. Roy, G. Roati, A. Simoni, M. Inguscio, G. Modugno, and M. Fattori. Direct evaporative cooling of ^{39}K atoms to Bose-Einstein condensation. *Phys. Rev. A*, 86:033421, Sep 2012. doi:10.1103/PhysRevA.86.033421. URL `http://link.aps.org/doi/10.1103/PhysRevA.86.033421`.

[75] C. J. Myatt, E. A. Burt, R. W. Ghrist, E. A. Cornell, and C. E. Wieman. Production of Two Overlapping Bose-Einstein Condensates by Sympathetic Cooling. *Phys. Rev. Lett.*, 78:586–589, Jan 1997. doi:10.1103/PhysRevLett.78.586. URL `http://link.aps.org/doi/10.1103/PhysRevLett.78.586`.

[76] Y.-J. Lin, A. R. Perry, R. L. Compton, I. B. Spielman, and J. V. Porto. Rapid production of ^{87}Rb Bose-Einstein condensates in a combined magnetic and optical potential. *Phys. Rev. A*, 79:063631, Jun 2009. doi:10.1103/PhysRevA.79.063631. URL `http://link.aps.org/doi/10.1103/PhysRevA.79.063631`.

[77] L. G. Marcassa, G. D. Telles, S. R. Muniz, and V. S. Bagnato. Collisional losses in a K-Rb cold mixture. *Phys. Rev. A*, 63:013413, Dec 2000. doi:10.1103/PhysRevA.63.013413. URL `http://link.aps.org/doi/10.1103/PhysRevA.63.013413`.

[78] Wolfgang Ketterle, Kendall B Davis, Michael A Joffe, Alex Martin, and David E Pritchard. High densities of cold atoms in a dark spontaneous-force optical trap. *Physical review letters*, 70(15):2253, 1993.

[79] Vandna Gokhroo, G Rajalakshmi, R Kollengode Easwaran, and C S Unnikrishnan. Sub-Doppler deep-cooled bosonic and fermionic isotopes of potassium in a compact 2D + –3D MOT set-up. *Journal of Physics B: Atomic, Molecular and Optical Physics*, 44(11):115307, 2011. URL `http://stacks.iop.org/0953-4075/44/i=11/a=115307`.

[80] M. Landini, S. Roy, L. Carcagní, D. Trypogeorgos, M. Fattori, M. Inguscio, and G. Modugno. Sub-Doppler laser cooling of potassium atoms. *Phys. Rev. A*, 84:043432, Oct 2011. doi:10.1103/PhysRevA.84.043432. URL `http://link.aps.org/doi/10.1103/PhysRevA.84.043432`.

[81] W. Ketterle and N. J. van Druten. Evaporative cooling of trapped atoms. 37:181, 1996.

[82] M. Egorov, B. Opanchuk, P. Drummond, B. V. Hall, P. Hannaford, and A. I. Sidorov. Measurement of *s*-wave scattering lengths in a two-component Bose-Einstein condensate. *Phys. Rev. A*, 87:053614, May 2013. doi:10.1103/PhysRevA.87.053614. URL `http://link.aps.org/doi/10.1103/PhysRevA.87.053614`.

[83] Francesca Ferlaino, Chiara D'Errico, Giacomo Roati, Matteo Zaccanti, Massimo Inguscio, Giovanni Modugno, and Andrea Simoni. Feshbach spectroscopy of a K-Rb atomic mixture. *Phys. Rev. A*, 73:040702, Apr 2006. doi:10.1103/PhysRevA.73.040702. URL `http://link.aps.org/doi/10.1103/PhysRevA.73.040702`.

[84] Robert L. D. Campbell, Robert P. Smith, Naaman Tammuz, Scott Beattie, Stuart Moulder, and Zoran Hadzibabic. Efficient production of large ^{39}K Bose-Einstein condensates. *Phys. Rev. A*, 82:063611, Dec 2010. doi:10.1103/PhysRevA.82.063611. URL `http://link.aps.org/doi/10.1103/PhysRevA.82.063611`.

[85] T. Kishimoto, J. Kobayashi, K. Noda, K. Aikawa, M. Ueda, and S. Inouye. Direct evaporative cooling of ^{41}K into a Bose-Einstein condensate. *Phys. Rev. A*, 79:031602, Mar 2009. doi:10.1103/PhysRevA.79.031602. URL `http://link.aps.org/doi/10.1103/PhysRevA.79.031602`.

[86] G. Ferrari, M. Inguscio, W. Jastrzebski, G. Modugno, G. Roati, and A. Simoni. Collisional Properties of Ultracold K-Rb Mixtures. *Phys. Rev. Lett.*, 89:053202,

Jul 2002. doi:10.1103/PhysRevLett.89.053202. URL http://link.aps.org/doi/10.1103/PhysRevLett.89.053202.

[87] G. Modugno, G. Ferrari, G. Roati, R. J. Brecha, A. Simoni, and M. Inguscio. Bose-Einstein Condensation of Potassium Atoms by Sympathetic Cooling. *Science*, 294(5545):1320–1322, 2001. doi:10.1126/science.1066687. URL http://www.sciencemag.org/content/294/5545/1320.abstract.

[88] G. Modugno, M. Modugno, F. Riboli, G. Roati, and M. Inguscio. Two Atomic Species Superfluid. *Phys. Rev. Lett.*, 89:190404, Oct 2002. doi:10.1103/PhysRevLett.89.190404. URL http://link.aps.org/doi/10.1103/PhysRevLett.89.190404.

[89] Chiara D'Errico, Matteo Zaccanti, Marco Fattori, Giacomo Roati, Massimo Inguscio, Giovanni Modugno, and Andrea Simoni. Feshbach resonances in ultracold 39 K. *New Journal of Physics*, 9(7):223, 2007. URL http://stacks.iop.org/1367-2630/9/i=7/a=223.

[90] Sanjukta Roy, Manuele Landini, Andreas Trenkwalder, Giulia Semeghini, Giacomo Spagnolli, Andrea Simoni, Marco Fattori, Massimo Inguscio, and Giovanni Modugno. Test of the Universality of the Three-Body Efimov Parameter at Narrow Feshbach Resonances. *Phys. Rev. Lett.*, 111:053202, Aug 2013. doi:10.1103/PhysRevLett.111.053202. URL http://link.aps.org/doi/10.1103/PhysRevLett.111.053202.

[91] Andrea Simoni, Matteo Zaccanti, Chiara D'Errico, Marco Fattori, Giacomo Roati, Massimo Inguscio, and Giovanni Modugno. Near-threshold model for ultracold KRb dimers from interisotope Feshbach spectroscopy. *Phys. Rev. A*, 77:052705, May 2008. doi:10.1103/PhysRevA.77.052705. URL http://link.aps.org/doi/10.1103/PhysRevA.77.052705.

[92] Michele Lynn Olsen. *Experiments with Feshbach molecules in a Bose-Fermi mixture*. PhD thesis, University of Colorado, 2008.

[93] Richard J. Fletcher, Alexander L. Gaunt, Nir Navon, Robert P. Smith, and Zoran Hadzibabic. Stability of a Unitary Bose Gas. *Phys. Rev. Lett.*, 111:125303, Sep 2013. doi:10.1103/PhysRevLett.111.125303. URL http://link.aps.org/doi/10.1103/PhysRevLett.111.125303.

[94] Tino Weber, Jens Herbig, Michael Mark, Hanns-Christoph Nägerl, and Rudolf Grimm. Three-Body Recombination at Large Scattering Lengths in an Ultracold Atomic Gas. *Phys. Rev. Lett.*, 91:123201, Sep 2003. doi:10.1103/PhysRevLett.91.123201. URL `http://link.aps.org/doi/10.1103/PhysRevLett.91.123201`.

[95] P. O. Fedichev, M. W. Reynolds, and G. V. Shlyapnikov. Three-Body Recombination of Ultracold Atoms to a Weakly Bound s Level. *Phys. Rev. Lett.*, 77:2921–2924, Sep 1996. doi:10.1103/PhysRevLett.77.2921. URL `http://link.aps.org/doi/10.1103/PhysRevLett.77.2921`.

[96] Esben Nielsen and J. H. Macek. Low-Energy Recombination of Identical Bosons by Three-Body Collisions. *Phys. Rev. Lett.*, 83:1566–1569, Aug 1999. doi:10.1103/PhysRevLett.83.1566. URL `http://link.aps.org/doi/10.1103/PhysRevLett.83.1566`.

[97] P. F. Bedaque, Eric Braaten, and H.-W. Hammer. Three-body Recombination in Bose Gases with Large Scattering Length. *Phys. Rev. Lett.*, 85:908–911, Jul 2000. doi:10.1103/PhysRevLett.85.908. URL `http://link.aps.org/doi/10.1103/PhysRevLett.85.908`.

[98] Franco Dalfovo, Stefano Giorgini, Lev P. Pitaevskii, and Sandro Stringari. Theory of Bose-Einstein condensation in trapped gases. *Rev. Mod. Phys.*, 71:463–512, Apr 1999. doi:10.1103/RevModPhys.71.463. URL `http://link.aps.org/doi/10.1103/RevModPhys.71.463`.

[99] C. Ospelkaus, S. Ospelkaus, L. Humbert, P. Ernst, K. Sengstock, and K. Bongs. Ultracold Heteronuclear Molecules in a 3D Optical Lattice. *Phys. Rev. Lett.*, 97:120402, Sep 2006. doi:10.1103/PhysRevLett.97.120402. URL `http://link.aps.org/doi/10.1103/PhysRevLett.97.120402`.

[100] Amodsen Chotia, Brian Neyenhuis, Steven A. Moses, Bo Yan, Jacob P. Covey, Michael Foss-Feig, Ana Maria Rey, Deborah S. Jin, and Jun Ye. Long-Lived Dipolar Molecules and Feshbach Molecules in a 3D Optical Lattice. *Phys. Rev. Lett.*, 108:080405, Feb 2012. doi:10.1103/PhysRevLett.108.080405. URL `http://link.aps.org/doi/10.1103/PhysRevLett.108.080405`.

[101] K. Góral, L. Santos, and M. Lewenstein. Quantum Phases of Dipolar Bosons in Optical Lattices. *Phys. Rev. Lett.*, 88:170406, Apr 2002.

doi:10.1103/PhysRevLett.88.170406. URL http://link.aps.org/doi/10.1103/PhysRevLett.88.170406.

[102] A. P. Chikkatur, A. Görlitz, D. M. Stamper-Kurn, S. Inouye, S. Gupta, and W. Ketterle. Suppression and Enhancement of Impurity Scattering in a Bose-Einstein Condensate. *Phys. Rev. Lett.*, 85:483–486, Jul 2000. doi:10.1103/PhysRevLett.85.483. URL http://link.aps.org/doi/10.1103/PhysRevLett.85.483.

[103] Nicolas Spethmann, Farina Kindermann, Shincy John, Claudia Weber, Dieter Meschede, and Artur Widera. Dynamics of Single Neutral Impurity Atoms Immersed in an Ultracold Gas. *Phys. Rev. Lett.*, 109:235301, Dec 2012. doi:10.1103/PhysRevLett.109.235301. URL http://link.aps.org/doi/10.1103/PhysRevLett.109.235301.

[104] P. W. Anderson. Infrared Catastrophe in Fermi Gases with Local Scattering Potentials. *Phys. Rev. Lett.*, 18:1049–1051, Jun 1967. doi:10.1103/PhysRevLett.18.1049. URL http://link.aps.org/doi/10.1103/PhysRevLett.18.1049.

A Supplemental figures

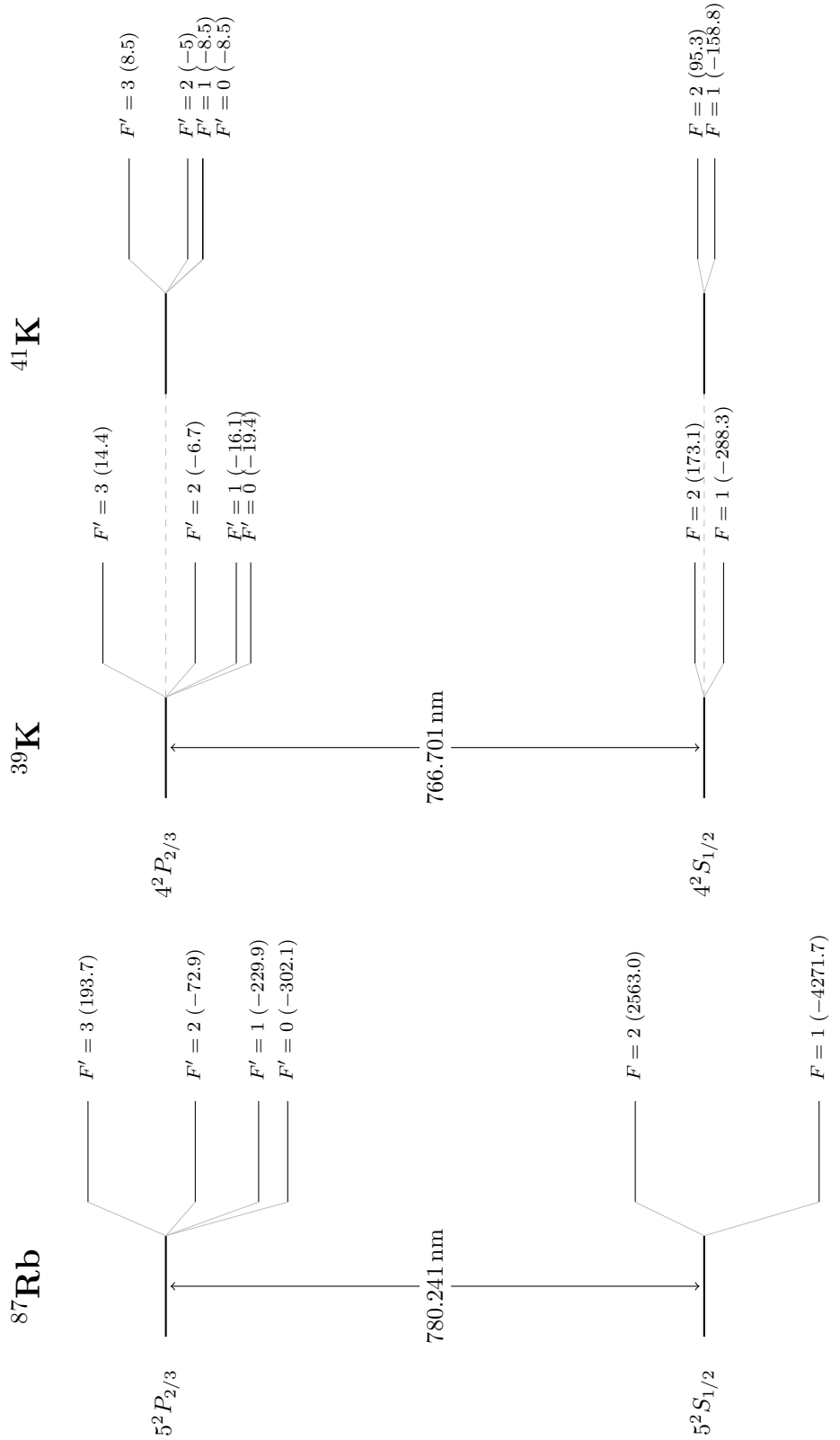

Figure A.1.: Level structure of ^{87}Rb, ^{39}K and ^{41}K. The level shift shown in brackets due to the hyperfine structure is given in MHz. The splittings are to scale but only withing the same species and the same angular momentum manifold. The values have been taken from refs. [38, 39].

.

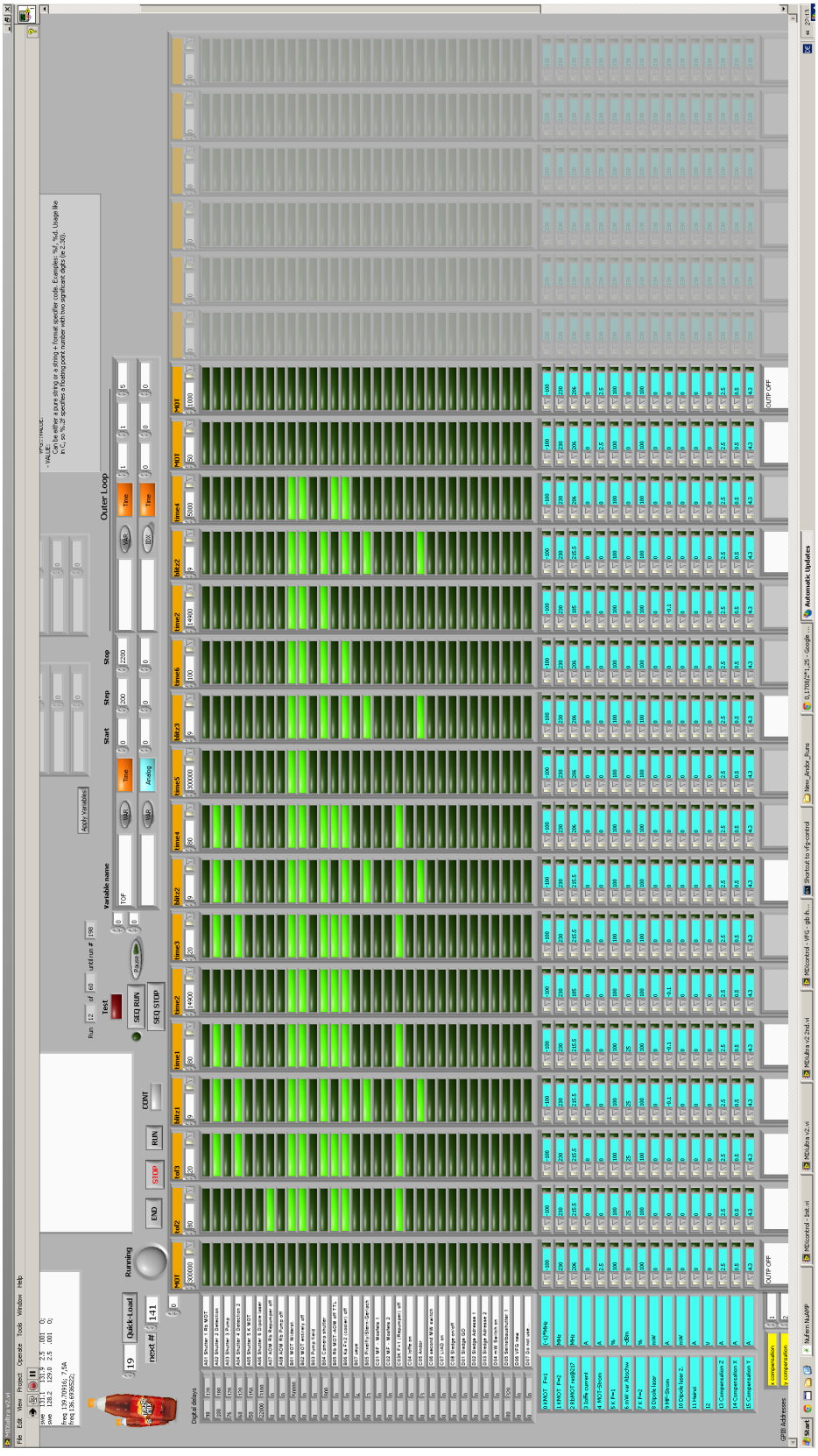

Figure A.2.: Screenshot of the LabView VI controlling the experiment.